Universidade de Vigo

CIC biomaGUNE
Biomaterialetako Ikerkuntza Kooperatiboko Zentroa
Centro de Investigación Cooperativa en Biomateriales

# Biosensing Using Metal Nanoparticles

Memoria presentada por Marc Coronado Puchau
para optar al grado de Doctor Internacional
Vigo, Noviembre de 2015

**D. Luis Manuel Liz Marzán, Catedrático del Departamento de Química Física de la Universidad de Vigo y D. Jorge Pérez Juste, Profesor Contratado Doctor en el mismo Departamento**

**INFORMAN:**

**Que Marc Coronado Puchau ha realizado en el Departamento de Química Física de la Universidad de Vigo y en el Centro de Investigación Cooperativa en Biomateriales (CIC biomaGUNE) de San Sebastián, bajo su dirección, el trabajo descrito en la presente memoria, que lleva por título "Biosensing Using Metal Nanoparticles", y que presenta para optar al grado de Doctor por la Universidad de Vigo con Mención Internacional.**

**Vigo, 8 de diciembre de 2015**

**Fdo. Luis Manuel Liz Marzán** **Fdo. Jorge Pérez Juste**

*A mi familia*

# Contents

# Motivation, Summary and List of publications

This PhD thesis aims at developing new plasmonic biosensors. In this context, the work presented here focuses on the synthesis of both silica and metal nanoparticles, as well as their surface functionalization and application in the detection of relevant molecules for human health. The development of new metal nanoparticles (NP) with improved plasmonic properties, along with the chemical control of their surface chemistry, are essential for this purpose. In this regard, synthesis and functionalization of nanoparticles were performed in this PhD thesis by improving existing protocols. All NPs described in this PhD thesis were characterized by UV-Vis spectroscopy and transmission electron microscopy (TEM). The NPs were used for the ultrasensitive detection of nerve gases, glucose, bacterial DNA or cocaine, among other biologically relevant molecules. The main objective of this thesis was thus the preparation of suitable nanostructures for the sensitive, selective and inexpensive detection of biological analytes. A brief summary of the PhD thesis is provided below, including the main aspects of the work developed in each chapter.

In Chapters 2 and 3 highly sensitive colorimetric biosensors for biological molecules (such as glucose and nerve gases) were developed by combining gold nanorods (AuNRs) and enzymes. In a first set of experiments, we explored the effect of an enzymatically obtained thiolated molecule on the growth of AuNRs (Chapter 2). The enzyme acetylcholinesterase was selected to produce thiocholine (a thiol-bearing molecule that can adsorb on the surface of gold seeds), thereby modulating the synthesis of the gold nanorods. Nerve gas analogs were colorimetrically detected by inhibiting acetylcholinesterase activity during AuNR synthesis. In a second set of experiments, the gradual etching of AuNRs with enzymatically produced hydroxyl radicals (Chapter 3) was investigated. Hydrogen peroxide ($H_2O_2$) and the enzyme Horse Radish Peroxidase (HRP) were used for the controlled oxidation of AuNRs. Enzymatic coupling of glucose oxidase to HRP activity allowed us to develop colorimetric assays for glucose detection. In both cases, the introduction of biocatalytic molecular species significantly improved the efficiency and biocompatibility of the system, thus opening new possibilities in biosensing using AuNPs.

The SERS performance of highly monodisperse gold nanotriangles with different sizes is presented in Chapter 4. As described in this chapter, gold nanotriangles display very interesting nanoplasmonic features with potential application in biosensing. However, those applications require high monodispersity and morphological stability. Our novel synthetic protocol in combination with mesoporous silica gated nanoparticles allowed us to use this nanostructure for the SERS detection of pathogenic DNA (*Mycobacterium* spp. *sp.*) and cocaine (Chapter 5).

This PhD thesis is expected to represent a significant advancement in the use of metal nanoparticles for biosensing. The NP synthesis methods developed in this work along with the use of mesoporous silica NP and biological catalysts allowed us to easily detect different biomolecules without complicated and expensive instrumentation. Indeed, some sensors can be even read out by the naked eye.

The work described in this dissertation has given rise to the following publications:

**Chapter 2**: Coronado-Puchau, M., Saa, L., Grzelczak, M., Pavlov, V., & Liz-Marzán, L. M. (**2013**). *Enzymatic modulation of gold nanorod growth and application to nerve gas detection*. Nano Today, 8(5), 461-468.

**Chapter 3**: Saa, L., Coronado-Puchau, M., Pavlov, V., & Liz-Marzán, L. M. (**2014**). *Enzymatic etching of gold nanorods by horseradish peroxidase and application to blood glucose detection*. Nanoscale, 6(13), 7405-7409.

**Chapter 4**: Scarabelli, L., Coronado-Puchau, M., Giner-Casares, J. J., Langer, J., & Liz-Marzán, L. M. (**2014**). *Monodisperse Gold Nanotriangles: Size Control, Large-Scale Self-Assembly, and Performance in Surface-Enhanced Raman Scattering*. ACS Nano, 8(6), 5833-5842.

**Chapter 5**: Oroval-Cucarella, M.; Coronado-Puchau, M.; Langer, J.; Sanz-Ortiz, M.N; Marcos, M.D.; Liz-Marzán, L.M; Martínez-Mañez, R.; *Surface Enhanced Raman Scattering and Gated Materials for the Ultrasensitive Detection of Mycoplasma and Cocaine*. Submitted.

Other publications to which the author has contributed during his PhD work are the following:

**1)** Polavarapu, L., Porta, A. L., Novikov, S. M., Coronado-Puchau, M., & Liz-Marzán, L. M. (**2014**). *Pen-on-Paper Approach Toward the Design of Universal Surface Enhanced Raman Scattering Substrates*. Small, 10(15), 3065-3071.

**2)** Wang, Y., Sentosun, K., Li, A., Coronado-Puchau, M., Sánchez-Iglesias, A., Li, S., & Liz-Marzan, L. M. (**2015**). *Engineering Structural Diversity in Gold Nanocrystals by Ligand-Mediated Interface Control*. Chemistry of Materials. DOI: 10.1021/acs.chemmater.5b03600.

**3)** Giner-Casares, J. J., Henriksen-Lacey, M., Coronado-Puchau, M., & Liz-Marzán, L. M. (**2015**). *Inorganic nanoparticles for biomedicine: where materials scientists meet medical research*. Materials Today. DOI: 10.1016/j.mattod.2015.07.004.

**4)** Bhaskar, U., Coronado-Puchau, M., Langer, J., Altantzis, T., Bals, S., Liz-Marzán, L. M. & Klajn, R. *Templated Assembly of Gold Nanoparticles with Low Packing Densities*. In preparation.

# 1. General Introduction

This Introduction is divided into three parts: we first deal with the synthesis and optical properties of metal nanoparticles, the second part comprises the synthesis of gated mesoporous silica and the mechanism underlying gate control, and the last part deals with the use of nanoparticles for biosensing based on UV-vis spectroscopy and surface enhanced Raman scattering (SERS). Prior to defining the different concepts detailed above, the basic concepts of metal, noble metal and metal nanoparticle are introduced. By definition, a metal is a substance with high electrical conductivity, luster, and malleability, which readily loses electrons to form positive ions (cations).[1] Among all metals, noble metals are resistant to corrosion and oxidation in moist air. The list of noble metals contains ruthenium, rhodium, palladium, silver, osmium, iridium, platinum, and gold, in order of increasing atomic number. Many of them are also called precious as they are of poor abundance in the Earth's crust. Noble metal nanoparticles (NP), especially gold (Au) and silver (Ag), have been intensively explored by the scientific community owing to their interesting properties. The *noble* nature of these NP compared with other NP, for example, transition metal NP such as iron, nickel, or cobalt, as well as their lower cytotoxicity render them attractive candidates for biological applications.[2,3] Much of the studies on noble metal NP are carried out using Au due to its higher chemical stability as compared to Ag. Therefore, in this PhD thesis Au was chosen to demonstrate the high potential of metal NP in biosensing under physiological conditions.

Gold NP have a rich history in science and technology, since they were used for both esthetic and medicinal purposes. Colloidal gold has been incorporated into glasses and vases to confer them with bright colors. The oldest known example is the fourth century AD Lycurgus cup made by the Romans (in exhibit at the British Museum of London). The cup appears red in transmitted light, and green in reflected light. Modern chemical analysis shows that the glass is not very different from that used today. However, it contains very small amounts of gold (about 40 ppm) and silver (about 300 ppm), in the form of mixed Au-Ag NPs of approximately 70 nm diameter.[4] In the middle ages a mixture of gold salts with molten glass was extensively used by medieval artisans to produce tiny gold colloids having a rich ruby color, and their varieties were exploited for coloration of glass, ceramics, and pottery. *Purple of Cassius*, a pink pigment commonly used in the seventeenth century, is also now known to be a combination of gold particles and tin dioxide. But it was in 1857 when Michael Faraday described a systematic chemical synthesis of colloidal Au NP based on the observation of the formation of a pure form of deep-red-colored colloidal gold by the reduction of an aqueous solution of chloroaurate ($AuCl_4^-$) using white phosphorus in $CS_2$, in a two-phase system.[5] This synthesis is considered to have been a major milestone in the development of nanotechnology. In addition, Faraday also investigated the optical properties of thin films prepared from dried colloidal solutions and found that colloidal gold had remarkable optical and electrical properties. Following Faraday, a large number of experimental methods have been reported for the synthesis of gold NPs.

# 1.1. Synthesis and Properties of Metal Nanoparticles

## 1.1.1.Synthesis of Nanometals

In general terms, chemical methods for the synthesis of nanomaterials are based in two steps: 1) reduction of metal ions, and 2) assembly of the metal atoms onto NP. As the synthesis initiates from atoms, these methods are also called *bottom-up* approaches. An ideal synthetic strategy should produce particles of a given size distribution through a simple process. A narrow size distribution is always desired to maintain well-defined properties. As described in more detail below, post-synthetic processes may be utilized if a methodology fails to generate monodisperse nanoparticles.

The design of generic methods that allow the preparation of gold nanostructures with a broad range of well-defined and controllable morphologies is needed to fully exploit their unique properties for practical applications. A typical synthesis of Au NP by chemical methods in liquid phase comprises three parts, namely inner Au atoms (central atoms), atoms exposed to the surface (surface atoms) and surface-protecting organic ligands or surfactants (Figure 1.1). The central gold atoms determine the crystallinity of the structure, whereas the geometry of the surface atoms form surface facets and edges that will dominate their catalytic activity and reactivity. The surfactant is anchored on the surface atoms, stabilizing them and providing surface functionality that influences the chemical nature and biocompatibility of the particles in solution, as described in detail below.[6]

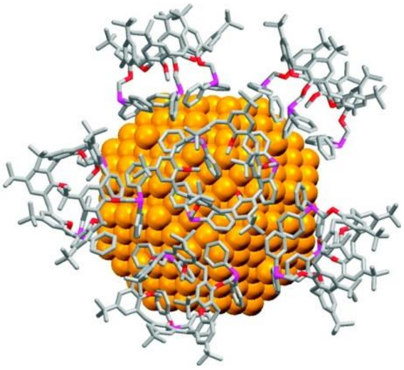

**Figure 1.1.-** Schematic representation of a AuNP protected by a ligand. Adapted from ref. [7].

#### 1.1.1.1. Synthesis of Isotropic Metal Nanoparticles

The so-called Turkevich method [8] is a simple process that has been widely adopted for the synthesis of colloidal gold NPs in water. In this approach, sodium citrate is used for the reduction of $Au^{3+}$ ions into $Au^0$ atoms. The subsequent aggregation results in the formation of NPs, typically at water boiling temperature. The NPs produced by this method are mostly monodisperse and spherical with an average diameter of around 15 nm. Reduction in the amount of sodium citrate can result in an increased size of the resulting NPs. Transmission electron microscopy (TEM) images of the particles obtained by this method are shown in Figure 1.2. The NPs prepared by this method are stable for long periods of time and have been extensively used for various investigations in biology and materials science.[6]

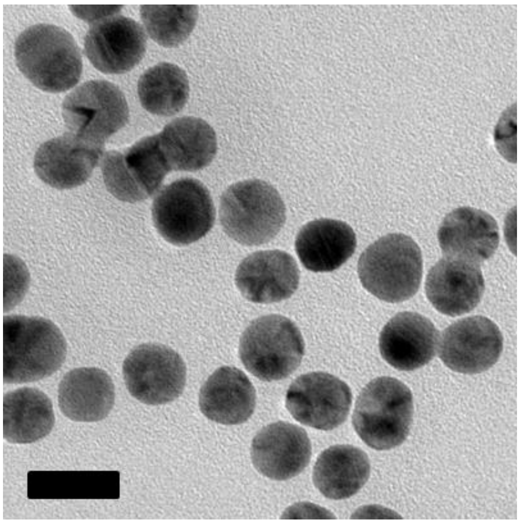

**Figure 1.2.-** Gold nanospheres. TEM image of ≈13 nm AuNPs obtained in our group by the Turkevich method. Scale bar: 20 nm.

#### 1.1.1.2. Synthesis of Anisotropic Metal Nanoparticles: The Seed Mediated Growth Method

Seed mediated growth is the most widely used strategy for the synthesis of anisotropic Au NPs. Based on the Zsigmondy's nuclear method [9] and proposed in the early 2000s by various groups,[10-13] the synthesis involves two consecutive steps. The first one comprises the synthesis of seed NPs by reduction of metal salts in the presence of stabilizing agents. This step involves the use of a strong reducing agent such as sodium borohydride ($NaBH_4$), which ensures a rapid nucleation rate leading to spherical nuclei with sizes typically ranging between 1 and 5 nm. Such conditions ensure rapid growth of all crystal surfaces, but are disadvantageous for shape control. Therefore, shape control is commonly achieved in the second step, in which the seed NPs act as both catalysts and nucleation points for the growth of the AuNPs. Metal reduction onto the seed particles is controlled in such a way that a symmetry-breaking event occurs, thus growing into the desired shape in a growth solution containing excess metal ions, a surfactant or shaping agent, and a mild reducing agent. Typically this growth stage is much slower than the first one. Note that the presence of surfactant molecules and other ions, such as silver or halides, together with the crystalline structure of the seeds irreversibly determine the growth process giving rise to NPs of different morphologies.[14,15]

An important piece of work in this respect was carried out by Liu and Guyot-Sionnest,[16] who observed differences between the crystalline structures of citrate- and cetyl trimethylammonium bromide- (CTAB) stabilized seeds prepared through reduction of $HAuCl_4$ with borohydride (Figure 1.3), thereby confirming the multiply-twinned structure of citrate-capped seeds and the single crystallinity of the seeds when CTAB was used as a capping agent.

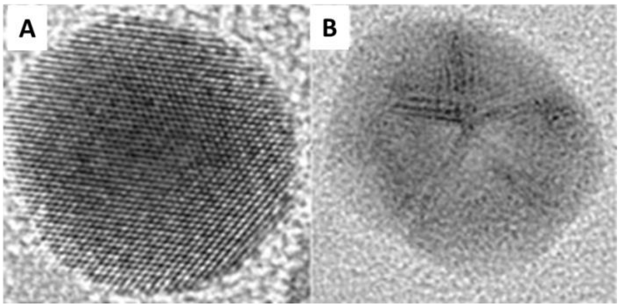

**Figure 1.3.-** Gold seed crystallinity. HR-TEM images of: a) single crystal seed and, b) multiply twinned seed. The diameters are around 2 nm. Adapted from [21].

### 1.1.1.2.1. Synthesis of Gold Nanorods

Seed mediated growth of gold nanorods using CTAB as surfactant is considered as the most efficient protocol to make anisotropic nanoparticles, in terms of the degree of control over size, shape and monodispersity. Therefore, it is also the most widely used protocol to make NP for biosensing and biomedical applications.[17] This method was first proposed by Murphy et al.[11] and significantly improved by Nikoobakht and El-Sayed[12] and other research groups,[18] so that it currently allows researchers to routinely synthesize AuNRs with shape-yields greater than 95%.

In a typical synthesis of AuNRs, ascorbic acid (a mild reducing agent) is added to an aqueous CTAB solution of $HAuCl_4$ to selectively reduce Au(III) to Au(I), followed by the addition of a small amount of silver nitrate and CTAB–capped single crystal seed particles. Gold seeds of about 2 nm in diameter catalyze the reduction of gold ions on their surface, while silver ions play a key role in the symmetry breaking event. Even though this event is known to be essential, limited understanding remains of how an isotropic seed particle becomes an asymmetric nanocrystal and about the growth parameters that trigger and drive this process. Recently, direct atomic-scale observation allowed Etheridge and co-workers to monitor the onset of asymmetry of the nascent crystal in such a way that they could conclude that silver ions are essential for the crystalline change of the seeds during the early stages of AuNR growth.[19] Further, the complete evolution of growth of AuNR has also been studied by using thiolated molecules that arrest the growth at different stages (see Figure 1.4).[20] In this respect, morphological control, mainly through variation of the aspect ratio, has been widely demonstrated by varying the concentration of silver nitrate and, to a lesser extent, of other parameters.[21] However, the precise control over this mechanism during or after the synthesis continues to be the subject of intense investigation, as minute changes in AuNR size, shape or morphology can be exploited to develop successful applications in materials science and biology.

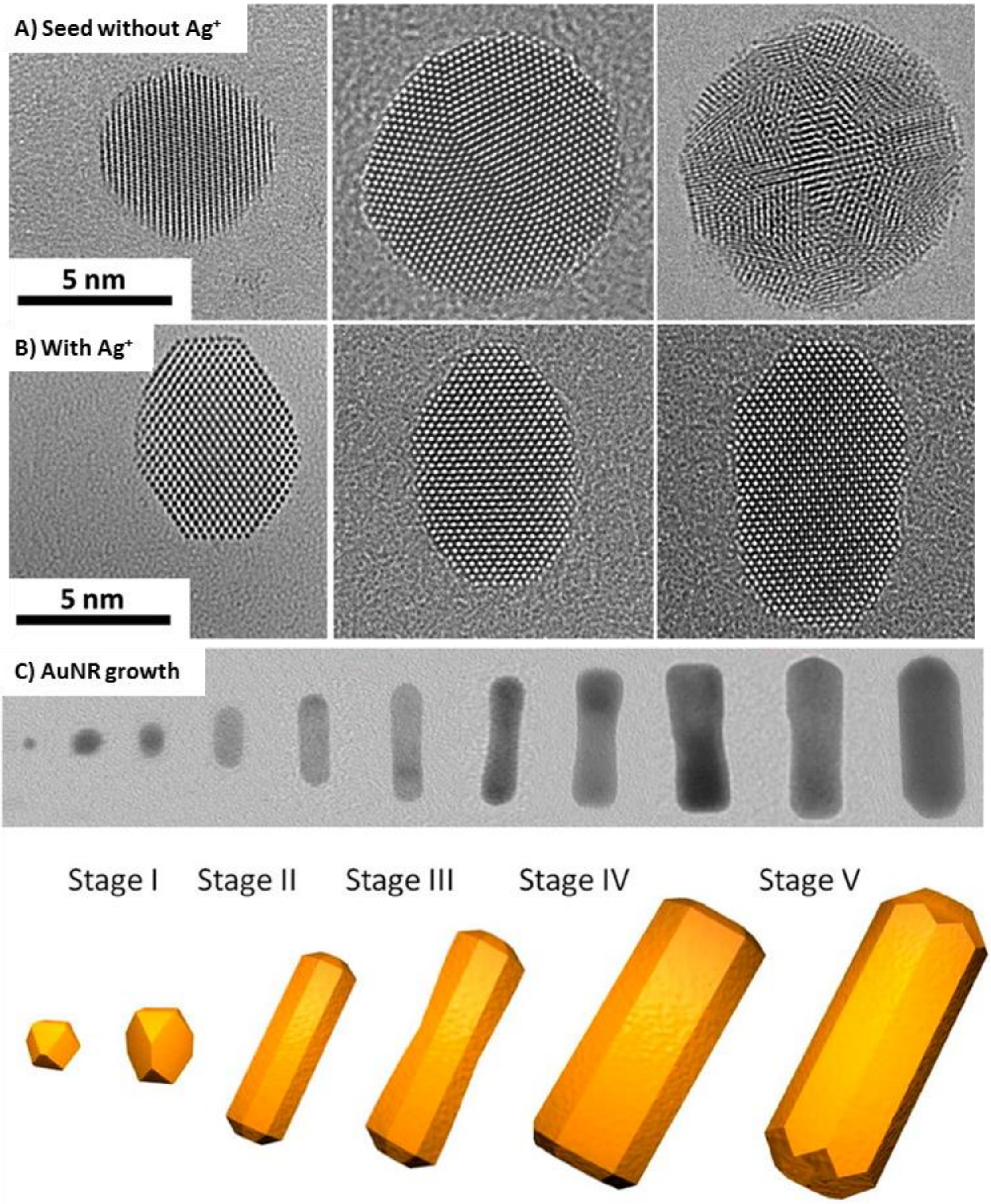

**Figure 1.4.-** A) Gold seed particles overgrown in the absence of $Ag^+$ remain spherical and may become twinned or multiply twinned, B) Au seeds overgrown in the presence of $Ag^+$ are observed to become anisotropic, C) Schematic and TEM images of the evolution of AuNR morphology after seed addition. Adapted from [19,20].

#### 1.1.1.2.2. Synthesis of Other Anisotropic Nanoparticles

As mentioned above, the origin of symmetry breaking of spherical seeds into anisotropic NP remains controversial. It is clear however that additives such as silver or halide ions present in the growth medium control the formation of crystallographic planes on the growing seed that will eventually lead to the formation of anisotropic NP. Recently, Mirkin *et al.*[22] investigated the role of halides, silver concentration, and growth rate on the final shape of AuNPs (Figure 1.5). They found that halides can play three roles during the synthesis of the specific shapes they studied: (1) modulation of the reduction potential of ionic gold prior to seed addition (Figure 1.5A), (2) passivation of the AuNP surface (Figure 1.5A), and (3) in silver-assisted syntheses, halides also modulate the extent of silver underpotential deposition (Figure 1.5B,C). The underpotential deposition process is affected by both $Ag^+$ concentration (Figure 1.5B) and the presence of halides (Figure 1.5C). For further details on the halide effect on crystal growth a review has been recently published by our group in collaboration with Murphy's group,[23] where the role of halide and silver ions in anisotropic metal nanoparticle synthesis is thoroughly discussed.

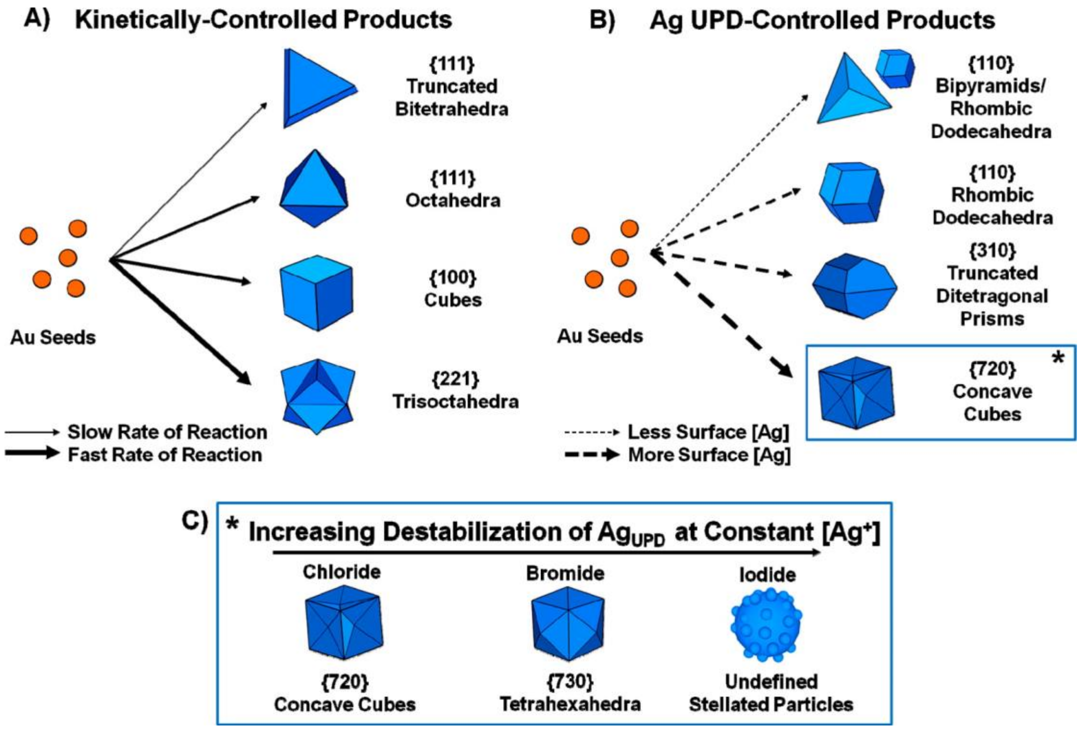

**Figure 1.5.-** Scheme illustrating how halides and silver ions can be used to direct the growth of gold seeds down different growth pathways to yield different shaped products: (A) kinetically controlled products in the absence of silver ions; (B) Ag underpotential deposition-controlled products where the interactions of silver with the particle surface dictate product shape; (C) effect of varying the stability of the Ag UPD layer with high concentrations of chloride, bromide, or iodide in the growth solution, yielding concave cubes, tetrahexahedra, and stellated particles, respectively. Adapted from [22].

### 1.1.2. Optical properties of Nanometals

AuNPs can be classified into three types according to their size and size-dependent properties: less than 2 nm, 2-10 nm, and 10-300 nm. Particles smaller than 2 nm in diameter are called “gold clusters”, which consist of few tens to a few hundreds of gold atoms. When the particle size is less than 5 nm, surface properties exceed inherent features of the material, determining its physical properties. Particles with sizes of 10-300nm have received a great deal of attention due to their extraordinary intrinsic physical properties. They exhibit characteristic colors and unusual optical properties that strongly depend on their size, shape, and the dielectric constant of the surrounding medium. The characteristic color of AuNPs derives from a phenomenon termed localized surface plasmon resonance (LSPR).[24,25] When electromagnetic radiation of an appropriate wavelength interacts with a metallic nanostructure, the conduction electrons near a metal–dielectric interface will be excited and undergo a collective oscillation relative to the lattice of positively charged nuclei, with the frequency of the incoming light resulting in a LSPR (Figure 1.6A). A momentary electric field is generated on the surface of the NP as a result of the oscillations. This can extend into the dielectric over nanometer lengths and hence give rise to an enhancement of the incident field by several orders of magnitude, resulting in novel properties of NPs (for a review on the subject see e.g. [26]).

At the beginning of the 20th century Gustav Mie proposed a theory that was able to explain the spectral properties of spherical particles.[27] The theory showed that the total extinction cross-section comprises contributions from the scattering and absorption cross-sections, i.e. the extinction cross-section, $\sigma_{\mathrm{ext}} = \sigma_{\mathrm{abs}} + \sigma_{\mathrm{scat}}$ (absorption cross-section + scattering cross-section). When the size of the NP is significantly smaller than the wavelength of light ($\lambda \gg 2r$, where $r$ is the radius of the NPs), Mie's theory reduces to:

$$\sigma_{\mathrm{ext}}(\omega) = 9\frac{\omega}{c}\varepsilon_{\mathrm{m}}^{\frac{3}{2}}V\frac{\varepsilon_2(\omega)}{[\varepsilon_1(\omega) + 2\varepsilon_{\mathrm{m}}]^2 + \varepsilon_2(\omega)^2} \qquad [1.1]$$

where $V$ is the volume of the particle $\left[\frac{4\pi}{3}r^3\right]$, $\omega$ is the angular frequency of the exciting light, $c$ is the velocity of light, $\varepsilon_{\mathrm{m}}$ is the dielectric function of the medium surrounding the NPs, and $\varepsilon_1$, $\varepsilon_2$ are the real and imaginary parts of the dielectric function of the NPs, respectively, i.e. $\varepsilon(\omega) = \varepsilon_1(\omega)+i\varepsilon_2(\omega)$. The resonance condition is $\varepsilon_1(\omega)=-2\varepsilon_m$, if $\varepsilon_2$ is small and is a weak function of $\omega$. For Au NPs in water, this can happen around $\lambda$ = 520 nm.

This theory was remodeled by Gans in order to explain the properties of other shapes (oblate and prolate spheroidal particles).[28] As mentioned above, it is important to note that the details of the LSPR response of metal nanostructures depend on different variables such as the size or the shape. AuNRs are classical examples to demonstrate the shape dependent LSPR properties. Unlike nanospheres (which have only one well-defined plasmon resonance peak), AuNRs display two plasmon bands in the visible/near-infrared (NIR) regions (Figure 1.6B) that are tunable depending on the dimensions, i.e. AuNR aspect ratio. According to theoretical calculations, the first band near 530 nm (called transverse LSPR) is due to electron oscillation perpendicular to the long axis of the NR whereas the second band, at a longer wavelength (called longitudinal LSPR mode) is assigned to an oscillation parallel to the long axis (Figure 1.6C). For other anisotropic NPs such as nanotriangles, LSPRs are split into distinctive dipole and quadrupole plasmon modes.[29]

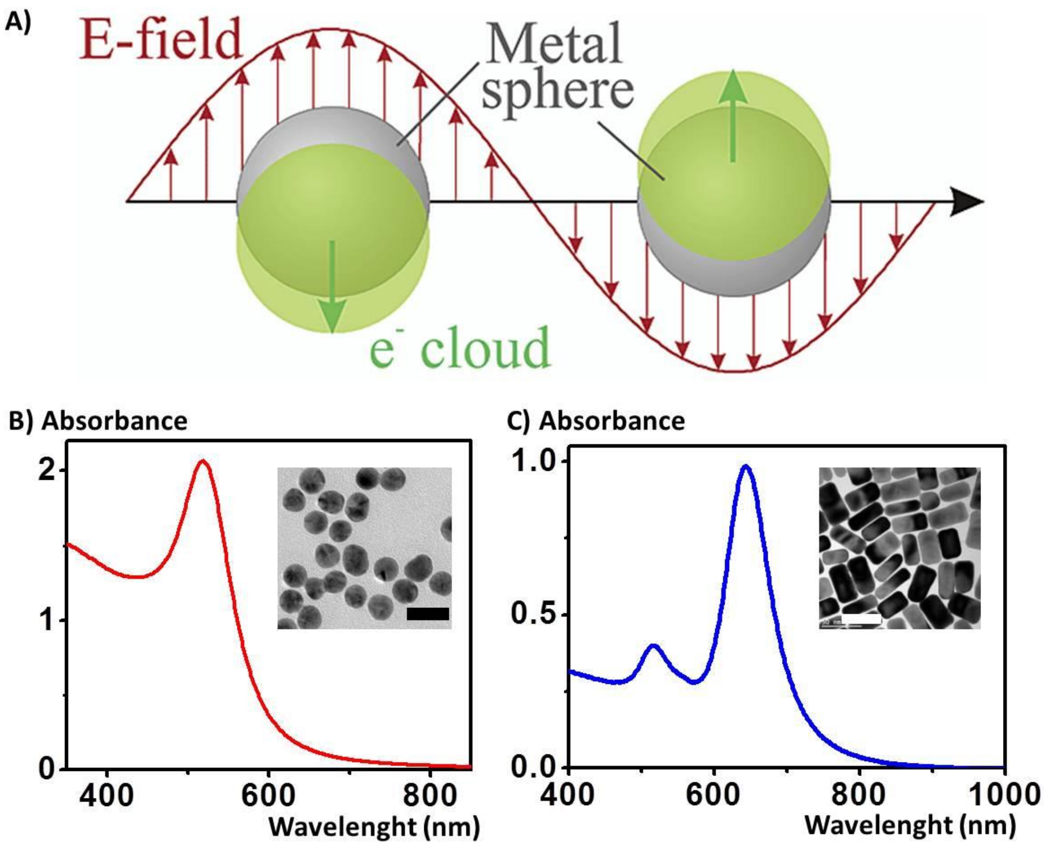

**Figure 1.6.-** A) Schematic representation of a plasmon oscillation in a metal sphere, showing the displacement of the conduction electron cloud relative to the nuclei. B,C) Absorption spectra of gold nanospheres and AuNRs, respectively. Corresponding TEM images of spherical and rod-shaped gold nanoparticles are shown as insets. Adapted from [30].

## 1.2. Mesoporous Silica Nanoparticles with Molecular Gates

Gated materials are nanosystems that usually contain two principal components: (i) a switchable "gate-like" ensemble capable of being "opened" or "closed" upon the application of certain external stimuli; (ii) a suitable inorganic support acting as a nanocontainer loading the carrier, to which gate-like molecules can be easily grafted, in this case mesoporous silica (see Figure 1.7). The selection of these components determines the controlled release performance of the hybrid support. Mesoporous silica of different pore sizes and morphologies are usually selected as inorganic scaffolds in gated ensembles because they show a very large load capacity, homogeneous porosity, and high inertness, which make them easy to functionalize.

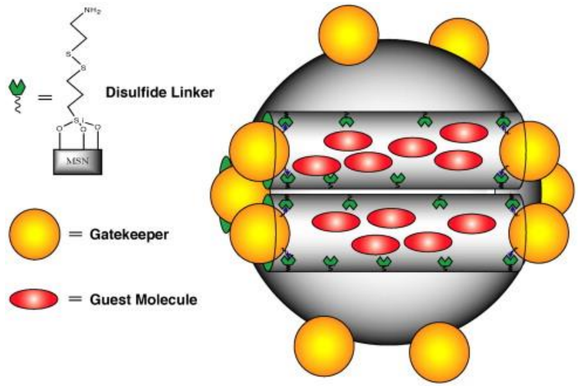

**Figure 1. 7.-** General representation of a mesoporous silica nanoparticle containing guest molecules (cargo) and a gate-like ensemble consisting of a gatekeeper attached to a disulfide linker. In this example, the gate could be opened at will by cleaving the disulfide bond with various disulfide reducing agents, such as dithiothreitol (DTT). Adapted from [42].

### 1.2.1. Synthesis of Mesoporous Silica Nanoparticles

Since the discovery of mesoporous silicas synthesized using cationic surfactants as templates, the templating method has been widely applied to prepare mesoporous silicas with high surface areas, tunable pore sizes, large pore volumes and rich morphology.[31,32] A large number of studies have focused on the interactions between surfactants and silica species in order to prepare specific mesoporous silicas. Mesostructural surfactant–silica nanocomposites spontaneously assemble through interaction of the organic and inorganic components. In addition to thermodynamics of the surfactant–silica assembly, the morphologies and dimensions of the resulting materials are particularly dependent on the kinetics of sol–gel chemistry (such as the reaction temperature, water content, and pH value of the reaction solution). With a careful control of the self-assembly and silica condensation rate, it is possible to tailor the sizes, mesostructures and morphologies of the mesoporous silica.[33]

The most widely used type of mesoporous silica nanoparticles (MSN) is MCM-41, composed of ordered hexagonally arranged cylindrical mesopores.[34,35] Since its introduction by the Mobil company as micrometer-sized amorphous aggregates, MCM-41 has evolved from submicrometer spheres,[36] to MSN of less than 100 nm.[37,38] The synthesis of MCM-41 involves liquid crystal templating using an alkylammonium salt, commonly cetyl trimethylammonium bromide (CTAB), soluble silica precursors (usually TEOS or sodium metasilicate) and alkali as catalyst. In aqueous solution, above the critical micelle concentration, amphiphilic surfactant molecules self-assemble into spherical micelles. Around the polar head region of the micelles, silica is condensed on the surfactant and forms a silica wall around the surface of the micelles. Subsequent removal of the surfactant template by calcination under oxidizing atmosphere results in the mesoporous product.[39] For further details on the synthesis see chapter 4.

### 1.2.2. Molecular Gates and Controlled Release

Concerning gated silica NP, several capping molecular and supramolecular systems are able to bind on the silica surface enclosing a compatible cargo that has been previously loaded into the mesoporous silica. External stimuli such as light, pH, changes in redox potential, temperature, and the presence of certain ions, molecules, or biomolecules can bind the capping molecule triggering a molecular conformational change that allows the cargo to diffuse out to the medium.[40-44] The design of gated mesoporous materials is thus based on both nanoscopic gating solids and molecular, biomolecular, or supramolecular concepts.

One of the first examples of a controlled gated support for delivery described in the literature was based on an MCM-41 mesoporous silica containing linear polyamines grafted onto the outer surface and loaded with the dye $[Ru(bipy)_3]^{2+}$.[45] The open–close protocol in this system is studied by means of the protonation of the polyamines. At a neutral pH, polyamines are mostly unprotonated, allowing the release of the entrapped dye. However at an acidic pH nitrogen atoms of the polyamine are protonated and adopt a rigid-like conformation (due to the Colulombic repulsions between ammonium groups), resulting in a partial pore blockage and the subsequent dye release inhibition (Figure 1.8A). Following this strategy, different solids consisting of MCM-41 mesoporous material loaded with dyes and functionalized with different molecules on the external surface were prepared. As reported by Martínez-Mañez and his group,[46-48] pH, light and temperature were the first external stimuli used to trigger the release of molecular cargo. However, in a further evolution and aiming to find applicability to this system, several strategies using biomolecules as external stimuli have been designed mainly for on-command drug delivery in cells and tissues,[49] and to a lesser extend for biosensing. Note that the use of MSN for the development of biosensors is still uncommon and very few examples are available. In this sense, new approaches based on the detection of oligonucleotides have been recently demonstrated.[50,51] As in the previous cases, the sensing material is prepared with mesoporous nanoparticles loaded with a dye (e.g. fluorescein), functionalized on the outer surface with (3-aminopropyl) triethoxysilane, and capped with an oligonucleotide, which remains attached to the nanoparticle surface via electrostatic interactions with the partially protonated amines (see Figure 1.8B). Interestingly, the aqueous suspensions of these nanoparticles (pH 7.5) have been demonstrated to be rapid, highly sensitive and very selective to the presence of the complementary single strand, thus allowing one to detect the presence of pathogenic DNA in the medium.

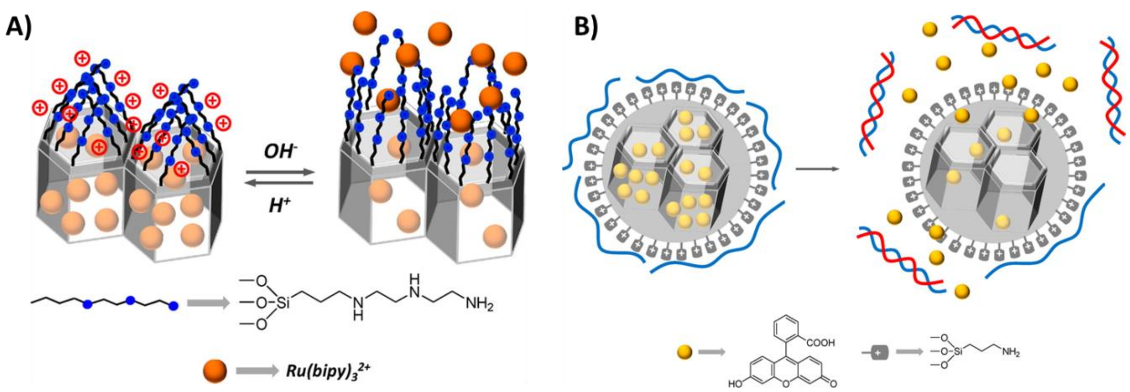

**Figure1.8.-** Schematic representation of: A) MCM-41 mesoporous silica containing polyamines grafted onto the outer surface and loaded with the dye $[Ru(bipy)_3]^{2+}$ . At a neutral pH, polyamines are unprotonated, allowing the release of the entrapped dye. B) MCM-41 functionalized with 3-aminopropyltriethoxysilane and capped with a single-stranded oligonucleotide. Delivery of fluorescein is selectively accomplished in the presence of the complementary oligonucleotide. Adapted from [52].

## 1.3. Nanoparticles for Biodetection

The development of highly sensitive and cost-effective biosensors has attracted significant interest from the scientific community over the last decade. The unique optoelectronic properties of nanomaterials can be of great utility in creating new biological sensors. Among the wide variety of inorganic nanoparticles that are currently used for biological applications (see Figure 1.9), plasmonic nanoparticles offer many advantages in biology and biomedical research due to their unique feature, that is, displaying localized surface plasmon resonance (LSPR) bands in the UV–visible-near IR spectral range. The LSPR frequency is extremely sensitive to subtle changes in the physicochemical environment, for example, the distance between nanoparticles,[53] and is also characteristic of their size and shape. Remarkably, in some cases the associated plasmon shift is so dramatic that a color change can be read out by the naked eye and does not require expensive or sophisticated instrumentation.[54] Plasmonic nanoparticles are mainly based on Au or Ag cores because they can be easily produced in different shapes and sizes. The surface chemistry of plasmonic nanoparticles is well-known and widely advanced, hence biofunctionalization can be effectively performed.[55] Regarding biosensing, plasmonic nanoparticles are perfect candidates for the fabrication of colorimetric sensors since they can be used as both recognition elements and transducers. The recognition element provides selective/specific binding with the target analyte while the transducer signals the binding event. In addition, LSPRs give rise to huge electromagnetic fields at the nanometal surface upon the excitation with light of appropriate energy.[56] This phenomenon allows one to detect molecules located near the metallic NP by Raman spectroscopy in a very sensitive way (see below).

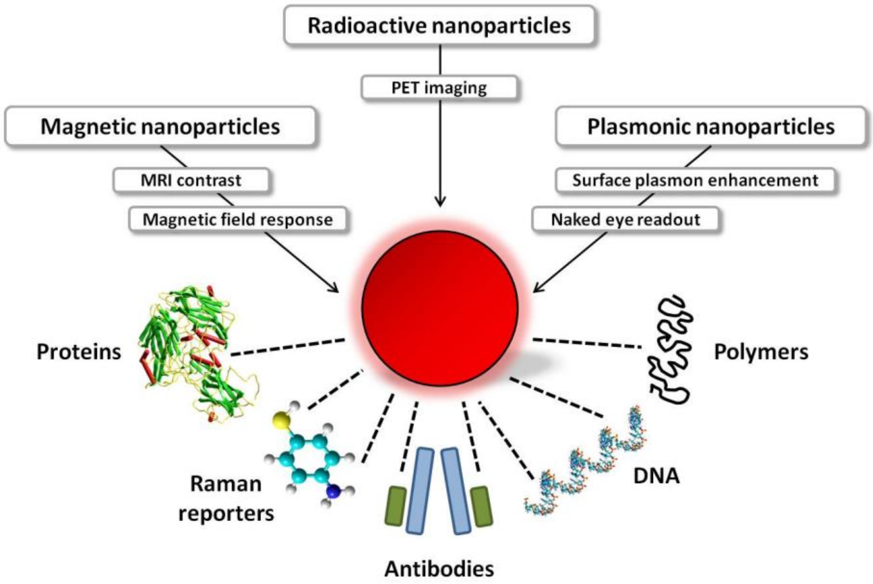

**Figure 1.9.-** Examples of application of nanoparticles for biodetection. Inorganic nanoparticles display different capabilities depending on the chemical composition of their cores and their functionalization. With the ever-growing use of nanoparticles in biomedicine, standard ligands (mostly alkanethiols terminated by a simple organic functional group) are replaced by biologically active molecules such as proteins or enzymes. Adapted from [57].

### 1.3.1. Metal Nanoparticles and Enzymes for Colorimetric Detection

Colorimetric assays are generally based on an absorbance shift in the UV-vis spectrum of colloid particles that can be modified through changes in the size, shape and state of aggregation of the NP. In this regard, AuNPs have become the most widely studied metal nanoparticle due to their tunability and chemical stability over time. The first and most popular example of the use of AuNP for colorimetric detection was demonstrated by Mirkin et al. back in 1996.[58] The authors fabricated red colloids containing AuNPs functionalized with thiolated DNA strands that became blue in the presence of a target oligonocleotide. In this process, complementary DNA strands hybridize with each other, inducing the aggregation of the AuNP with the concomitant color change (Figure 1.10). After publication of this mechanism, the number of works using AuNP for biodetection has been steadily growing with a notable expansion during the past five years.[59-62]

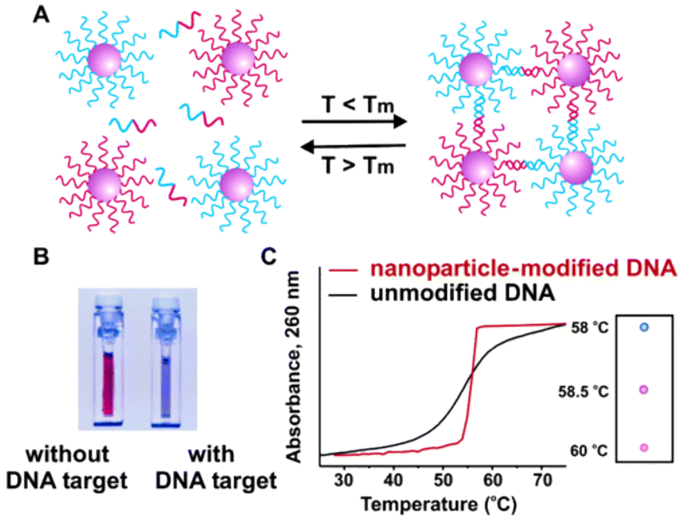

**Figure 1.10.-** In the presence of complementary target DNA, oligonucleotide-functionalized gold nanoparticles aggregate (A), resulting in a change of solution color from red to blue (B). The aggregation process can be monitored using UV−vis spectroscopy or simply by spotting the solution on a silica support (C). Adapted from [58].

Besides DNA, the use of other biological moieties such as enzymes has been recently demonstrated to be very effective for the detection of biomolecules. An important contribution in this respect was reported by Pavlov et al. for the detection of nerve gases by modulating the growth of AuNP through the enzymatic activity of acetylcholinesterase (AChE) – a hydrolytic enzyme present in the human nervous system that decomposes acetylcholine into acetate and choline. However, spherical nanoparticles present limited performance as biosensors since they exhibit a single plasmon resonance band. In this sense, anisotropic NPs such as AuNR have been demonstrated to be better candidates for biosensing due to the different colors they exhibit in the visible when changing their aspect ratio (See Figure 1.11). Thus, AuNR are preferred for biosensing, imaging and diagnosis.[63-65] In general, according to the biomolecule detected using AuNRs or other AuNPs we can divide the different existing approaches in 4 categories, namely, 1) sensing of DNA and oligonucleotides, 2) protein detection, 3) heavy metal ions detection, and 4) sensing of glucose and other biological-related molecules. Good examples of all these categories can be found in a recent review by Saha *et al.*[66]

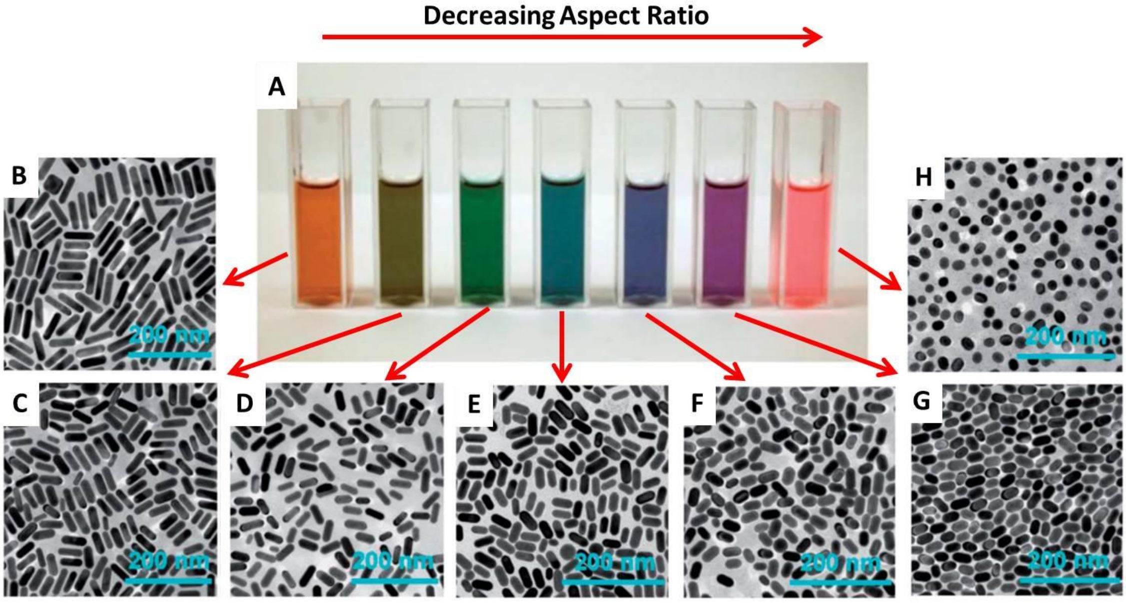

**Figure 1.11.-** A) Photographs of aqueous solutions of gold nanorods with different aspect ratios. B-H) TEM images of the corresponding nanoparticles; all scale bars = 200 nm. The difference in color of the AuNR solutions is dramatic due to the nature of the plasmon bands, which are very sensitive to aspect ratio. Adapted from [67].

### 1.3.2. Metal Nanoparticles for Surface Enhanced Raman Scattering (SERS)

Surface enhanced Raman scattering (SERS) was first observed in 1974 for pyridine adsorbed on a silver electrode,[68] but the phenomenon was not correctly interpreted until 1997.[69] The observation of single-molecule SERS by two different groups[70,71] stimulated the interest of the scientific community on this technique triggering the rapid development of SERS during the past few decades. SERS is a molecular ultrasensitive technique based on the plasmon-assisted scattering of molecules on or near metal nanostructures. In other words, SERS combines the molecular specificity of vibrational Raman spectroscopy with high sensitivity due to plasmon assisted scattering.[72] Hence, both the chemical nature of the molecule and the position of the molecule with respect to the nanostructure are crucial to obtain a good SERS signal. Molecules with high Raman cross-section show a high SERS signal. The cross section of a molecule for a given linear optical process can be defined as the signal intensity produced by this process compared to the incident power density.[73] But even when the cross section of a given molecule is very high, the highest intensity is obtained when the target molecule is in close contact to the plasmonic surface of the metal nanoparticle, and the intensity decreases exponentially with distance.[74] In addition, the presence of the molecule at a hot spot (highly localized region exhibiting extreme field enhancement) can also contribute to determine the sensitivity of this technique (Figure 1.12). Therefore, best SERS performance is achieved when using molecules with high affinity to a metal nanoparticle that in turn presents a high electromagnetic enhancement.

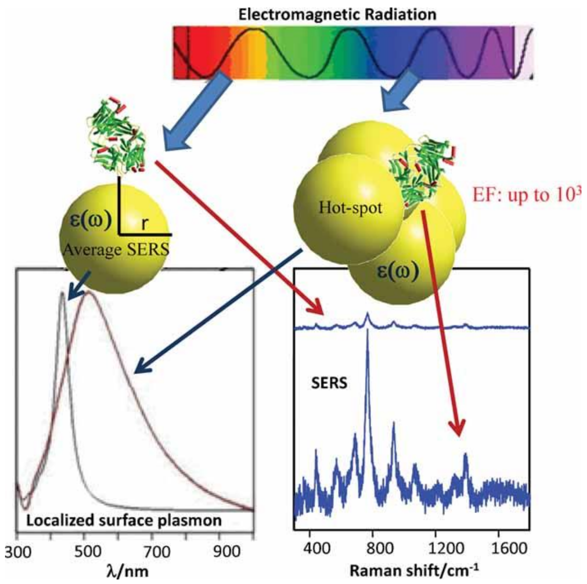

**Figure 1.12.-** Schematic view of SERS on both non-interacting nanoparticles and aggregates. Non-interacting nanoparticles display well-defined LSPRs but these broaden and red-shift in aggregates due to electromagnetic coupling. Coupling also leads to the formation of hot spots, with large effects on the intensity of the SERS signal (additional enhancement factors up to $10^3$). Adapted from [75].

In this context, the most employed metals in SERS are gold and silver. Although better SERS performance is obtained for Ag nanoparticles, AuNP are more extensively used for SERS biosensing and other bio-applications due to their high chemical stability, low reactivity and lack of cytotoxicity. In fact, a plethora of amazing applications involving SERS have been recently developed, especially in the fields of diagnostics, biodetection, and bioimaging.[76,77] One of the hot topics in using SERS for biodetection is how to design nanoparticles that are biocompatible and yet keep the integrity of SERS signal detectable and informative. To achieve this objective, big efforts in surface chemistry have been performed giving rise to new experimental procedures that allow one to obtain spectroscopic information in very complex media.[78] As a recent example of this feature, Xie *et al.* were able to register specific SERS signals coming from gold nanoparticles internalized by a living cell.[79] The AuNPs were functionalized with Alexa Fluor

750, a widely used dye when working with SERS for exhibiting high levels of cell uptake. Afterwards, tris(2-carboxyethyl)phospine, a highly effective quencher of the Raman signal that cannot cross the cell membrane was added. This two-step process guaranteed that the signal of the AuNP laying outside the cell was quenched and thus, the acquired SERS signal was exclusively coming from NP inside the living cell. Undoubtedly, this and other approaches will be further explored and very likely SERS will become an indispensable tool for sensing and diagnosis in the near future.

## 1.4. References

[1] W. M. Haynes, (2014). CRC Handbook of Chemistry and Physics (pp 12-41) Boca Raton: CRC press.
[2] L. M. Liz-Marzán, Mater. Today, 7 (2004) 26.
[3] N. Lewinski, V. Colvin, R. Drezek. Small 4 (2008) 26.
[4] H. Liao, C. L. Nehl, J. H. Hafner. Nanomedicine 1 (2006) 201.
[5] M. Faraday, Philos.Trans. R. Soc. 147 (1857) 145.
[6] C. Louis, O. Pluchery, (2012). Gold nanoparticles for physics, chemistry and biology (pp. 106-124). London: Imperial College Press.
[7] J. M. Ha, A. Solovyov, & A. Katz. Langmuir, 25 (2009) 10548.
[8] J. Turkevich, P.C. Stevenson, J. Hillier. Discuss. Faraday Soc. 11 (1951)55
[9] R. Gans, Ann. Phys. 47 (1915) 270.
[10] T. K. Sau, C.J. Murphy, J. Am. Chem. Soc. 126 (2004) 8648.
[11] N. R. Jana, L. Gearheart, C.J. Murphy, Adv. Mater. 13 (2001) 1389.
[12] B. Nikoobakht, M.A. El-Sayed, Chem. Mater. 15 (2003) 1957.
[13] K. R. Brown, D. G. Walter, M. J. Natan, Chem. Mater. 12 (2000) 306
[14] C. J. Murphy, T. K. Sau, A. M. Gole, C. J. Orendorff, J. Gao, *et al.* The J. Phys. Chem. B. 109 (2005) 13857.
[15] A. Gole, C. J. Murphy, Chem. Mater., 16 (2004) 3633.
[16] M. Liu, P. Guyot-Sionnest, J. Phys. Chem. B. 109 (2005) 22192.
[17] J. Stone, S. Jackson, D. Wright, WIREs: Nanomed. Nanobiotechnol. 3 (2011) 100.
[18] J. Pérez-Juste, I. Pastoriza-Santos, L. M. Liz-Marzán, P. Mulvaney, Coord. Chem. Rev. 249 (2005) 1870
[19] M. J. Walsh, S. J. Barrow, W. Tong, A. M. Funston, J. Etheridge, ACS Nano, 9 (2005) 715.
[20] K. Park, L. F. Drummy, R. C. Wadams, H. Koerner, D. Nepal, L. Fabris, R. A. Vaia, Chem. Mater. 25 (2013) 555.
[21] M. Grzelczak, J. Pérez-Juste, P. Mulvaney, L. M. Liz-Marzán, Chem. Soc. Rev. 37(2008) 1783.
[22] M. R. Langille, M. L. Personick, J. Zhang, C. A. Mirkin, J. Am. Chem. Soc, 134 (2012) 14542.
[23] S. E. Lohse, N. D. Burrows, L. Scarabelli, L. M. Liz-Marzán, C. J. Murphy, Chem. Mater. 26 (2013) 34.
[24] K. A. Willets, R. P. Van Duyne, Annu. Rev. Phys. Chem. 58 (2007) 267.
[25] P. K. Jain, X. Huang, I. H. El-Sayed, M. A. El-Sayed, Acc. Chem. Res. 41 (2008) 1578.
[26] M. A. Garcia, J. Phys. D: Appl. Phys. 44 (2011) 283001.
[27] G. Mie, Annalen der physik, 330 (1908) 377.
[28] R. Gans, Annalen der Physik, 342 (1912) 881.
[29] J. Nelayah, M. Kociak, O. Stéphan, F. J. G. de Abajo, M. TencéHenrard, *et al.* Nature Phys. 3 (2007) 348.
[30] K. L. Kelly, E. Coronado, L. L. Zhao, G. C. Schatz, J. Phys. Chem. B. 107 (2003) 668.

[31] C. T. Kresge, M. E. Leonowicz, W. J. Roth, J. C. Vartuli, J. S. Beck, Nature 359 (1992) 710.
[32] T. Yanagisawa, T. Shimizu, K. Kuroda, C. Kato, Bull. Chem. Soc. Jpn., 63 (1990) 988.
[33] S. H. Wu, C. Y. Mou, H. P. Lin, Chem. Soc. Rev. 42 (2013) 3862.
[34] C. T. Kresge, M. E. Leonowicz, W. J. Roth, J. C. Vartuli, J. S. Beck. Nature. (1992) 710.
[35] J. S. Beck, J. C. Vartuli, W. J. Roth, M. E. Leonowicz, C. T. Kresge, K. D. Schmitt, C. T. W. Chu, D. H. Olson, E. W. Sheppard. J. Am. Chem. Soc. 114 (1992) 10834.
[36] M. Grün, I. Lauer, K. K. Unger. Adv. Mater. 9 (1997) 254.
[37] H. Meng, M. Xue, T. Xia, Z. Ji, D. Y. Tarn, J. I. Zink, A. E. Nel. ACS Nano 5 (2011) 4131.
[38] Y-S. Lin, C. L. Haynes, J. Am. Chem. Soc.;132 (2010) 4834.
[39] S. H. Wu, Y. Hung, C. Y. Mou,). Chem. Commun. 47 (2011) 9972.
[40] B. G. Trewyn, I. I. Slowing, S. Giri, H. T. Chen, V. S.-Y. Lin,. Acc. Chem. Res. 40 (2007) 846.
[41] I. I. Slowing, B. G. Trewyn, S. Giri, V. S.-Y. Lin, Adv. Funct. Mater. 17 (2007) 1225.
[42] I. I. Slowing, J. L. Vivero-Escoto, C. W. Wu, V. S.-Y. Lin, (2008). Adv. Drug Deliv. Rev. 60 (2008) 1278.
[43] R. Klajn, J. F. Stoddart, B. A. Grzybowski, Chem. Soc. Rev. 39 (2010) 2203.
[44] F. Tang, L. Li, D. Chen, Adv. Mater. 24 (2012) 1504.
[45] R. Casasús, E. Climent, M. D. Marcos, R. Martínez-Máñez,; F. Sancenón, J. Soto, P. Amorós, J. Cano, E. Ruiz, J. Am. Chem. Soc. 130 (2008) 1903.
[46] E. Aznar, R. Casasús, B. García-Acosta, M. D. Marcos, R. Martínez-Máñez, F. Sancenón, J. Soto, P. Amorós, Adv. Mater. 19 (2007) 2228.
[47] E. Aznar, M. D. Marcos, R. Martínez-Máñez, F. Sancenón, J. Soto, P. Amorós, C. Guillem, J. Am. Chem. Soc., 131 (2009) 6833.
[48] E. Aznar, L. Mondragón, J. V. Ros-Lis, F. Sancenón, M. D. Marcos, R. Martínez-Máñez, J. Soto, E. Pérez-Payá, P. Amorós Angew. Chem., Int. Ed. 50 (2011) 11172.
[49] K. M. L. Taylor-Pashow, J. Della Rocca, R. C. Huxford, W. Lin, Chem. Commun. 46 (2010) 5832.
[50] E. Climent, R. Martínez-Máñez, F. Sancenón, M. D. Marcos, J. Soto, A. Maquieira, P. Amorós, Angew. Chem., Int. Ed. 49 (2010) 7281.
[51] E. Climent, L. Mondragón, R. Martínez-Máñez, F. Sancenón, M. D. Marcos, J. R. Murguía et al. Angew. Chem., Int. Ed. 52 (2013) 8938.
[52] C. Coll, A. Bernardos, R. Martínez-Máñez, F. Sancenón. Acc. Chem. Res. 46 (2012) 339.
[53] P. K. Jain, M. A. El-Sayed, Chem. Phys. Lett. 487 (2010) 153.
[54] Y. Song, W. Wei, X. Qu, Adv. Mater. 23(2011), 4215-4236.
[55] R. M. Fratila, S. G. Mitchell, P. del Pino, V. Grazu, J. M. de la Fuente. Langmuir, 30 (2014) 15057.
[56] U. Kreibig, M. Vollmer, (1995). Optical properties of metal clusters. Theoretical Considerations. Springer Berlin Heidelberg.
[57] J. J. Giner-Casares, M. Henriksen-Lacey, M. Coronado-Puchau, L. M. Liz-Marzán. Mater. Today. 10.1016/j.mattod.2015.07.004

[58] C. A. Mirkin, R. L. Letsinger, R. C. Mucic, J. J. Storhoff, Nature, 382 (1996) 607.

[59] H. Jans, Q. Huo, Chem. Soc. Rev. 41 (2012) 2849.

[60] R. R. Arvizo, S. Bhattacharyya, R. A. Kudgus, K. Giri, R. Bhattacharya, P. Mukherjee, Chem. Soc. Rev. 41 (2012) 2943.

[61] G. Doria, J. Conde, B. Veigas, L. Giestas, C. Almeida, M. Assunção, *et al.* Sensors, 12 (2012) 1657.

[62] P. D. Howes, R. Chandrawati, M. M. Stevens, Science, 346 (2014) 1247390.

[63] E. T. Castellana, R. C. Gamez, D. H. Russell, J. Am. Chem. Soc. 133 (2011) 4182.

[64] S. Mallick, I. C. Sun, K. Kim D. K. Yi, J. Nanosci. Nanotechol. 13 (2013) 3223.

[65] W. I. Choi, A. Sahu, Y. H. Kim, G. Tae, Ann. Biomed. Eng. 40 (2012) 534.

[66] K. Saha, S. S. Agasti, C. Kim, X. Li, V. M. Rotello, Chem. Rev. 112 (2012) 2739.

[67] Y. Zheng, M. Xiao, S. Jiang, F. Ding, J. Wang. Nanoscale 2 (2013) 788.

[68] M. Fleischmann, P. J. Hendra, A. J. McQuillan, Chem. Phys. Lett. 26 (1974) 163.

[69] D. L. Jeanmaire, R. P. Van Duyne, J Electroanal. Chem. Interfacial Electrochem. 84 (1977) 1.

[70] S. Nie, S. R. Emory, Science, 275 (1997) 1102.

[71] K. Kneipp, Y. Wang, H. Kneipp, L. T. Perelman, I. Itzkan, R. R. Dasari, M. S. Feld, Phys. Rev. Lett, 78 (1997) 1667.

[72] S. Schlücker, Angew. Chem., Int. Ed. 53(2014) 4756.

[73] R. A. Alvarez-Puebla, L. M. Liz-Marzán, Angew. Chem., Int. Ed. 51 (2012) 11214.

[74] G. J. Kovacs, R. O. Loutfy, P. S. Vincett, C. Jennings, R. Aroca, (). Langmuir, 2 (1986) 689.

[75] R. A. Alvarez-Puebla, L. M. Liz-Marzán, Small 6 (2010) 604.

[76] S. Abalde-Cela, P. Aldeanueva-Potel, C. Mateo-Mateo, L. Rodríguez-Lorenzo, R. A. Alvarez-Puebla, L. M. Liz-Marzán, J. R. Soc. Interface 7 (2010) S435.

[77] W. Xie, S. Schlücker, Phys. Chem. Chem. Phys. 15 (2013) 5329.

[78] D. Cialla, A. März, R. Böhme, F. Theil, K. Weber, M. Schmitt, J. Popp, Anal. Bioanal. Chem. 403 (2012) 27.

[79] H. N. Xie, Y. Lin, M. Mazo, C. Chiappini, A. Sánchez-Iglesias, L. M. Liz-Marzán, M. M Stevens, Nanoscale, 6 (2014) 12403.

# 2. Enzymatic Modulation of Gold Nanorod Growth and Application for Nerve Gas Detection

*ABSTRACT*

*In this chapter we describe the modulation of nanorod growth through the addition of an enzymatically-produced thiolated molecule. The enzyme acetylcholinesterase was selected because it hydrolyzes the substrate acetylthiocholine to produce the thiol-containing molecule thiocholine, in a controlled manner. UV–vis spectroscopic monitoring showed that the resulting localized surface plasmon resonance bands of the formed colloidal nanoparticles are highly sensitive to the concentration of thiocholine, while transmission electron microscopy allowed us to confirm that the observed optical changes arise from the evolution of the shape of the obtained gold nanoparticles from nanorods to cubes and finally to spheres, upon increasing the concentration of thiocholine. Hence, enzyme concentrations could be correlated with different plasmon bands and/or gold nanoparticle shapes. On the basis of this result, a simple colorimetric assay is proposed for the detection of subnanomolar concentrations of acetylcholinesterase inhibitors, which are close analogs of nerve gases.*

## 2.1. Introduction

Gold nanorods (AuNRs) are anisotropic metal nanoparticles that have been widely exploited for detection purposes due to their fascinating optical properties. This metal nanostructure can be easily synthesized by the seed mediated growth method.[1-5] In fact, this approach has become the preferred strategy by the scientific community for the synthesis of AuNRs. As detailed in the general introduction, it involves the addition of small seed particles of about 2 nm in diameter to a gold salt solution ($HAuCl_4$) containing cetyltrimethylammonium bromide (CTAB), silver nitrate and ascorbic acid. In this growth medium, the gold seeds catalyze the reduction of gold ions on their surface. It has been demonstrated that the adsorption of different moieties onto the metal surface can considerably affect the synthesis of this nanostructure. Morphological control, mainly through variation of the aspect ratio, has been reached by varying the concentration of silver nitrate and, to a lesser extent, of other parameters.[6] For example, the use of organic additives such as aromatic salicylates[7] and unsaturated fatty acids[8], which are weakly adsorbed to the gold surface, has been shown to inhibit growth on the lateral faces of the AuNRs, leading to preferential reduction on the tips. Thiol-containing molecules are another class of additives that can significantly affect the rate of the gold reduction on specific sites. Sodium sulfide[9], low-molecular weight alkanethiols [6] or thiolated polymers[10-12] have been used to quench the growth of AuNRs or to prevent reshaping once the growth was completed. However, the use of thiols as shape-controlling agents is rather difficult to implement, as the strong Au-S interaction often inhibits the catalytic properties of the gold surface and thus quenches the growth process[11]. A possible way to overcome this difficulty is to couple the seed-mediated growth of AuNRs to a reaction producing thiol additives in a controllable manner.

Acetylcholinesterase (AChE) is a hydrolytic enzyme that can decompose acetylthiocholine – a derivative of acetylcholine, which is a central neurotransmitter widely distributed in our nervous system – to generate the thiol-bearing compound thiocholine (TCh) [13]. Since the generation of such a thiolated molecule is directly controlled by the concentration of AChE, we hypothesized that the enzymatically produced TCh may be used to tune the growth of AuNRs. Indeed, we show in this communication that the growth of AuNRs is largely sensitive to the concentration of enzymatically produced TCh. Thus, depending on the experimental conditions of the enzymatic reaction, the final growth solution was found to contain a mixture of rods, cubes and spheres with controllable relative populations, strongly affecting the overall optical response of the system. As a consequence, different enzyme concentrations can be correlated with changes in localized surface plasmon resonance (LSPR) bands and/or gold NP shapes. We exploit this effect to develop a simple and highly sensitive colorimetric procedure for the subnanomolar detection of AChE inhibitors (down to 280 pM for paraoxon).

## 2.2. Results and Discussion

The proposed experimental approach involves three consecutive steps: 1) generation of small amounts of TCh by using the enzyme AChE to catalyze the hydrolysis of ATCh; 2) mixing the so-generated TCh with an Au seed solution; 3) transfer of this mixture into an AuNR growth medium (see Figure 2.1).

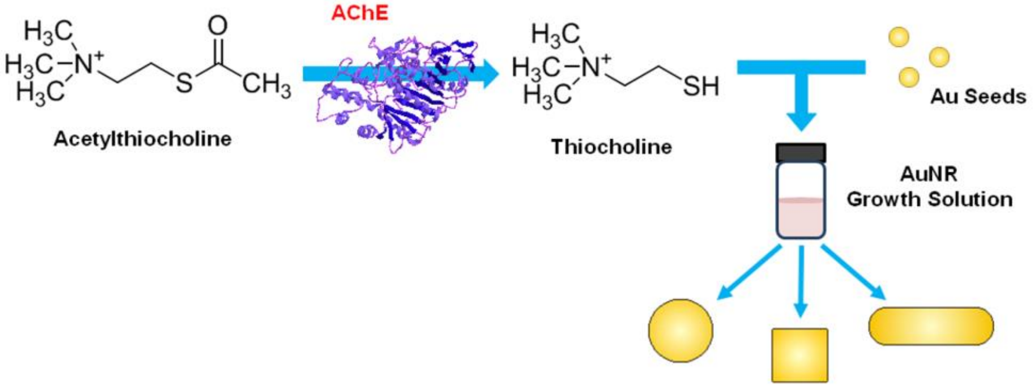

**Figure 2.1.-** Schematic representation of the modulation of seed-mediated gold nanorod growth. A fixed amount of a gold seed solution was incubated with different amounts of enzymatically produced thiocoline. The mixture was added to the growth solution, thereby producing nanoparticles with (mainly) three different shapes. With increasing amounts of TCh, the anisotropy of the produced NPs was decreased.

### 2.2.1.Concentration Threshold of Enzymatically Produced Thiols

Large amounts of enzymatically produced TCh were found to fully inhibit the autocatalytic reduction of gold ions on preformed seeds. As TCh is a suitable stabilizer for small gold nanoparticles [14-16], we expect that the CTAB bilayer around the seeds gets replaced by TCh to produce a compact cationic shell that prevents catalytic reduction of metal ions. To study the effect of TCh on the seed-mediated growth of AuNRs, we first defined the upper concentration limit of TCh at which only the shape of the final nanoparticles is modulated, rather than the total amount of reduced metal. The concentration of TCh was determined by a colorimetric assay (see experimental section). The temperature, substrate concentration and enzymatic reaction time were kept constant ([ATCh] = 0.05 mM, 15 min, 37 °C). Under these conditions, the amount of TCh that is produced depends exclusively on the amount of enzyme used in each experiment, which is measured in units of enzymatic activity, mU/mL. Thus, we can directly estimate the relationship between the amount of TCh and that of AChE. In a first set of experiments, different amounts of enzymatically produced TCh were incubated with a fixed concentration of seeds, and subsequently the autocatalytic reduction of gold ions was initiated. The total amount of reduced gold was estimated by UV-visible spectroscopy, assuming that the absorbance at $\lambda = 400$ nm corresponds to 0.5 mM of metallic gold [17]. For larger TCh amounts (> 0.3 mM), the reduction of gold is partially inhibited, suggesting TCh binding to the surface of the gold seeds, thereby preventing further gold reduction (Figure 2.2). Gradual decrease of TCh concentration increases the final concentration of metallic gold, leading to complete gold reduction when the concentration of added TCh is below 0.15 mM. This value corresponds to ca. 550 molecules per seed nanoparticle, assuming that the diameter of the seed is 2 nm. Within the concentration range of complete gold reduction, further decrease of TCh affects the final color of the solution and therefore the position of the LSPR bands. Simple inspection of the absorbance spectra allows us to see that meaningful LSPR bands are only registered for low TCh concentrations (up to 0.05 mM, [AChE] = 2 mU/mL, see Figure 2.2A). Varying the specific concentration of TCh in this range leads to significant changes in both the longitudinal and transverse LSPR bands, indicating that AuNR growth strongly depends on the amount of TCh present in the medium. This clear tendency confirms that TCh possesses a significant affinity toward the surface of the gold seeds, thereby affecting the formation of AuNRs. Thus, the effect of TCh on AuNR

growth was studied for concentrations below 1.5 mU/mL (yellow area in Figure 2.2B).

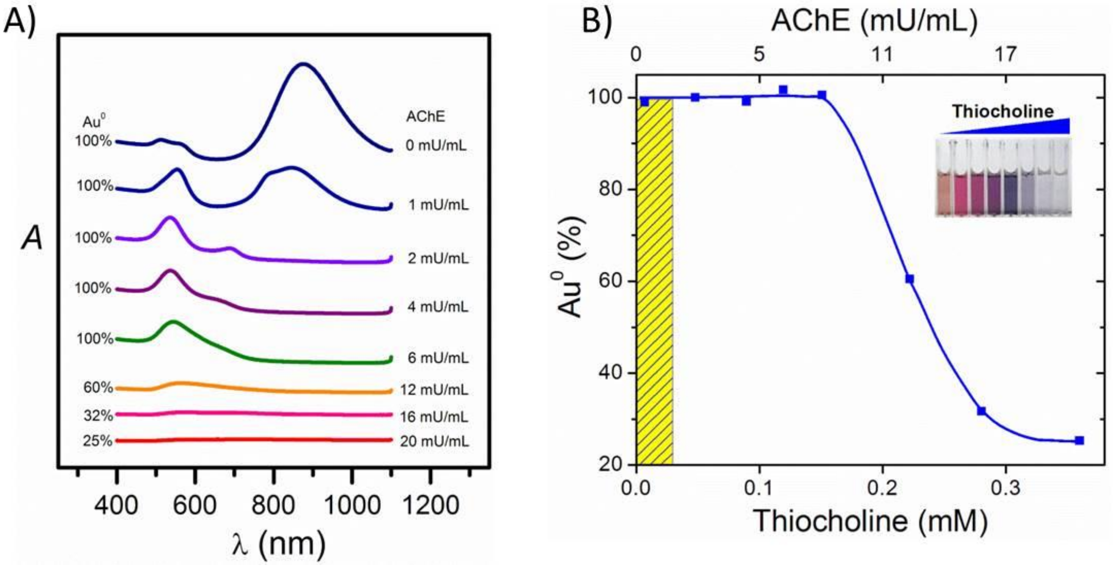

**Figure 2.2.-** A) Absorbance spectra of the growth products formed in the presence of 0.05 mM ATCh and different concentrations of AChE (right labels). The percentage of reduced gold (left labels) was estimated assuming that the absorbance at λ = 400 nm corresponds to 0.5 mM of metallic gold. B) Percentage of gold reduction upon addition of gold seeds, preincubated with varying concentrations of TCh. For these experiments, the concentration of AChE was varied, while temperature, substrate concentration and enzymatic reaction time were kept constant ([ATCh] = 0.05 mM, 15 min, 37 °C). Under these conditions the concentration of TCh (mM) can be correlated with the concentration of AChE (mU/mL) as follows: [TCh] = 0.017[AChE] + 0.016.

### 2.2.2.Enzymatically Tunable Growth of Gold Nanorods

In the selected low concentration range (Figure 2.2), increasing amounts of TCh were found to impair the regular growth of AuNRs and different NP shapes formed, as shown in Figure 2.3A. As more AChE was added to a 0.05 mM ATCh solution, the morphology of the growth products varied from rods to cubes and finally spheres. Statistical analysis from transmission electron microscopy (TEM) images was used to analyze the population of the different NP shapes present in the growth products (Figure 2.3B). Initially, without the addition of the enzyme, the large majority of the NPs were AuNRs, with a small content of cubes and/or spheres. However, with the supply of small amounts of AChE, a significant increase in the number of cubes was readily observed. Larger amounts of AChE promoted a drastic increase in the number of spheres and eventually the growth of rods was completely hindered. These changes can also be detected in the absorbance spectra of the growth products (Figure 2.3C). The spectrum corresponding to the original AuNR solution displays an intense band centered at 909 nm, which can be exclusively associated to the characteristic longitudinal LSPR of the AuNRs, and a weaker band centered at 509, mainly due to the transverse LSPR of the nanorods. Upon addition of AChE these two bands gradually blue shifted, while the ratio between the intensities of the longitudinal and transverse LSPR bands decreased. In view of these results, we can correlate the amount of generated AChE with the changes observed either in the intensity or in the position of the LSPR bands. This correlation was found to be optimum for the ratio between the LSPR maxima, i.e. $A_L/A_T$ (Figure 2.3D).

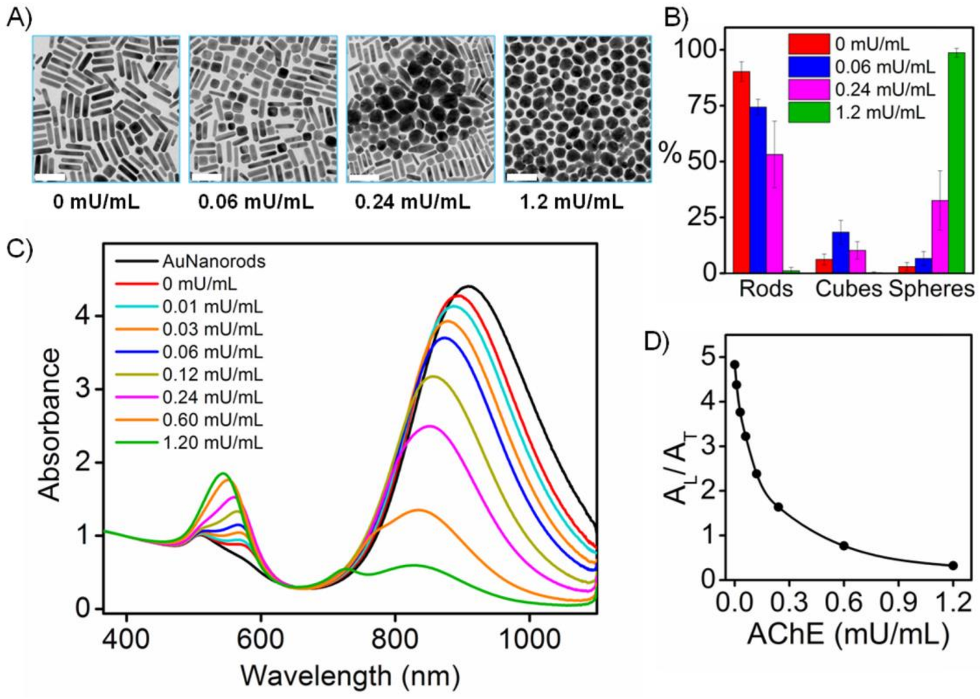

**Figure 2.3.-** Effect of TCh on seeded growth. A) TEM images of the growth products obtained upon addition of 0.05 mM ATCh and varying concentrations of AChE. B) Percentage of the different NP shapes in the growth product obtained for each AChE concentration. C) Absorbance spectra of the growth products formed in the presence of 0.05 mM ATCh and different concentrations of AChE. D) Variation of the ratio between the maxima of the longitudinal ($A_L$) and transverse ($A_T$) LSPR bands, as a function of AChE concentration. Scale bars in A represent 100 nm.

The same features were also observed when different amounts of ATCh were added to a 0.5 mU/mL AChE solution (Figure 2.4A). This observation, together with that provided by additional control experiments, reinforces the idea that the enzymatic activity is necessary for the modulation of AuNRs growth. Indeed, when only one of the two enzymatic components, either AChE or ATCh, was added to the enzymatic solution, no effect on AuNR growth was observed (see Figure 2.4B,C).

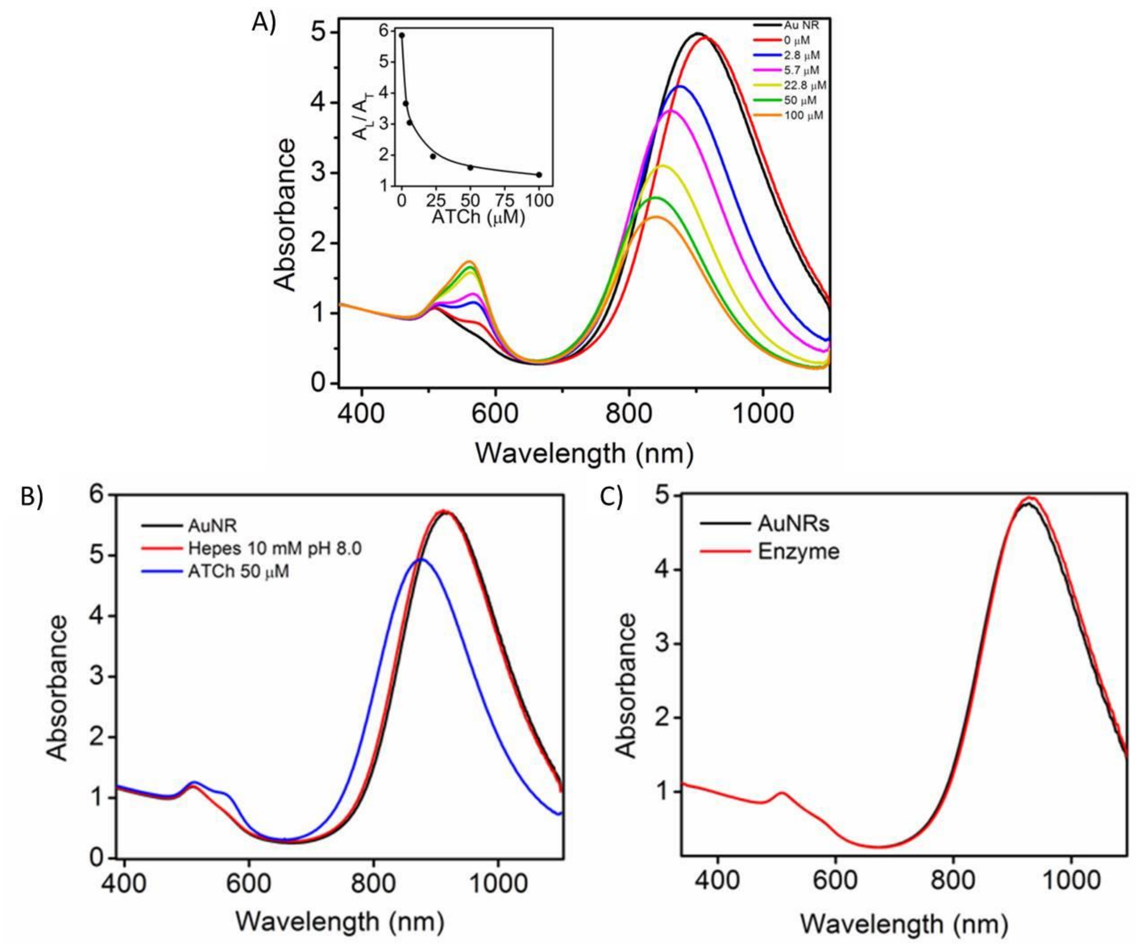

**Figure 2.4.-** A) Absorbance spectra of the growth products formed in the presence of 0.5 mU/mL AChE and different concentrations of ATCh. Inset: variation of the ratio between the maxima of the longitudinal ($A_L$) and the transverse ($A_T$) LSPR bands, as a function of ATCh concentration. B,C) Control experiments showing the effect of the individual components of the enzymatic reaction on the synthesis of AuNRs. Note that 50 µM ATCh has a slight effect on the AuNR synthesis. This can be due to the formation of TCh by the spontaneous hydrolysis of the precursor.

### 2.2.3.Overgrowth of Gold Nanorods

AuNRs can also be used as seeds for subsequent overgrowth and tuning of their dimensions. Therefore, it is also interesting to explore the effect of our thiolated molecule (TCh) on AuNR overgrowth. To this end, 2.5 mL of original AuNR sol ([Au] = 0.45 mM) was added to solutions containing increasing amounts of the enzyme AChE (and hence of TCh) and the resulting mixtures were added to the growth solution. TEM imaging (Figure 2.5A) revealed that thiols also impair AuNR overgrowth, since addition of small amounts of thiol obviously has an effect on the resulting AuNR shape. In fact, peanut- rather than rod-like morphology was obtained, while the average length was found to remain constant (Figure 2.5B). However, changes were observed in the width of the NRs, when comparing the ends, which seem to be equivalent to those for growth without thiol, with the middle section, which remains narrower (Figure 2.5B). For larger amounts of thiol, increased AuNR aggregation was observed (Figure 2.5A, right panel). These changes and in particular the aggregation process can be more clearly observed in the absorbance spectra (Figure 2.5D). The longitudinal plasmon band blueshifts at low concentrations of thiol, but redshifts at high concentrations, along with damping of the band. These observations are consistent with the formation of aggregates at high thiol concentrations (for AChE amounts larger than 3.7 mU/mL, which correspond to 0.08 mM of TCh). Interestingly, transverse overgrowth has been reported in the presence of other thiolated molecules[18]. In most cases, nanopeanuts were reported as an intermediate step of the overgrowth process, which then progress until achieving a truncated octahedral shape. It remains unclear why in our case the transverse overgrowth stops in the nanopeanut shape. It is important to mention that Stucky and coworkers[18] have shown successful overgrowth of the AuNRs to produce octahedral morphology only in the presence of molecules that can form zwitteronic ions (such as cysteine and glutathione). They have also shown that overgrowth in the presence of molecules that lack these specific functional groups lead to faster aggregation compared to overgrowth, which is in good agreement with our observations. The dumbbell-like shell can thus be interpreted as an intermediate stage of the initiated overgrowth process.

Since the tight CTAB bilayer on the lateral parts favors adsorption of thiol groups onto the tips[19], gold reduction starts preferentially on the 'corners' producing spheroids. Further increase of the concentration of thiol molecules can lead to replacement of the remaining CTAB on the lateral faces, but they are unable to stabilize the particles, leading to aggregation. In a more general context, we could in principle conclude that the thiol group of TCh adsorbs on the AuNR surface preventing seeded growth. Extrapolating this conclusion to the main reaction, we could speculate that the thiol selectively blocks the surface of the seeds, thereby inducing the formation of cubes and spheres.

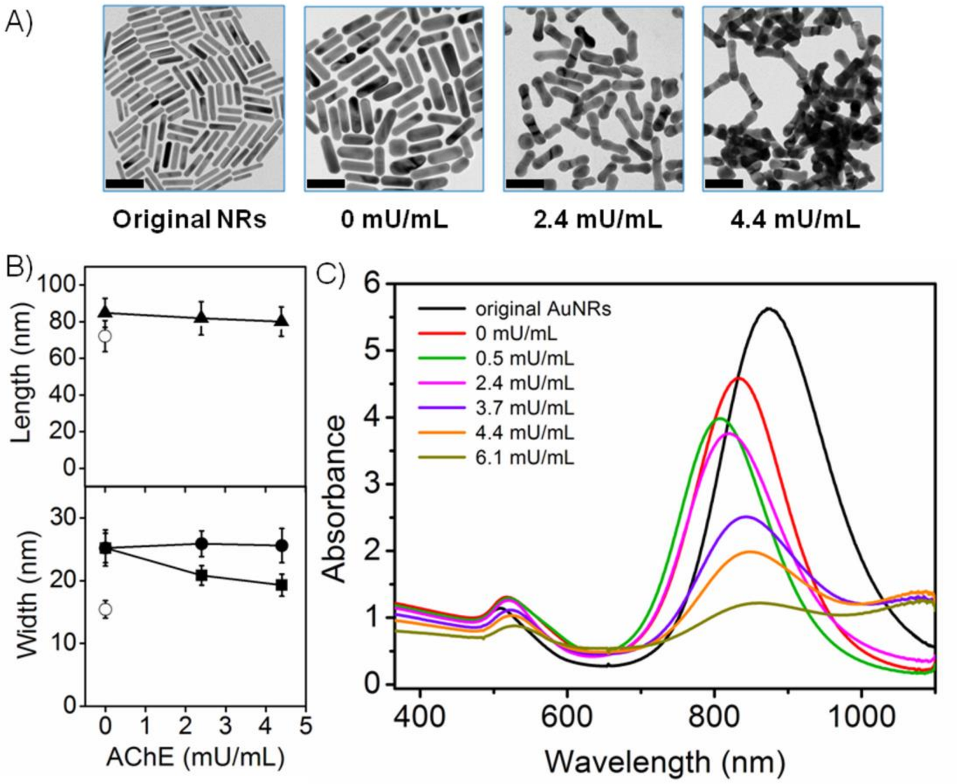

**Figure 2.5.-** Overgrowth of AuNRs. A) TEM images of the growth products obtained upon addition of 50 μM ATCh and varying concentrations of AChE to the growth solution. B) Plot of the length (triangles), width at the tips (circles) and width in the middle (squares) of the grown AuNRs, as a function of AChE concentration. Open circles show the length and width of the original AuNRs. C) Absorbance spectra of the growth products formed in the presence of 50 μM ATCh and different concentrations of AChE. Scale bars in A represent 100 nm.

### 2.2.4. Plasmon-Assisted Biosensing of AChE Inhibitors

In the previous section we have seen that very low concentrations of TCh (below 0.036 mM) can be directly correlated with the growth of AuNRs through the changes observed in their characteristic LSPR bands. Hence, we can take advantage of this feature to develop a colorimetric method for the detection of enzymatically produced TCh molecules. In fact, as the amount of TCh directly depends on the enzymatic activity of AChE and this in turn depends on the amount of AChE inhibitors present in the medium, the method can be developed for detecting traces of AChE inhibitors. This is extremely relevant in the context of chemical weapons, since such inhibitors have been used as nerve gases. We illustrate this possibility using as inhibitor diethyl 4-nitrophenyl phosphate (paraoxon), which is an organophosphate compound that inhibits AChE by phosphorylating the serine hydroxyl group in the active site of the enzyme (see Fig 2.6A) [20]. This toxicity mechanism is similar to that of organophosphorous nerve agents and therefore this compound can be used as an analogue for the study of nerve gases [21]. The colorimetric detection of AChE inhibitors has been previously reported using spherical AuNPs, generally based on thiol modulation through monitoring particle aggregation [22-24], but also through seed-mediated growth of Au-Ag nanoparticles [13]. For all these methods, nM detection was achieved for paraoxon, at best. We hypothesized that the use of anisotropic AuNRs may improve the detection limit since the high extinction coefficient characteristic of the longitudinal LSPR band (extremely sensitive to AuNR aspect ratio) may provide the analytic method with a higher sensitivity, which might be even increased by the presence of a second plasmon band at higher energies.

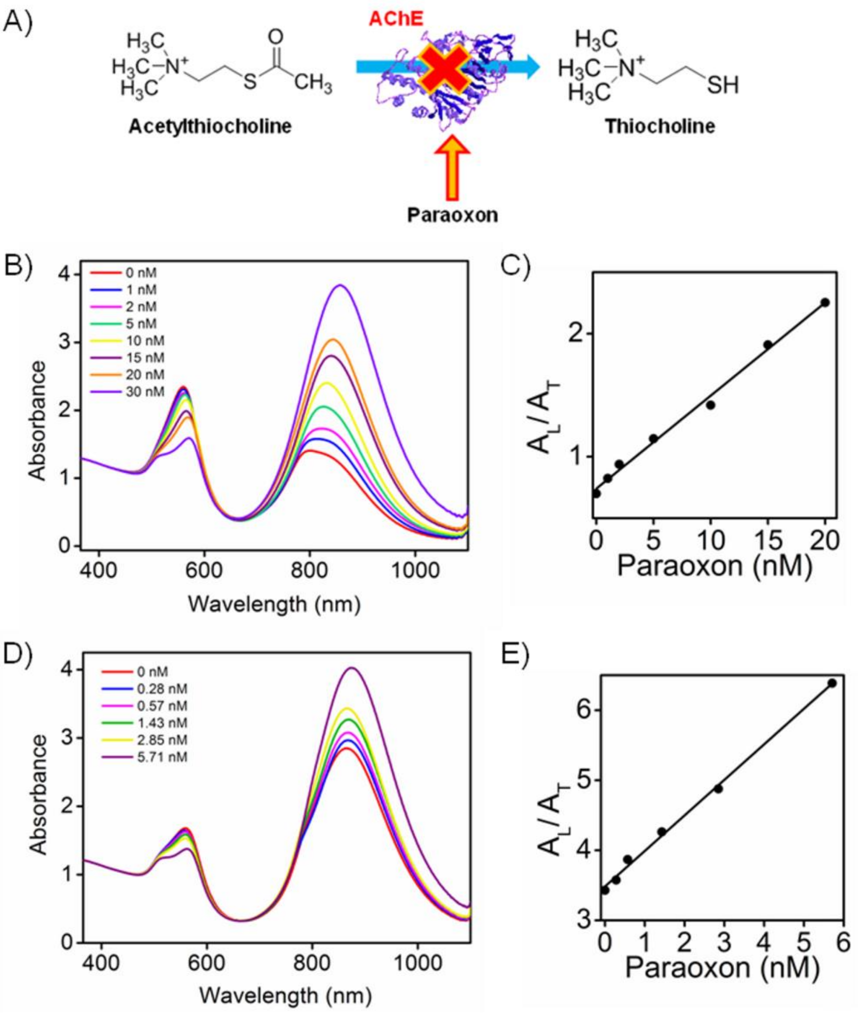

**Figure 2.6.-** A) Scheme showing the inhibition of AChE activity by paraoxon. B) Absorbance spectra of the growth products formed in the presence of 0.05 mM ATCh, 0.5 mU/mL AChE and different concentrations of paraoxon. D) Absorbance spectra of the growth products formed in the presence of 0.025 mM ATCh, 0.185 mU/mL AChE and different concentrations of paraoxon. C,E) Variation of the ratio between the maxima of the longitudinal ($A_L$) and transverse ($A_T$) LSPR bands, as a function of paraoxon concentration.

We first optimized the conditions for the detection of paraoxon in the nanomolar range, using the preincubation of 0.05 mU/mL AChE with paraoxon for 1 h, followed by the addition of 0.05 mM ATCh. The absorbance spectra corresponding to the inhibitors in a concentration range between 1 and 20 nM are reported in Figure 2.6B. By plotting the evolution of the ratio between the intensities of the two LSPR bands, a linear regression curve can be obtained, as shown in Figure 2.6C. This is a clear demonstration that the detection limit of 1 nM can be readily achieved. The accuracy in the determination of paraoxon concentration may be somehow improved by deconvoluting the higher energy (double) band into two Gaussians, in such a way that the one centered at higher energy can be associated to contributions by spheres and rods, while the one centered at lower energies accounts for the presence of cubes (see Figure 2.7A). This treatment results in an improvement of the linear regression curve, which increases its slope in 53%, thus improving the accuracy of the method (Figure 2.7B). Control experiments with higher paraoxon concentrations, in the absence of both AChE and ATCh were also carried out (see Figure 2.8). No differences in the synthesis of AuNRs were observed in this case upon paraoxon addition.

The reaction conditions were then adapted to test whether the limit of detection can be further improved. To this end, the preincubation time of AChE with paraoxon was increased from 1 to 3 hours and the concentrations of AChE and ATCh were reduced (see caption of Figure 2.6). As shown in Fig. 2.6D, E, these conditions allow us to achieve a detection limit of 280 pM. This limit of detection was obtained considering 3 standard deviations above the mean background. Deconvolution of the absorbance spectra was performed in the same way as that in the previous case, resulting in a significant improvement of the accuracy in determining paraoxon concentration. In fact, the slope of the linear regression curve increases in this case by 250% (Figure 2.7C).

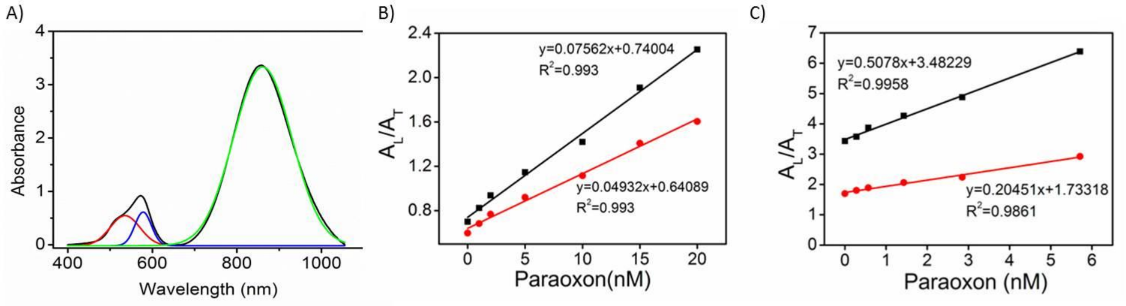

**Figure 2.7.-** A) Example of the deconvolution of the absorbance spectra for the biosensing of AChE inhibitors. The original spectrum (black) was deconvoluted into 3 Gaussian curves: two at high energies (blue and red) and one at low energies (green). B, C) Linear regression curves before (red) and after (black) the deconvolution of the spectra for the biosensing of AChE inhibitors. Regression curves are shown for nanomolar (B) and sub-nanomolar (C) detection of paraoxon.

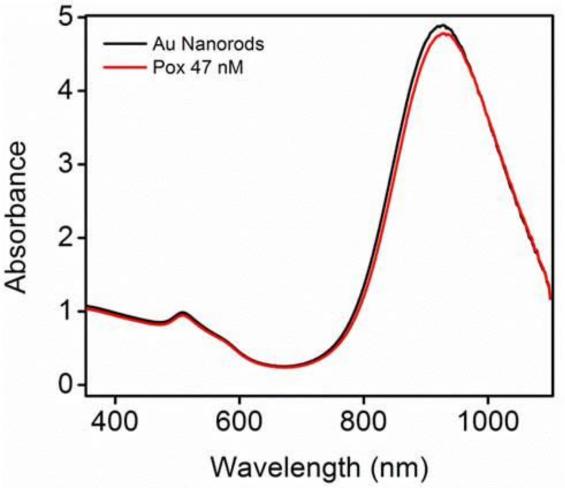

**Figure 2.8.-** Control experiment showing the negligible effect of paraoxon (47 nM) on the synthesis of AuNRs.

This choice provides the method with the highest sensitivity and accuracy for paraoxon biosensing with metal NPs reported so far. Finally, to confirm the robustness of this detection system, we evaluated the effect of galantamine and 1,5-bis(4-allyldimethylammoniumphenyl)pentan-3-one dibromide (BW284c51), two additional common AChE inhibitors. As expected, similar results to those reported for paraoxon were obtained (see Figure 2.9), thereby demonstrating the efficiency of this system for sensitive detection of any AChE inhibitor.

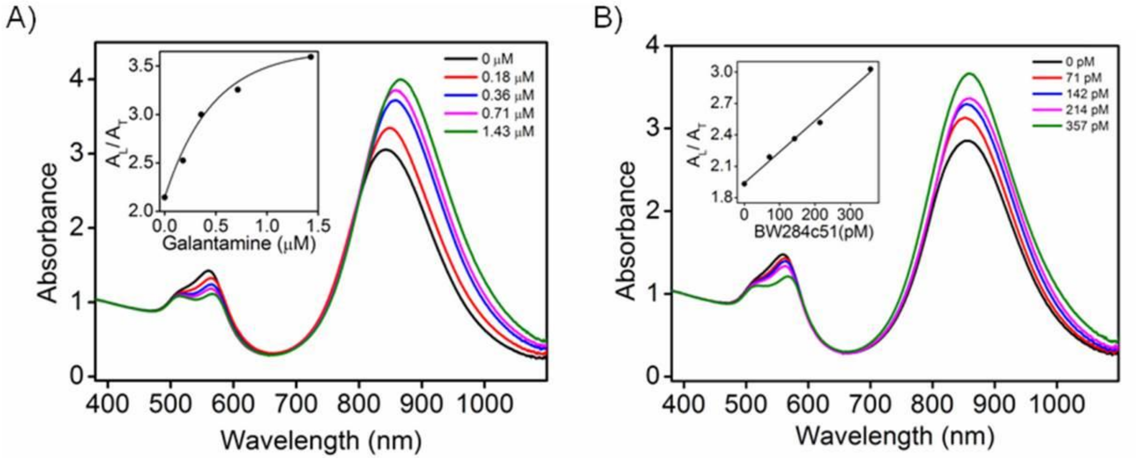

**Figure 2.9.-** Plasmon-assisted biosensing of AChE inhibitors. A) Absorbance spectra of the growth products formed in the presence of 0.05 mM ATCh, 0.25 mU/mL AChE and different concentrations of Galantamine. B) Absorbance spectra of the growth products formed in the presence of 0.05 mM ATCh, 0.37 mU/mL AChE and different concentrations of 1,5-bis(4-allyldimethylammoniumphenyl)pentan-3-one dibromide (BW284c51). In both cases the enzyme was preincubated at room temperature for 2 hours with different concentrations of the inhibitor. The enzymatic reaction for the formation of TCh was carried out at 37 °C for 15 min. Insets: variation of the ratio between the maxima of the longitudinal ($A_L$) and the transverse ($A_T$) LSPR bands, as a function of the concentration of Galantamine (A) or BW284c51 (B).

## 2.3. Conclusions

In this chapter we have demonstrated that trace concentrations of thiocholine – produced by the hydrolytic activity of the enzyme acetylcholinesterase – are able to modulate the seed-mediated growth of AuNRs. As a consequence, it was found that the intensities of the corresponding plasmon bands are highly sensitive to the concentration of this thiol-containing compound. Furthermore, a gradual change in the position and intensity of the longitudinal and transverse LSPR bands was observed upon addition of TCh prior to seeded growth. This was attributed to an evolution in the shape of the obtained AuNPs, from nanorods to cubes and spheres, as observed in TEM. On the basis of these findings we developed a simple colorimetric assay for the ultrasensitive detection of AChE inhibitors. Thus, subnanomolar concentrations of paraoxon and two other AChE inhibitors (nerve gas analogues) were detected. The lowest detection limit was 280 pM, which represents a significant improvement with respect to previous works for AChE inhibitors biosensing using metal nanoparticles.

## 2.4. Experimental Section

### 2.4.1. Materials

$HAuCl_4 \cdot 3H_2O$ (99%), cetyltrimethylammonium bromide (CTAB), sodium borohydride ($NaBH_4$), silver nitrate ($AgNO_3$), acetylcholinesterase (from electric eel), acetylthiocholine chloride, diethyl p-nitrophenyl phosphate (Paraoxon), Galantamine, 1,5-bis(4-allyldimethylammoniumphenyl)pentan-3-one dibromide (BW284c51), and other chemicals were supplied by Sigma-Aldrich. Milli-Q water (Millipore, Billerca, MA, USA) was used as solvent. All chemicals were used as received from the supplier, with no further purification.

### 2.4.2.Gold Nanorod Synthesis

AuNRs were prepared by seed mediated growth [4, 6]. The seeds were made by adding a freshly prepared $NaBH_4$ solution (0.3 mL, 0.01 M) to another solution containing $HAuCl_4$ (0.025 mL, 0.05 M) and CTAB (4.7 mL, 0.1 M). The growth solution was prepared by adding ascorbic acid (0.08 mL, 0.1 M) to a solution containing $HAuCl_4$ (0.1 mL, 0.05 M), $AgNO_3$ (0.12 mL, 0.01 M), HCl (0.19 mL, 1 M), and CTAB (10 mL, 0.1 M).

### 2.4.3. Acetylcholine Esterase Assay

Acetylthiocholine chloride (0.05 mM) was incubated with different amounts of AChE in 0.01 M HEPES buffer (pH 8.0) in a final volume of 70 μL, at 37 °C for 15 min. Then, 24 μL of gold seed solution was added and the resulting mixture was transferred to the AuNR growth medium.

### 2.4.4. Determination of Thiocholine Concentration

Quantification of thiocholine was performed by using the Ellman method [25]. After incubation of AChE and ATCh, the enzymatic product thiocholine reacts with the Ellman reagent (5-thio-2-nitrobenzoic acid) to form a colored compound that is measured spectrophotometrically at 412 nm. Thiocholine concentration was calculated through its molar extinction coefficient $\varepsilon = 14{,}150\ M^{-1}\ cm^{-1}$.

### 2.4.5. Gold Nanorod Overgrowth

Acetylthiocholine chloride (0.05 mM) was incubated with different amounts of AChE in 0.01 M HEPES buffer (pH 8.0) in a final volume of 350 μL, at 37 °C for 15 min. Then, 2.5 mL of AuNRs ([Au] = 0.45 mM) was added to this enzymatic solution. The resulting mixture was then transferred into the AuNR growth medium (7.5 mL).

### 2.4.6. Inhibition of AChE by Paraoxon

Two different assays were performed for the detection of paraoxon in the nanomolar and subnanomolar range:

*1st assay* (nanomolar detection): Different concentrations of paraoxon were incubated with 0.5 mU mL$^{-1}$ AChE in 0.01 M HEPES buffer (pH 8.0), in a final volume of 66.5 µL, at room temperature for 1 h. Next, 3.5 µL of 1 mM acetylthiocholine chloride in 0.01 M HEPES buffer (pH 8.0) was added, and the resulting mixture was incubated at 37 °C for 15 min. Thereafter, 24 µL of gold seeds was added to this solution and the mixture transferred into the AuNR growth medium.

*2nd assay* (subnanomolar detection): Different concentrations of paraoxon were incubated with 0.185 mU mL$^{-1}$ AChE in 0.01 M HEPES buffer (pH 8.0) in a final volume of 66.5 µL, at room temperature for 3h. Next, 3.5 µL of 0.5 mM acetylthiocholine chloride in 0.01 M HEPES buffer (pH 8.0) was added, and the resulting mixture was incubated at 37 °C for 30 min. Thereafter, 24 µL of gold seed solution was added and the mixture transferred into the AuNR growth medium.

## 2.5. References

[1] K. R. Brown, M. J. Natan, Langmuir, 14 (1998) 726.

[2] N. R. Jana, L. Gearheart, C. J. Murphy, Chem. Mater., 13 (2001) 2313.

[3] N. R. Jana, L. Gearheart, C. J. Murphy, Adv. Mater., 13 (2001) 1389.

[4] B. Nikoobakht, M. A. El-Sayed, Chem. Mater., 15 (2003) 1957.

[5] J. Perez-Juste, I. Pastoriza-Santos, L. M. Liz-Marzan, P. Mulvaney, Coord. Chem. Rev., 249 (2005) 1870.

[6] M. Liu, P. Guyot-Sionnest, J. Phys. Chem. B, 109 (2005) 22192.

[7] X. Ye, L. Jin, H. Caglayan, J. Chen, G. Xing, C. Zheng et al., ACS Nano, 6 (2012) 2804.

[8] X. Ye, C. Zheng, J. Chen, Y. Gao, C. B. Murray, Nano Lett., 13 (2013) 765.

[9] D. A. Zweifel, A. Wei, Chem. Mater., 17 (2005) 4256.

[10] Y. Horiguchi, K. Honda, Y. Kato, N. Nakashima, Y. Niidome, Langmuir, 24 (2008) 12026.

[11] K. Park, L. F. Drummy, R. C. Wadams, H. Koerner, D. Nepal, L. Fabris, R. A. Vaia, Chem. Mater., 25 (2013) 555.

[12] L. Vigderman, E. R. Zubarev, Chem. Mater., 25 (2013) 1450.

[13] A. Virel, L. Saa, V. Pavlov, Anal. Chem., 81 (2009) 268.

[14] M. G. Warner, J. E. Hutchison, Nat. Mater., 2 (2003) 272.

[15] G. H. Woehrle, M. G. Warner, J.E. Hutchison, Langmuir, 20 (2004) 5982.

[16] A. Y. Koyfman, G. Braun, S. Magonov, A. Chworos, N. O. Reich, L. Jaeger, J. Am. Chem. Soc., 127 (2005) 11886.

[17] J. Rodríguez-Fernández, J. Pérez-Juste, F. J. García de Abajo, L. M. Liz-Marzán, Langmuir, 22 (2006) 7007.

[18] X. Kou, S. Zhang, Z. Yang, C.-K. Tsung, G.D. Stucky, L. Sun et al., J. Am. Chem. Soc., 129 (2007) 6402.

[19] S. Gómez-Graña, F. Hubert, F. Testard, A. Guerrero-Martínez, I. Grillo, L. M. Liz-Marzán et al., Langmuir, 28 (2012) 1453.

[20] B. E. Mileson, J. E. Chambers, W. L. Chen, W. Dettbarn, M. Ehrich, A. T. Eldefrawi et al., Toxicol. Sci., 41 (1998) 8.

[21] A. Vale, S. Bradberry, P. Rice, T. C. Marrs, Medicine, 31 (2003) 26.

[22] J. Sun, L. Guo, Y. Bao, J. Xie, Biosens. Bioelect., 28 (2011) 152.

[23] M. Wang, X. Gu, G. Zhang, D. Zhang, D. Zhu, Langmuir, 25 (2009) 2504.

[24] G. Fu, W. Chen, X. Yue, X. Jiang, Talanta, 103 (2013) 110.

[25] G. L. Ellman, K. D. Courtney, V. Andres, Jr., R. M. Feather-Stone, Biochem. Pharmacol., 7 (1961) 88.

# 3. Enzymatic Etching of Gold Nanorods by Horseradish Peroxidase and Application to Blood Glucose Detection

*ABSTRACT*

*In this chapter another biocatalytic species, the enzyme horseradish peroxidase (HRP), has been used to trigger the chemical etching of AuNRs in a controlled way. This enzymatic reaction allowed us to induce a gradual decrease of the AuNR aspect ratio by adding trace concentrations of* $H_2O_2$ *and halide ions, which have also been found to be essential for this process. As a consequence, other enzymatic reactions, such as those catalyzed by glucose oxidase, were coupled to HRP activity, allowing the detection of different amounts of glucose. On the basis of these findings, we developed a highly sensitive and simple colorimetric assay that can be read out by the naked eye and allows the detection of physiological glucose concentrations in human serum.*

## 3.1. Introduction

This chapter deals with a different application of gold nanoparticles for the development of colorimetric sensors.[1-4] Gold nanorods (AuNRs) were selected again due to the sensitivity of their longitudinal localized surface plasmon resonance band toward minute changes in AuNR morphology,[5,6] so that the optical response can be tuned in a wide wavelength range by simply changing the aspect ratio. Shortening of gold nanorods,[7] transverse overgrowth[8] and lateral etching[9] are a few examples of reported post-synthetic morphological modifications of AuNRs.

One strategy for tuning the aspect ratio of AuNRs, and consequently their optical properties, is partial oxidation under mild conditions. For example, it has been shown that AuNRs etching by $H_2O_2$ takes place under acidic conditions.[10] However, high concentrations of oxidizing agent and high temperature are usually required, thereby preventing the applicability of this system for biodetection purposes. In order to overcome this issue, when lower $H_2O_2$ concentrations are used, catalytic species should be introduced to trigger the chemical etching of the AuNRs. Most of these species are metal ions such as ferric [9,11] or copper ions.[12] Still, the low specificity of these ions together with the relatively high concentrations of $H_2O_2$ represent an important limitation toward biodetection. Therefore, the introduction of biocatalytic species could significantly improve the efficiency and biocompatibility of the system, thereby opening new possibilities in biosensing using AuNRs.

One of these biological species is the enzyme horseradish peroxidase (HRP).[13] HRP is composed of a glycoprotein containing 308 amino acid residues and the active center hemin,[14] and can catalyze the oxidation of various electron donor substrates including 2,3-dimethoxyphenol, guaiacol, 5-amino-2,3-dihydro-1,4-phthalazinedione (luminol), 2,2′-azino-bis(3-ethylbenzothiazoline-6-sulfonate) (ABTS), and 3,3',5,5'-tetramethylbenzidine (TMB). The catalytic reaction is a three-step cyclic process. First, hemin complexed with the protein shell is oxidized by hydrogen peroxide forming a double covalent bond between iron in hemin and an oxygen atom from $H_2O_2$, to yield Compound I, which is a hemin derivative bearing an oxoferryl group ($Fe^{IV}=O$). This derivative can oxidize the first reducing substrate molecule through single-electron transfer, discharging the π-cation radical. The resulting intermediate still containing an oxoferryl group is called Compound II. A second substrate molecule reduces Compound II through a single-electron transfer to the native ferric hemin containing $Fe^{III}$. During this transformation, oxygen is released from an oxoferryl group when it accepts two protons forming a water molecule. During the reaction cycle of HRP two substrate molecules (AH) turn into two free radicals ($A^{\bullet}$) according to the following equations.[15]

$\text{Native HRP}+H_2O_2 \rightarrow \text{Compound I}^{\bullet +}$

$\text{Compound I}^{\bullet +}+AH \rightarrow \text{Compound II}^{+}+A^{\bullet}$

$\text{Compound II}^{+}+AH \rightarrow \text{Native HRP}+H_2O+A^{\bullet}$

HRP has been extensively used in biology and biotechnology for its unique characteristics, low cost and ability to form coupled enzyme assays.[15,16] We present in this paper the effect of HRP on the enzymatic anisotropic etching of AuNRs when trace concentrations of $H_2O_2$ are present (**Scheme 3.1**). Since HRP can be easily coupled to other enzymes, we coupled HRP to glucose oxidase (GOx), so that $H_2O_2$ can be generated via glucose oxidation, which may provide a novel method for glucose detection. In some recent works, the generation of $H_2O_2$ by GOx has been employed for the oxidation of metal nanoparticles, enabling the development of colorimetric glucose biosensors.[17,18] However, these experiments are usually time-consuming and costly. As a consequence, the introduction of HRP, an enzyme that presents very fast reaction kinetics and substrate turnover rates may be of interest for plasmonics assisted biosensing. Therefore, we developed in this work a simple and fast colorimetric assay for the detection of glucose, which can be directly read out by the naked eye.

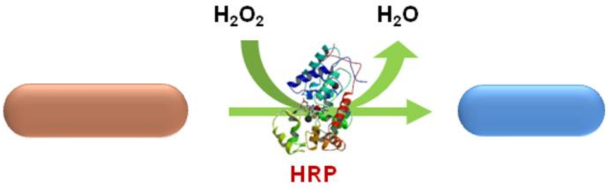

**Scheme 3.1**.- Enzymatic oxidation of gold nanorods by the enzymatic activity of horseradish peroxidase.

## 3.2. Results and Discussion

### 3.2.1. Enzymatic Etching of AuNRs by HRP

The effect of the enzymatic activity of HRP on the etching of AuNRs was first investigated in the presence of cetyltrimethylammonium bromide. Different concentrations of $H_2O_2$ were added to an AuNR solution $[Au^0]$=0.12 mM containing HRP (1.5 μM) and citrate buffer (20 mM, pH=4.0). As shown in Figure 3.1, in the presence of $H_2O_2$ and HRP, oxidation of the AuNRs occurs with the subsequent decrease in AuNR size (Figure 3.1A). Statistical analysis from transmission electron microscopy (TEM) images was used to analyze the length and thickness of the AuNRs before and after oxidation. Initially, the AuNRs were ca. 60 nm long and 15 nm thick. However, upon addition of $H_2O_2$ the NR length was gradually reduced while the thickness remained constant (Figure 3.1B). When a sufficient amount of $H_2O_2$ was added, the rod-like shape was lost and spherical particles were obtained. It is important to note at this point that oxidation was negligible in the absence of HRP, even at $H_2O_2$ concentrations as high as 100 μM. The TEM results, together with the observed changes in the LSPR band of the AuNRs after addition of different amounts of HRP confirm that the enzymatic activity of HRP is essential for the efficient etching of AuNRs under these conditions (see Figure 3.2). Although the precise mechanism underlying this process is beyond the aim of this study, we postulate that in the presence of $H_2O_2$, the HRP heme group may generate a hydroxyl radical with a stronger oxidizing ability than $H_2O_2$ itself, hence facilitating the above described oxidation reaction within a time scale of minutes. The observed anisotropic oxidation of the AuNRs is clearly reflected in a blue shift and a decrease in the intensity of the longitudinal LSPR band, initially centered at 850 nm, which gradually increases with the supply of $H_2O_2$. Therefore, the amount of $H_2O_2$ can be correlated to the observed longitudinal LSPR shift, for which a linear correlation was found in the $H_2O_2$ concentration range between 0 and 60 μM (Figure 3.1D). Such an etching process eventually leads to formation of spherical nanoparticles and even to complete dissolution.

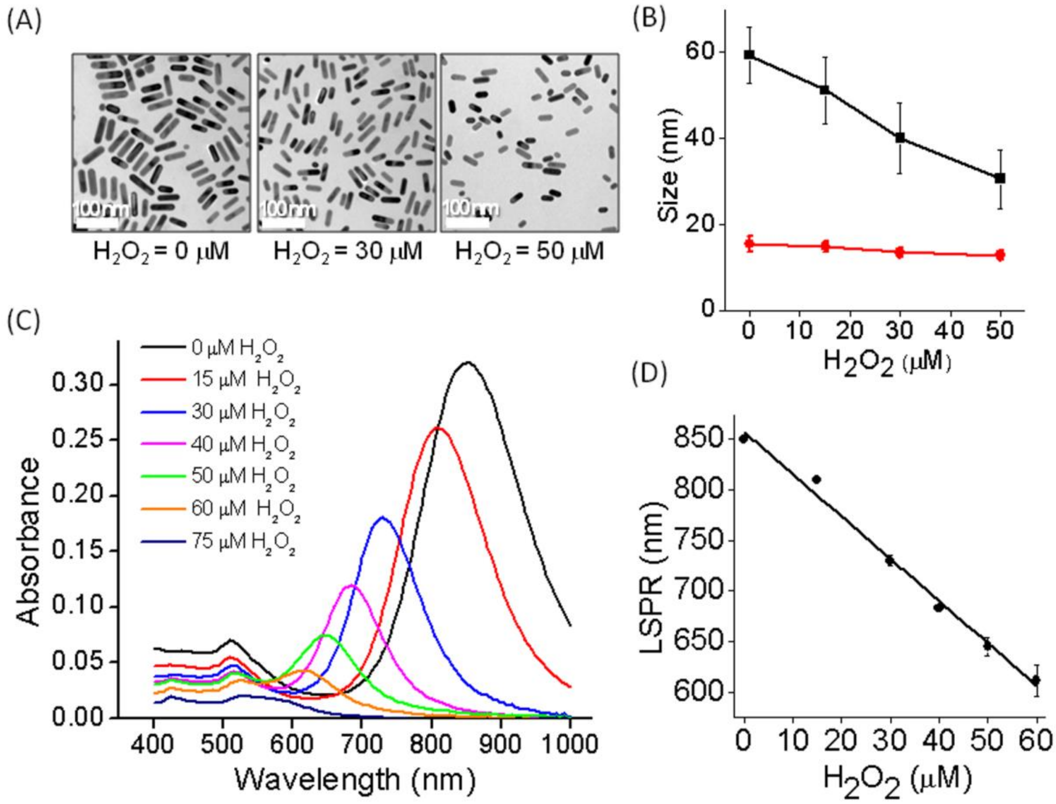

**Figure 3.1**.- Enzymatic etching of AuNRs by HRP (A) TEM images of the initial AuNRs and after addition of different $H_2O_2$ concentrations. (B) Length (black squares) and width (red circles) of the AuNRs as a function of $H_2O_2$ concentration. (C) Vis-NIR spectra after the incubation (15 min) of AuNRs with HRP (1.5 µM) and different concentrations of $H_2O_2$. (D) LSPR shift as a function of $H_2O_2$ concentration. Scale bars are the same for all images and represent 100 nm.

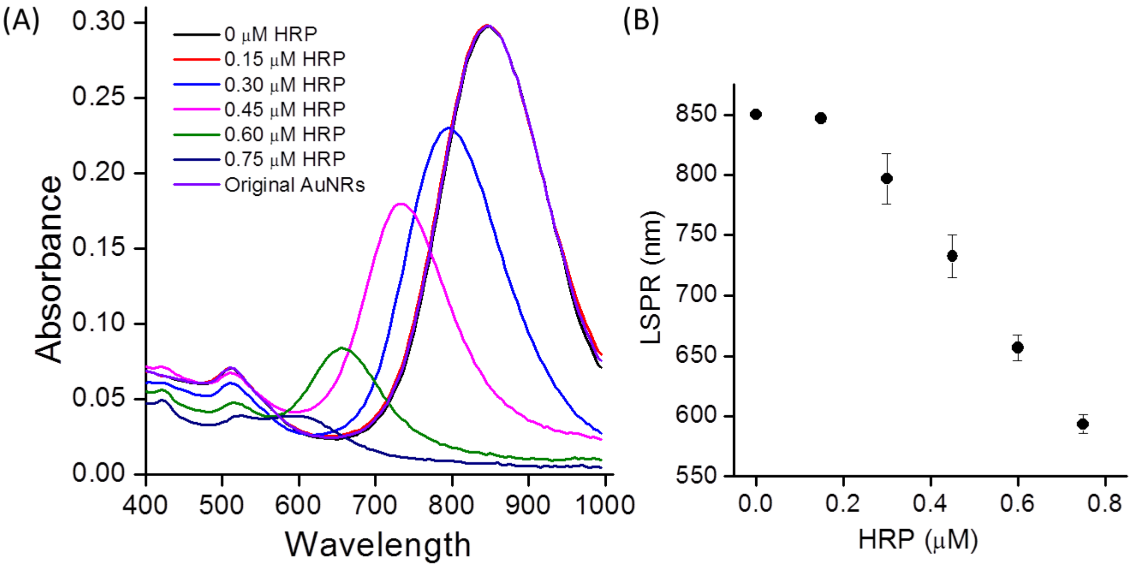

**Figure 3.2.-** Effect of HRP concentration on etching of AuNRs. (A) Absorbance spectra of AuNRs after incubation in the presence of $H_2O_2$ (0.1 mM) and different concentrations of HRP for 15 min. (B) Shift of the LSPR maximum as a function of HRP concentration.

### 3.2.2. Role of Halides on AuNRs Etching

For certain applications, purification of the AuNRs and removal of excess surfactant may be required. However, we found that when AuNRs were washed (twice) to remove excess CTAB, the oxidation reaction did not proceed. Since this was likely to be related to the removal of halide counterions, we tested the effect of adding bromide after purification. Thus, different concentrations of a bromide salt (NaBr) were added to the enzymatic solution to achieve a controlled concentration of anions. Indeed, the increase of [$Br^-$] was found to enhance AuNR etching. In other words, as more bromide was added to a solution containing $H_2O_2$ (176 µM) and HRP (1.5 µM), the length of the AuNRs decreased accordingly. Again, when no bromide was added the AuNRs were stable and no etching was observed. This result is in agreement with previous work in which addition of $HAuCl_4$ in the presence of CTAB led to rapid oxidation of AuNRs, although in this case the complexation of Au(III) ions with CTAB also played an important role.[19] Replacing bromide for other halides such as chloride and iodide was found to lead to different AuNR oxidation rates. Thus, in the presence of $Cl^-$ the oxidation is very slow and the longitudinal LSPR band does not shift upon addition of NaCl. In contrast, addition of NaI leads to efficient oxidation of the NRs, resulting in complete damping of the longitudinal band with iodide concentrations as low as 20 mM (Figure 3.3). The origin of such a difference arises from the redox potential of the various gold halides. In the three cases considered herein, $Cl^-$, $Br^-$, and $I^-$, the formation of the halide is favored. Oxidation of Au NRs by either $H_2O_2$ or hydroxyl radicals occurs spontaneously in all three cases. On the other hand, according to the reduction potential of the gold halides, the oxidation trend follows the order: $\mathrm{AuCl}_\mathrm{x}^- < AuB\mathrm{r}_\mathrm{x}^- < Au\mathrm{I}_\mathrm{x}^-$ , since the reduction potential for the Au halides follows the reverse order (see **Table 3.1**).

**Table 3.1.-** Redox potential for gold halides.

| | **$AuX_4^- + 2e^- \leftrightarrow AuX_2^- + 2X^-$** | **$AuX_2^- + e^- \leftrightarrow Au + 2X^-$** |
|---|---|---|
| Halide | **E (v)** | **E (v)** |
| $Cl^-$ | 0.926 | 1.154 |
| $Br^-$ | 0.802 | 0.959 |
| $I^-$ | 0.550 | 0.578 |

In conclusion, by forming a Au halide, the anions favor the oxidation of AuNRs. The extent of this oxidation depends upon the redox potential of the Au halides, as predicted thermodynamically and observed experimentally.

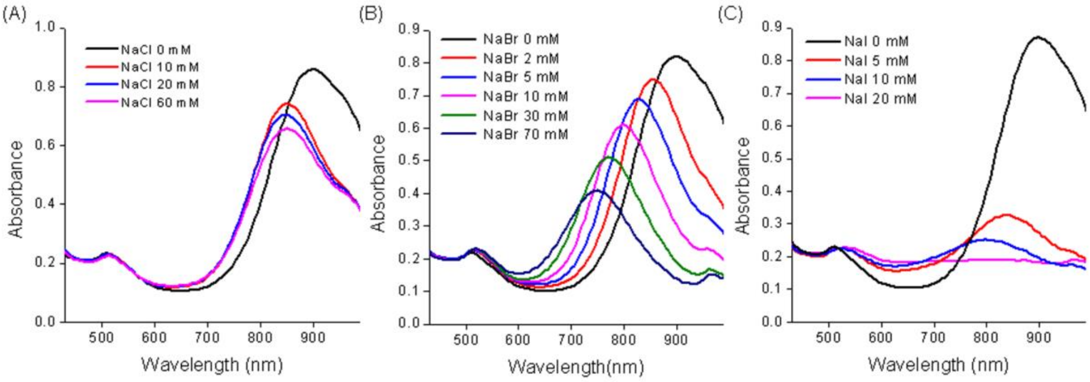

**Figure 3.3.-** Halide effect on the enzymatic etching of AuNRs. Absorption spectra of a AuNRs solution ([$Au^0$] = 0.29 mM) after incubation in the presence of HRP (1.5 μM), $H_2O_2$ (176 μM) and different concentrations of: (A) NaCl, (B) NaBr and (C) NaI. Note that in the case of NaCl the initial shift of the band (NaCl 10 mM) may be due to the presence of $Br^-$ ions in the solution. All spectra were normalized at 400nm.

In view of these findings we further investigated the oxidation of gold nanoparticles with different shapes and capping molecules. Spherical citrate gold nanoparticles (AuNS@citrate) and polyvinylpyrrolidone coated gold nanostars (AuNs@PVP) were enzymatically oxidized in the presence of 1 μM HRP, 25 mM NaBr and different concentrations of $H_2O_2$. As in the case of AuNRs, a decrease of the plasmon bands was observed, together with a blue shift in the case of AuNs@PVP (Figure 3.4). These results are consistent with the changes in the size and shape previously observed for AuNRs. Thus, in a more general context, we can conclude that the presence of halides in solution is required for the enzymatic oxidation of gold nanoparticles, regardless of the capping agent.

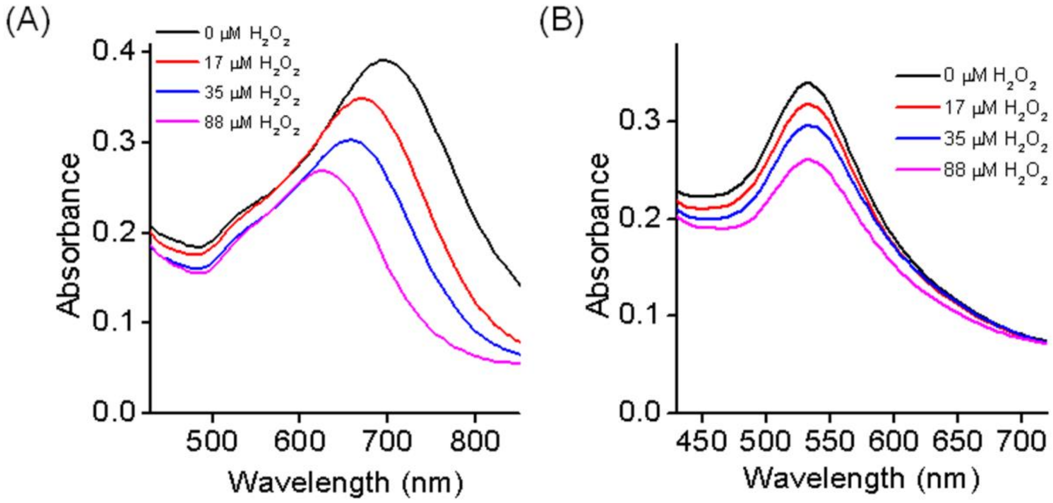

**Figure 3.4.-** Enzymatic oxidation of gold nanoparticles (A) Absorbance spectra of polyvinylpyrrolidone coated gold nanostars (AuNs@PVP; 0.26 mM), after incubation in the presence of HRP (1 µM), NaBr (25 mM) and different concentrations of $H_2O_2$ for 15 min (B) Absorbance spectra of spherical citrate gold nanoparticles (AuNS@citrate; 0.35 mM) after incubation in the presence of HRP (1 µM), NaBr (25 mM) and different concentrations of $H_2O_2$. Note that the rates of oxidation are different than in the case of AuNRs due to the use of a lower concentration of HRP in all cases.

### 3.2.3.Plasmon-Assisted Glucose Biosensing

We have seen in the previous section that HRP can oxidize gold nanoparticles in the presence of $H_2O_2$ and a halide acting as gold complexing agent. This feature can be exploited to develop a colorimetric method for the detection of glucose, by coupling the enzymatic activity of glucose oxidase (GOx) to HRP activity (Figure 3.5A). We postulated that AuNRs etching would serve as a reporter for any enzymatic reaction coupled to the HRP reaction. However, we found that this assessment is only true when the pH of the reaction medium is acidic (data not shown). Therefore, GOx was selected for this purpose since this enzyme has been shown to remain active under acidic pH conditions (The present study was performed in citrate buffer, pH=4.0). GOx catalyzes the oxidation of glucose, generating $H_2O_2$ as a reaction product. The addition of aqueous solutions with different glucose concentrations to a solution containing HRP, GOx and AuNRs leads to a gradual blue shift of the longitudinal LSPR, which can be easily monitored by Vis-NIR spectroscopy (Figure 3.5B). A linear correlation between the amount of glucose added to the solution and the shift of the AuNRs longitudinal band was clearly observed in the concentration range from 0 to 250 μM. This provides a highly sensitive method for the detection of glucose (with a detection limit of 10 μM). This limit of detection was obtained considering 3 standard deviations above the mean background (Figure 3.5C). Control experiments demonstrate that no oxidation takes place in the absence of HRP (Figure 3.6A).

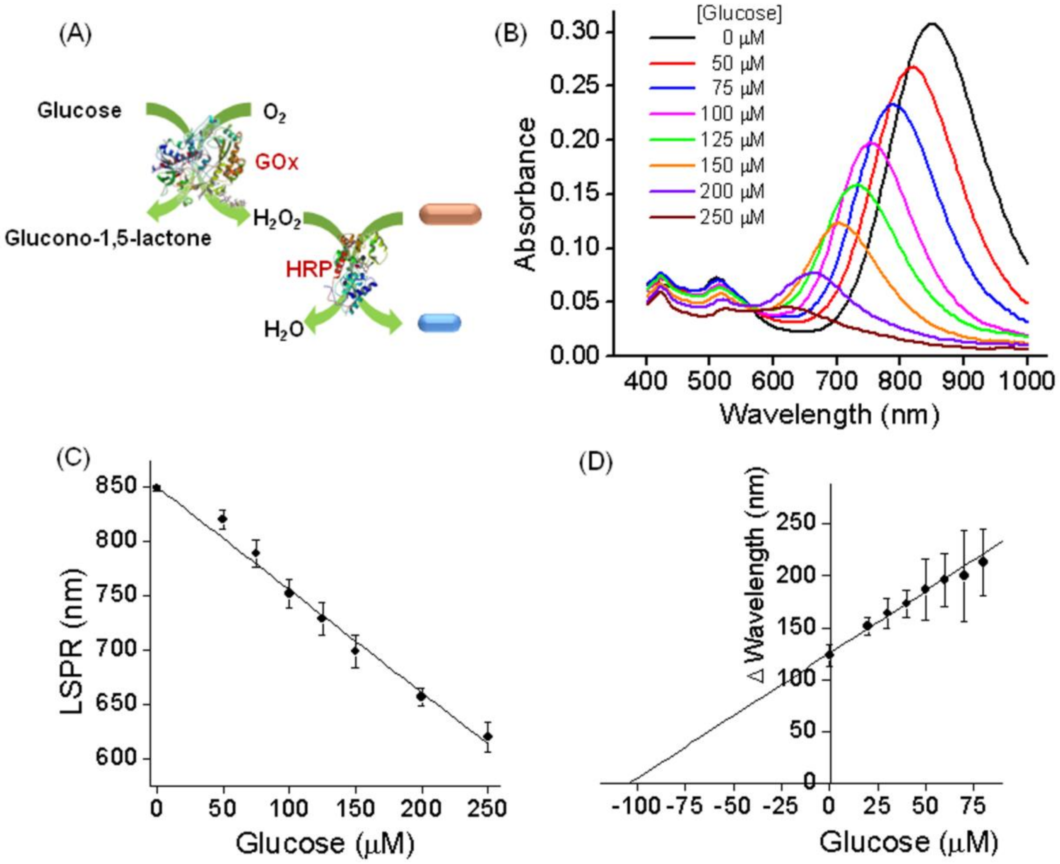

**Figure 3.5.-** Enzymatic etching of AuNRs for glucose biosensing. (A) Schematic view of the enzymatic etching of AuNRs by coupled activity of GOx and HRP. (B) Vis-NIR spectra of AuNRs solution before and after incubation in the presence of HRP (1.5 μM), GOx (50 nM) and different concentrations of glucose as indicated. (C) LSPR shift as a function of glucose concentration. (D) Quantification of glucose concentration in human serum via the method of standard addition.

Upon optimization of this enzymatic coupled activity, human serum of unknown glucose concentration was analyzed to demonstrate the practical application of this plasmon-assisted biosensor. Note that the usual concentration of glucose in human blood lies within the mM range, while the high sensitivity of this method allows us to carry out detection in the μM range. Hence, human serum samples were diluted 50-fold prior to the analysis. The concentration of glucose in the human samples was quantified by the method of the standard addition. Human serum was added to standard solutions containing different concentrations of glucose from 0 to 80 μM. The experimental data were plotted as concentration of added glucose vs. LSPR shift. As shown in Figure 3.5D, a linear regression was performed to calculate the position of the X-intercept of the calibration line, which showed the concentration of glucose in the diluted real sample. Taking the dilution factor into consideration, a glucose concentration in the human plasma of 5.31 mM was determined. This concentration is within the physiological range, thus demonstrating that this method is valid for the detection of glucose in human blood. Note that a standard colorimetric procedure yielded a value of 5.11 mM for the same human serum sample (data not shown). A similar plasmonic glucose biosensor has been reported by Liu *et al.*,[18] based on AuNRs etching mediated by the Fenton reagent $Fe^{2+}$-EDTA. The advantage of using HRP instead of the Fenton reagent for this particular application is that AuNR oxidation is much faster and sensitive (see a comparison in Figure 3.6B. In the work reported in ref. [18], comparatively high concentrations of $H_2O_2$ were required to oxidize the AuNRs, even in presence of CTAB.

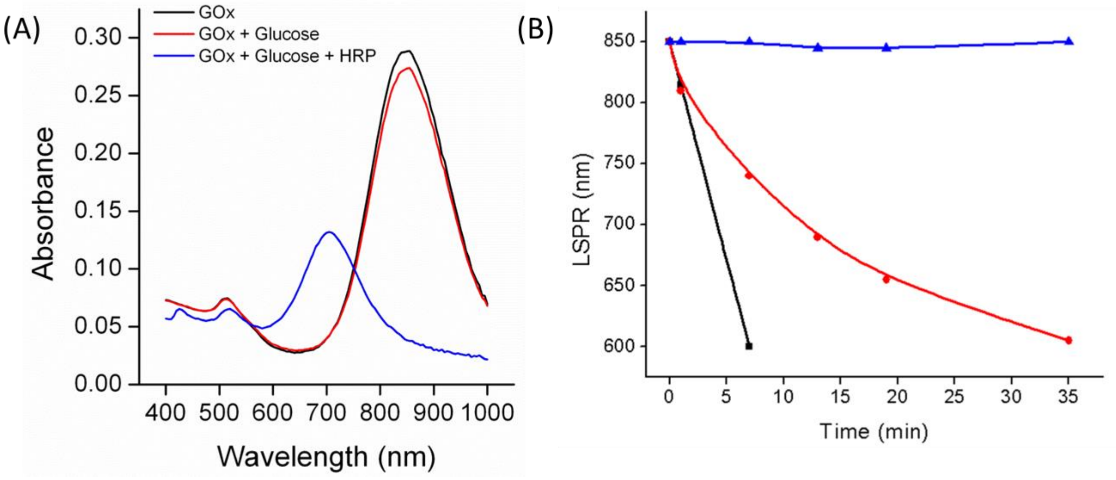

**Figure 3.6.-** (A) Control experiments showing the importance of HRP in the etching of AuNRs. AuNRs were incubated with GOx (50 nM) and Glucose (0.1 mM) in the presence (blue line) or absence (red line ) of HRP (1.5 µM), or only in the presence of GOx (50 nM) (black line) for 20 min. (B) Variation of LSPR maxima with time during the oxidation etching of AuNRs by HRP 1.5 µM and $H_2O_2$ 0.1 mM (black squares), Fenton reagent 0.25 mM and $H_2O_2$ 0.1 mM (red circles), and only $H_2O_2$ 0.1 mM (blue triangles).

Practical application of this colorimetric biosensing method may require that non-trained users can easily perform the sensing assay. For this purpose, we carried out a simplified implementation of the sensor, based on silica gels prepared by a simple sol-gel preparation,[20] in which AuNRs were embedded in the presence of HRP 3.2 µM, GOx 140 nM and NaBr 25 mM. Addition of a glucose solution on the so formed composite silica monolith leads to a color change from pink to yellow, reflecting the oxidation of the AuNRs (Figure 3.7). It is important to note that the thickness of the silica gel is of relevance for this process. The slow diffusion of the glucose solution through the gel triggers the observation of a range of colors with time, from yellow through pink, depending on the oxidation stage of the AuNRs (Figure 3.7A). The color of the AuNRs in the gel, prior to glucose addition, is light pink whereas in the presence of glucose AuNRs etching leads to a color change into blue, and eventually into yellow due to complete oxidation from

$Au^0$ into $Au^{III}$. The reaction conditions and the thickness of the gel were thus optimized to develop a simple device for the detection of glucose with the naked eye. As displayed in Figure 3.7B, addition of a 5 mM glucose solution was sufficient to change the color from pink to yellow. This concentration is close to the usual glucose level in human blood (*ca*. 5.5 mM).

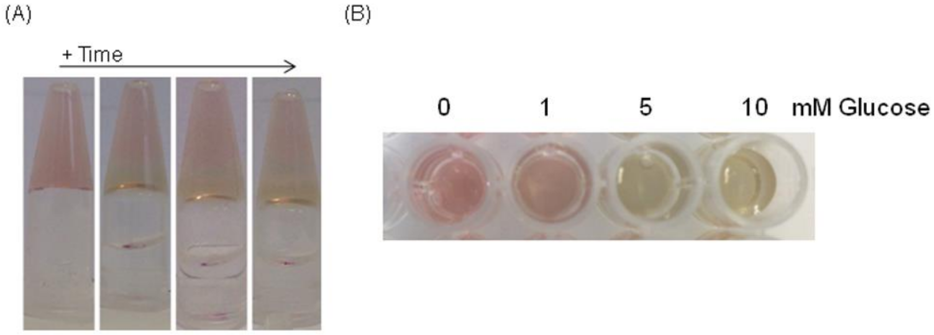

**Figure 3.7.-** Glucose detection in silica gel/enzyme/AuNR composites. (A) Kinetics of AuNR oxidation in a silica gel within an eppendorf tube. Note that the increase of the AuNR oxidation with time leads to an increase of the yellow band. (B) Colorimetric detection of glucose in thin silica gels loaded on well plates with a more uniform color change.

## 3.3. Conclusions

In this chapter we have demonstrated that the enzymatic activity of horseradish peroxidase can induce the gradual oxidation of AuNRs and other gold nanoparticles, in the presence of halide ions as gold complexing agents. As a consequence of AuNR shortening, the position of the longitudinal LSPR band of the AuNRs can be used to determine the concentration of $H_2O_2$ in solution. On the basis of this process, we developed a simple colorimetric assay for the detection of glucose that allows detection of physiological glucose concentrations. The use of

HRP in this reaction represents a significant improvement with respect to previously reported plasmon-assisted glucose biosensors.

## 3.4. Experimental Section

### 3.4.1. Materials

$HAuCl_4 \cdot 3H_2O$ (99%), cetyltrimethylammonium bromide (CTAB), sodium borohydride ($NaBH_4$), silver nitrate ($AgNO_3$), glucose oxidase type VII from *aspergillus niger*, horseradish peroxidase type VI and other chemicals were supplied by Sigma-Aldrich. Milli-Q water (Millipore, Billerca, MA, USA) was used as solvent. All chemicals were used as received from the supplier. Absorbance measurements were performed in a Varioskan Flash microplate reader (Thermo Scientific) using 96-microwell plates. The UV-Vis absorbance spectra were scanned from 400 to 1000 nm at 30 °C.

### 3.4.2. Gold Nanorod Synthesis

AuNRs were prepared by seed mediated growth [6,21]. The seeds were made by adding a freshly prepared $NaBH_4$ solution (0.3 mL, 0.01 M) to another solution containing $HAuCl_4$ (0.025 mL, 0.05 M) and CTAB (4.7 mL, 0.1 M). The growth solution was prepared by adding ascorbic acid (0.08 mL, 0.1 M) to a solution containing $HAuCl_4$ (0.1 mL, 0.05 M), $AgNO_3$ (0.12 mL, 0.01 M), HCl (0.19 mL, 1 M), and CTAB (10 mL, 0.1 M).

### 3.4.3. HRP Assay

Varying concentrations of $H_2O_2$ were added to a solution containing AuNRs ($[Au^0]$=0.12 mM), CTAB 5 mM, HRP (1.5 μM) and citrate buffer 20 mM pH 4.0, in a final volume of 100 µL. The absorbance spectra of the resulting mixtures were recorded after 15 min.

### 3.4.4. GOx Assay

Varying concentrations of glucose were added to a solution containing AuNRs ($[Au^0]$=0.12 mM), CTAB 5 mM, HRP (1.5 µM), GOx (50 nM) and citrate buffer 20 mM, pH 4.0, in a final volume of 100 µL. The absorbance spectra of the resulting mixtures were recorded after 15 min.

### 3.4.5. Effect of Halides

In order to remove excess CTAB, AuNRs were washed by centrifugation at 7000 rpm for 20 min. The supernatant was discarded and the precipitate was redispersed in water until reaching the initial volume. The washed AuNRs were used in the HRP assay as described above.

### 3.4.6. Quantification of Glucose in Human Serum

Commercial human serum (Sigma-Aldrich) was centrifuged on Amicon Ultra filter with a 3,000 molecular weight cutoff. After filtering, serum was spiked with different concentrations of glucose and the glucose concentration of the mixtures was determined as described above. The dilution factor of serum in the assay was 1:50.

### 3.4.7. Preparation of Silica Gel/Enzyme/AuNR Composites

Sol-gel based silica matrices were prepared according to Luckham and Brennan.[20] Briefly, 10 mL of H2O were mixed with 2.9 g of sodium silicate solution followed by addition of 5 g of Dowex cation exchange resin to replace $Na^+$ with $H^+$. The mixture was stirred until reaching a final pH = 4 and filtrated to remove the resin. This silicate precursor was then mixed in a 1:1 ratio with a solution containing AuNRs 0.78 mM, HRP 3.4 µM, GOx, 0.28 µM, NaBr 50 mM in citrate buffer 0.2 M pH 4.0. The mixtures were then allowed to cure in microplate wells for 48 h at 4 °C prior to use. Samples of 100 µL containing different concentrations of glucose were added to the silica gel matrix, and the change in the color of the silica gels was followed by the naked eye.

## 3.5. References

[1] K. L. Kelly, E. Coronado, L. L. Zhao and G. C. Schatz, J. Phys. Chem. B, 107 (2002) 668.

[2] L. Rodriguez-Lorenzo, R. de la Rica, R. A. Alvarez-Puebla, L. M. Liz-Marzan and M. M. Stevens, Nat. Mater. 11 (2012) 604.

[3] L. Guo, Y. Xu, A. R. Ferhan, G. Chen and D.-H. Kim, J. Am. Chem. Soc. 135 (2013) 12338.

[4] Y. Xianyu, J. Sun, Y. Li, Y. Tian, Z. Wang and X. Jiang, Nanoscale, 5 (2013) 6303.

[5] M. Coronado-Puchau, L. Saa, M. Grzelczak, V. Pavlov and L. M. Liz-Marzan, Nano Today, 8 (2013) 461.

[6] J. Perez-Juste, I. Pastoriza-Santos, L. M. Liz-Marzan and P. Mulvaney, Coord. Chem. Rev. 249 (2005) 1870.

[7] C.-K. Tsung, X. Kou, Q. Shi, J. Zhang, M. H. Yeung, J. Wang and G. D. Stucky, J. Am. Chem. Soc. 128 (2006) 5352.

[8] X. Kou, S. Zhang, Z. Yang, C.-K. Tsung, G. D. Stucky, L. Sun, J. Wang and C. Yan, J. Am. Chem. Soc. 129, (2007) 6402.

[9] X. Guo, Q. Zhang, Y. Sun, Q. Zhao and J. Yang, ACS Nano, 6 (2012) 1165.

[10] G. Chandrasekar, K. Mougin, H. Haidara, L. Vidal and E. Gnecco, Appl. Surf. Sci. 257 (2011) 4175.

[11] R. Zou, X. Guo, J. Yang, D. Li, F. Peng, L. Zhang, H. Wang and H. Yu, CrystEngComm, 11 (2009) 2797.

[12] T. S. Sreeprasad, A. K. Samal and T. Pradeep, Langmuir, 23 (2007) 9463.

[13] J. Everse, K. E. Everse and M. B. Grisham, Peroxidases in Chemistry and Biology, Volume II, CRC Press, 1990.

[14] K. G. Welinder, FEBS Lett. 72 (1976) 19.

[15] A. M. Azevedo, V. C. Martins, D. M. Prazeres, V. Vojinovic, J. M. Cabral and L. P. Fonseca, Biotechnol. Annu. Rev. 9 (2003) 199.

[16] N. C. Veitch, Phytochemistry, 65 (2004) 249.

[17] Y. Xia, J. Ye, K. Tan, J. Wang and G. Yang, Anal. Chem. 85 (2013) 6241.

[18] X. Liu, S. Zhang, P. Tan, J. Zhou, Y. Huang, Z. Nie and S. Yao, Chem. Commun., , 49 (2013) 1856.

[19] J. Rodriguez-Fernandez, J. Perez-Juste, P. Mulvaney and L. M. Liz-Marzan, J. Phys. Chem. B, 109 (2005) 14257.

[20] R. E. Luckham and J. D. Brennan, Analyst, 135 (2010) 2028.

[21] B. Nikoobakht and M. A. El-Sayed, Chem. Mater. 15 (2003) 1957.

# 4. Gold Nanotriangles for Surface Enhanced Raman Scattering Detection

*ABSTRACT*

*In this chapter we have significantly improved the surface-enhanced Raman scattering detection of various molecules by using gold nanotriangles. This nanostructure display fascinating nanoplasmonic features that have been hindered by the lack of efficient synthetic methods yielding sufficient size and shape monodispersity, as well as by insufficient morphological stability. Here we present a synthesis and purification protocol that efficiently addresses these issues. The obtained monodispersity leads to extended self-assembly, not only on electron microscopy grids but also at the air–liquid interface, allowing transfer onto centimeter-size substrates. These extended monolayers show promising performance as surface-enhanced Raman scattering substrates, as demonstrated for thiophenol detection.*

## 4.1. Introduction

Gold nanotriangles are anisotropic metal nanoparticles, which stand out for their unique optical and plasmonic properties with potential application in various fields.[1-4] However, the quality of available AuNTs is still far away from that usually found for other anisotropic nanoparticles, such as gold nanorods. The yield of common synthetic methods for AuNTs is usually below 30-40% and the particles often show high polydispersity. Indeed, in the existing synthetic protocols the NTs usually have relatively big lateral dimensions,[5,6] and no synthetic protocols for the preparation of monodisperse AuNTs below 100 nm are available in the literature. Moreover, the stability of these NPs against oxidation is low and reshaping typically takes place few hours after their preparation.[7] All these factors have seriously hindered the application of AuNTs for the development of plasmonic devices. Since it is not always possible to synthesize highly monodisperse AuNPs in one step, in this work we employed purification strategies to obtain high quality NP colloids. We demonstrate here that variations on existing synthetic processes [8,9] can yield to AuNTs with initial shape-yield higher than 50%, which can be further increased up to 95% after a simple and fast purification step. This method additionally yields optimum monodispersity of the AuNTs down to 4%, and a wide tunability of the NT dimensions with edge lengths ranging from 50 to 150 nm, which translates into LSPR values from 630 to 740 nm. This high uniformity allowed us to assemble monodisperse AuNTs on substrates and to evaluate their performance for sensing applications. In this respect, we aim at the formation of close-packed AuNT monolayers for their use as surface enhanced

Raman scattering (SERS) substrates. SERS ultradetection usually requires the formation of hot spots, *i.e.* short separation distances between the plasmonic nanoparticles.[10] This requirement can be contented by the self-assembly of nanoparticles, which can be improved at the air/liquid interface, into large monolayers of closely packed nanoparticles.[11,12] Since AuNTs are stable in aqueous solution, surface activity can be obtained through functionalization with polyvinylpyrrolidone (PVP).[13,14] PVP coating of plasmonic nanoparticles allows the formation of single nanoparticle monolayers at the air/liquid interface extended over large areas reaching square centimeters, as has been previously shown for silver nanocubes[15] and nanotriangles.[16] We therefore used PVP-coating and subsequent self-assembly to fabricate SERS substrates based on AuNTs. The SERS performance of AuNTs both in solution and in assemblies is demonstrated through benzenethiol (BT) detection, reaching enhancement factors around $10^5$, even for well-separated AuNTs in solution.

## 4.2. Results and Discussion

### 4.2.1. Synthesis of AuNTs

The synthesis of AuNTs is based on the seed mediated growth originally proposed by Mirkin and coworkers.[17] In this method, the presence of iodide anions in a silver-free growth solution triggers the anisotropic growth of CTAC coated seeds. The initial Au seeds with a size of ca. 7 nm are first overgrown up to 40 nm in an intermediate growth step, and subsequently transferred to the final growth solution, yielding an overall shape-yield around 30%, with rather high polydispersity. The synthetic scheme (**Scheme 4.1** Experimental Section) comprises two growth steps and allows one to obtain AuNTs (edge length 71±3 nm) characterized by a low polydispersity (below 6%) and high morphological stability over time.

### 4.2.2. Nanotriangles Purification

The presence of by-product particles with different morphologies remaining after the synthesis may hinder the direct use of these NTs for applications that require very high particle monodispersity and narrow plasmon resonances, such as SERS detection. In order to obtain a pure AuNT dispersion, purification by flocculation and subsequent precipitation was performed. Such a separation by shape was achieved by exploiting the depletion interactions between particles in the presence of surfactant micelles. This kind of interactions arise when two particles are separated by a distance that results to be smaller than the size of a more abundant second component,[18-20] which, in our case, is represented by CTAC micelles. This approach presents two crucial benefits: 1) the stability of the AuNTs is not compromised at high CTAC concentrations (indeed, CTAC can even enhance the stability of AuNTs), and 2) centrifugation is not necessary due to the nature of the CTAC stock solution (see Experimental Section). The optimal procedure was found to correspond to a CTAC concentration of 0.15 M. The separation of the by-product (mainly isotropic particles) can be monitored by changes in the LSPR band: the band centered at 520-530 nm (typical of isotropic particles) significantly decreases, as well as by TEM (See Figure 4.1).

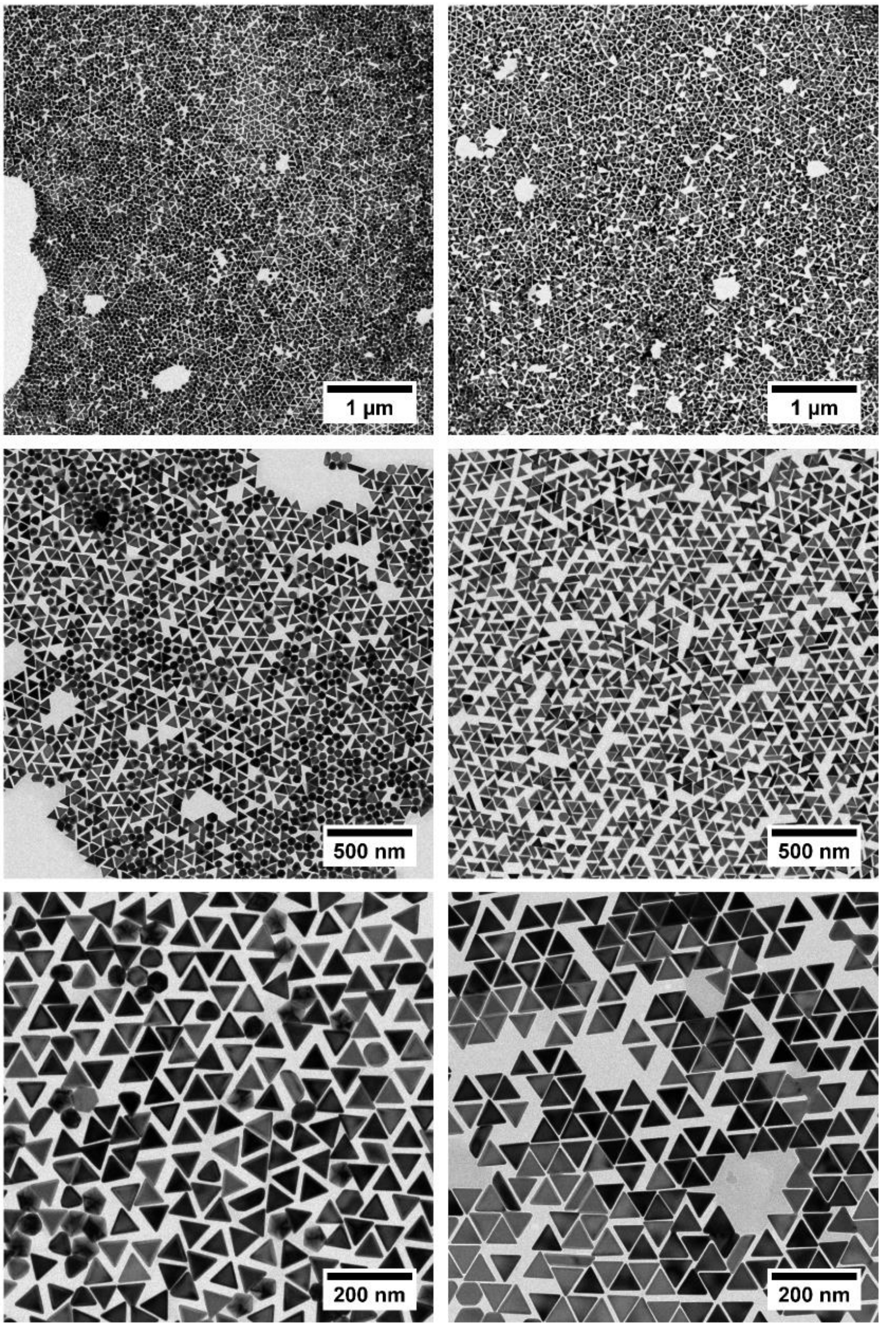

**Figure 4.1.-** Comparison between non-purified and purified AuNT samples (TEM images at various magnifications). Left panel: non-purified sample; right panel: purified sample.

### 4.2.3. Self-Assembly of AuNTs

AuNTs@PVP (see Experimental Section) were transferred (by centrifugation and redispersion) into an ethanol:hexane mixture with a volume ratio of 2:3 and subsequently spread on top of an air/water interface. PVP provides surface activity to the AuNTs, resulting in the stabilization of a monolayer of AuNTs at the air/liquid interface, covering an area of several square centimeters. The amount of AuNTs to be spread was estimated from the NT concentration in solution to obtain a single monolayer at the air-water interface. The monolayer appears as a thin gold layer to the naked eye (Figure 4.2A) and can be readily transferred onto any solid substrate by gently touching the monolayer with the substrate parallel to the air/liquid interface. This assembly method requires a low amount of sample, given that the whole amount of AuNTs spread at the air/liquid interface will enter the monolayer. The possibility of fabricating homogeneous substrates over large areas is most relevant, especially when comparing with methods such as drop casting. Drop casting allows the fabrication of crystallites limited to the micrometer range,[21] while achieving only local order due to coffee ring effects.[22]

AuNT monolayers were transferred onto carbon-coated copper grids for TEM analysis. The NTs within the monolayer showed a high degree of local disorder, however, they were positioned within short distances from each other (Figure 4.2B-C). ImageJ software was used to calculate the coverage density, which resulted to be 89±9%, as an average value over 60 TEM images (Figure 4.2D). This short interparticle distance is most relevant for a successful performance in SERS spectroscopy experiments, as shown below. Indeed, strong plasmon coupling was observed by UV-vis spectroscopy on such an AuNTs monolayer (Figure 4.2E) revealed a significant LSPR shift of more than 150 nm, from ca. 650 nm in bulk solution up to ca. 810 nm.

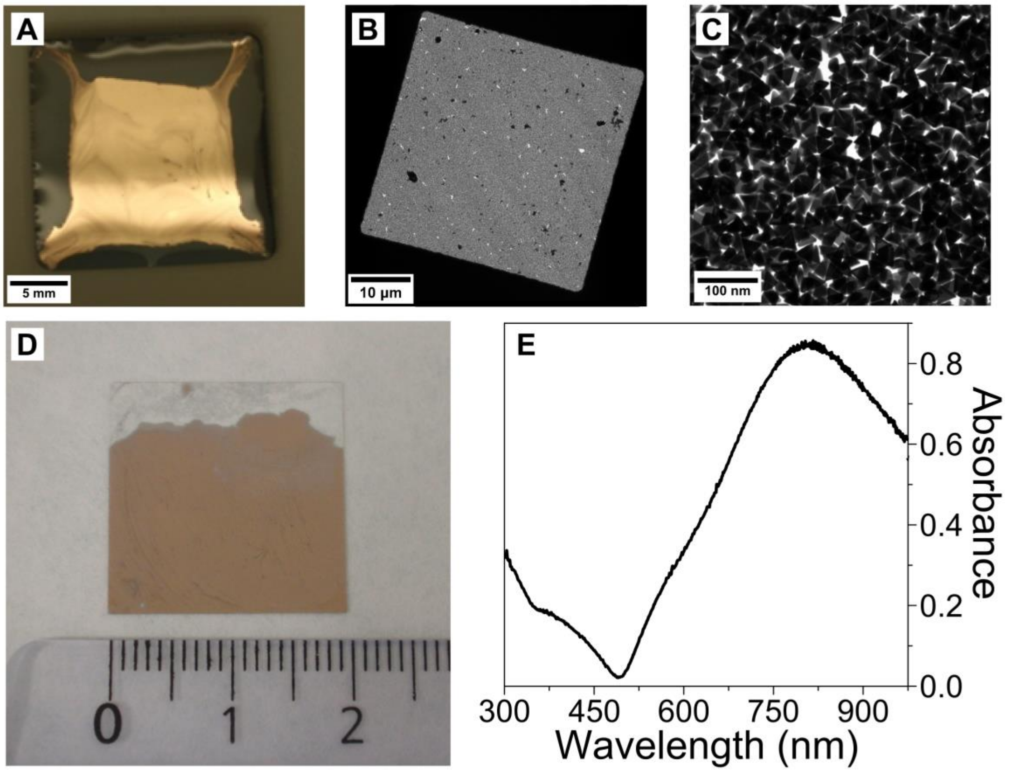

**Figure 4.2.-** Self-Assembly of AuNTs@PVP. A: Optical photograph of an AuNT@PVP monolayer organized at the air-water interface. B,C) TEM images of an AuNT@PVP monolayer upon transfer onto a TEM grid (additional TEM images are provided in the Supporting Information, Figure S21). D) Optical photograph of an AuNT@PVP monolayer on a glass slide. The scale is indicated by the ruler. E) UV-vis spectrum of the AuNTs monolayer transferred onto a transparent glass substrate. The absorption maximum of the LSPR band is located at ca. 810 nm**.**

### 4.2.4. SERS Performance

The plasmonic response of AuNTs allowed us to study their SERS performance, both in solution from well separated nanoparticles (no aggregation) and from solid substrates, where plasmon coupling due to close proximity is expected. SERS was measured in aqueous solution using molecules with different binding affinities toward Au nanoparticles, namely the thiols benzenethiol (BT) and 4-mercaptopyridine (4-MP), the dye crystal violet (CV) and the explosive 2,4-dinitrotoluene (2,4-DNT). BT binds covalently to the Au surface via formation of a

2.3 eV strong Au-S bond,[23,24] whereas the polar 4-MP preferentially binds via the thiol group but can also interact via the pyridine nitrogen. In the cationic CV, the electrostatic bond is stronger than in the neutral 2,4-DNT which interacts with the Au NPs via nitro groups. Figure 4.3A shows the SERS spectra of BT for different concentrations ranging from $10^{-5}$ to $10^{-8}$ M. The characteristic vibrations observed at 1575, 1076, 1025, 1001, and 696 $cm^{-1}$ can be clearly identified for BT concentrations down to $10^{-7}$ M, whereas the spectrum at $10^{-8}$ M shows the three most intense vibrations, with less intense vibrations being below the detection limit. All the detected vibrational modes are in good agreement with reported SERS spectra for BT,[25] with the peaks between 1600 and 900 $cm^{-1}$ assigned to ring deformation modes, namely C-C asymmetric stretching, ring in-plane deformation and C-C symmetric stretching, ring out-of-plane deformation and C-H out-of-plane bending. The low frequency modes at 473 and 417 $cm^{-1}$ correspond to the C-S out-of-plane bending and C-S stretching combined with the ring in-plane deformation mode, respectively.[26,27] The polar 4-MP only shows very strong signal at high concentration ($10^{-5}$ M) but rapidly decreased by a factor 70 for $10^{-6}$ M (Figure 4.4A). Most intense modes were found at 1576, 1096, 1065, 1003 and 998 $cm^{-1}$, in agreement with earlier reports.[28-30] The SERS spectrum from a 4-MP $10^{-8}$ M solution exhibits a very low signal to noise ratio, and only the most intense mode at 1065 $cm^{-1}$ could be detected, with 600 fold lower intensity compared to the $10^{-5}$ M solution. Figure 4.3B shows the surface-enhanced resonant Raman scattering (SERS) spectra for CV with concentrations ranging between $10^{-6}$ and $10^{-8}$ M, at an excitation wavelength of 633 nm. Whereas very strong SERS signals were detected from $10^{-6}$ to $10^{-7}$ M, the intensities at $10^{-8}$ M are low with respect to the background but all the main modes at 1618, 1376, 1169, 913, 799 and 722 $cm^{-1}$ can be clearly identified. The background is related to CV fluorescence, probably originated from free molecules in solution. At an excitation wavelength of 785 nm, the fluorescence background significantly decreases but also SERS is found to be less efficient (Figure 4.4B), as expected when the resonance condition is lost. A lower SERS response was observed for the explosive 2,4-DNT. The two dominant modes at 1345 and 881 $cm^{-1}$ corresponding to $NO_2$ stretch and bending out-of plane modes could only be detected down to $10^{-4}$ M (Figure 4.4C),[31] most likely because of the lower affinity of the analyte to Au surface.

Quantification of the SERS performance was carried out through determination of the enhancement factor. In colloidal dispersions, the analytical enhancement factor (AEF) of a nanoparticle ensemble can be estimated through the ratio between the SERS intensity for the selected mode of a given analyte ($I_{SERS}$) and the corresponding Raman intensity ($I_{RS}$) under identical experimental conditions (sample preparation, laser wavelength and power, objectives, exposition time etc.), using the following equation:[32]

$$AEF = \frac{I_{SERS}}{I_{RS}} \frac{C_{RS}}{C_{SERS}} \qquad [4.1.]$$

where $C_{SERS}$ and $C_{RS}$ are the concentrations of the analyte in the SERS and Raman experiments, respectively. Additional contribution to SERS originating from molecular resonances upon 785 nm excitation were avoided by using the non-resonant BT as analyte for AEF estimation. With $C_{RS} = 10^{-1}$ M, $C_{SERS} = 10^{-7}$ M, $I_{RS}$ (1002 $cm^{-1}$) = 6094 and $I_{SERS}$ (999 $cm^{-1}$) = 708, the AEF was estimated to be 1.2 x $10^5$. This value lies within the highest AEF presented in the literature for metal nanoparticle colloids.[32]

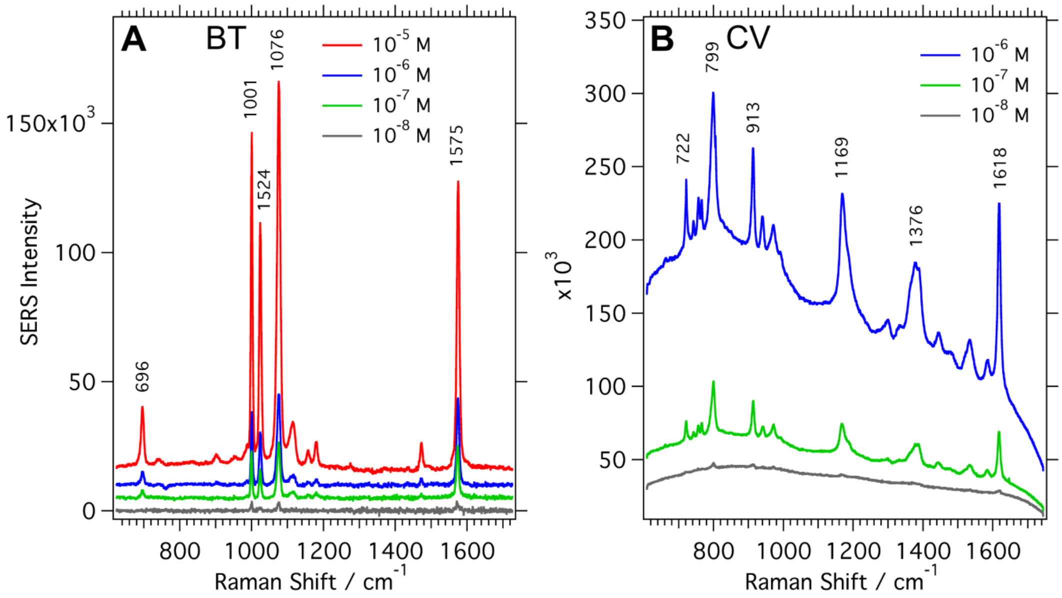

**Figure 4.3.-** SERS performance of AuNTs in solution. SERS spectra of BT excited at 785 nm (A) and CV excited at 633 nm (B), with concentrations varying between $10^{-5}$ and $10^{-8}$ M. In A an offset was applied to improve data presentation. In B the SERS spectra are not background corrected, showing significant fluorescence from dissolved CV, and are presented without offset.

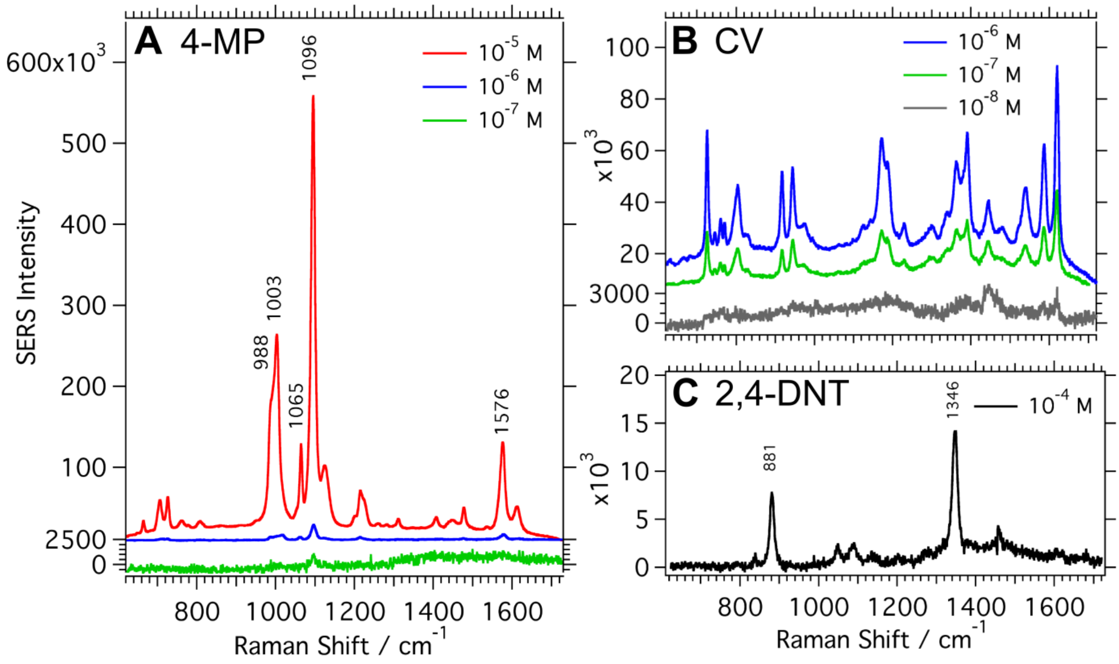

**Figure 4.4.-** SERS spectra of A) 4-MP solution within the concentration range of $10^{-5}$ to $10^{-7}$ M. B) CV solution within the concentration range of $10^{-6}$ to $10^{-8}$ M. C: 2,4-DNT solution with concentration of $10^{-4}$ M at excitation 785 nm. The spectra are background corrected. In A and B an offset was applied to improve the data presentation.

The SERS performance of dense AuNT monolayers was studied using the same analytes with concentrations ranging from $10^{-5}$ to $10^{-8}$ M. Figure 4.5 shows the average SERS spectra of BT measured on an AuNTs assembly on a glass slide and of CV on AuNTs assembled on a TEM grid. The detection limit for BT was found to be $10^{-7}$ M, which is 1 order of magnitude higher than in solution. At lower BT concentrations the SERS signature could not be unambiguously resolved because of interference with background bands originating from PVP and other contaminations. In contrast, CV could be detected on the assembled films down to the same level as in solution, without interference with signals originating from the background at an excitation wavelength of 633 nm (Figure 4.5B). SERS mapping of the AuNTs assembly containing BT was carried out to study the intensity distribution over larger areas. The SERS images for the vibrations at 1075 and 1575 $cm^{-1}$ over a surface area of ca. 80 $\mu m^2$ show nearly identical signal distribution of areas with higher and lower intensities (brighter and darker spots) for both modes (see insets in Figure 4.5A). The fluctuations can be related to the formation of hotspots with different electromagnetic field enhancement, due to the random order of AuNTs. Walker *et al.* showed that the SERS efficiency of randomly assembled AuNTs is ca. one order of magnitude lower than that for the corresponding ordered crystalline assembly over a small area within a coffee ring.[21] The observed variation of the intensity ratio can be caused by small changes of the molecular orientation with respect to the surface, leading to different mode-dependent SERS cross sections. Nonetheless, the SERS intensity in our samples is relatively homogeneous and thus this system is a promising candidate for SERS applications along with other anisotropic AuNPs such as nanostars and nanorods.

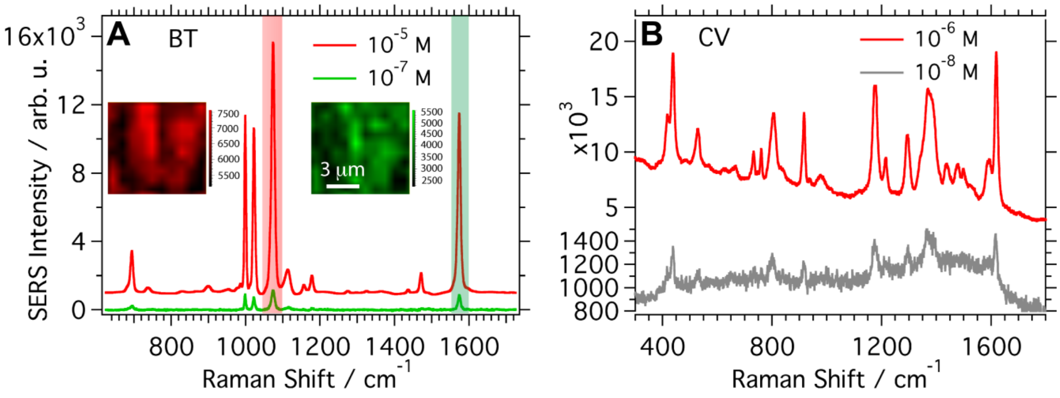

**Figure 4.5.-** SERS performance of self-assembled AuNTs. Concentration dependent average SERS spectra obtained from a large scale mapping of BT excited with 785 nm (A) and CV excited with 633 nm (B) onto an AuNTs monolayer. The insets in A are SERS maps of the scanned area (9×9 µm$^2$) for two characteristic vibrations at 1075 cm$^{-1}$ (red) and 1575 cm$^{-1}$ (green), for a BT concentration of $10^{-7}$ M (green spectrum). The SERS spectra in B are not background corrected and are presented without offset.

## 4.3. Conclusions

In this chapter we have demonstrated that the unique optoelectronic properties of gold nanotriangles significantly improve the SERS detection of various molecules. Monodisperse AuNTs with 95% shape-yield were self-assembled at the air/liquid interface to obtain monolayers with dimensions that could be easily increased up to several square centimeters. SERS performance was tested over these substrates and in solution for BT, 4-MP, CV and 2,4-DNT within the concentration range of $10^{-5}$ to $10^{-8}$ M and a remarkable AEF of 1.2 x $10^5$ was obtained for a BT solution.

## 4.4. Experimental Section

### 4.4.1. Materials

Hexadecyltrimethylammonium chloride (CTAC, 25 wt % in water), hydrogen tetrachloroaurate trihydrate ($HAuCl_4 \cdot H_2O$, ≥99.9%), L-ascorbic acid (≥99%), polyvinylpyrrolidone (PVP, average molecular weight: 10,000), thiophenol (>98%), sodium iodide (≥99.5%), sodium borohydride ($NaBH_4$, 99%), hexane (≥95%) and ethanol (>99.9%, absolute grade) were purchased from Aldrich. All chemicals were used as received. Milli-Q water (resistivity 18.2 MΩ·cm at 25 °C) was used in all experiments. All glassware was washed with aqua regia, rinsed with water, sonicated 3 times for 3 min with Milli-Q water and dried before use.

### 4.4.2. Synthesis and Purification of AuNTs

The synthesis of AuNTs involves three consecutive steps: 1) generation of CTAC coated Au seeds, 2) fast addition of the generated seeds to a final growth solution and, 3) purification of the products (see **Scheme 4.1**).

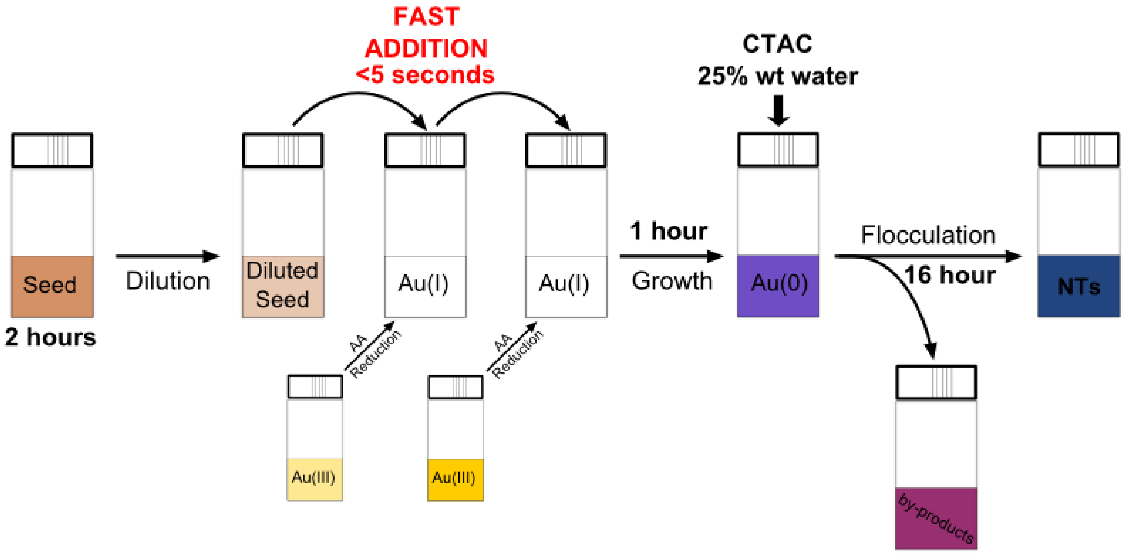

**Scheme 4.1.-** Scheme representing the overall procedure for the synthesis and purification of AuNTs.

### 4.4.3. Synthesis of Seed@CTAC

The initial seeds were prepared by the standard CTAC/$NaBH_4$ procedure: 25 µL of a 0.05 M $HAuCl_4$ solution was added to 4.7 mL of 0.1 M CTAC solution; 300 µL of a freshly prepared 0.01 M $NaBH_4$ solution was then injected under vigorous stirring. Excess borohydride was consumed by keeping the seed solution for 2h at room temperature prior to use.

### 4.4.4. Synthesis of AuNTs@CTAC

In a typical synthesis of 40 mL AuNTs solution ( the following two growth solutions were prepared: 1) 1.6 mL of 0.1M CTAC solution was added to 8 mL of Milli-Q water, followed by 40 µL of 0.05 M $HAuCl_4$ and by 15 µL of 0.01 M NaI solutions; 2) 500 µL of 0.05 M $HAuCl_4$ solution was added to 40 mL of 0.05 M CTAC, followed by 300 µL of 0.01 M NaI solution. The first solution was used to grow the CTAC capped seed into larger nanoparticles, while the second solution was used as the NTs growth batch. Before proceeding, the initial seed@CTAC solution was diluted 10× in a 0.1 M CTAC solution. Subsequently, 40 µL and 400 µL of 0.1M AA solution were added to solutions 1 and 2 respectively, and both solutions were manually stirred until the complete transparency of the solutions was achieved, indicating $Au^{III}$ to $Au^{I}$ reduction. Finally, 100 µL of diluted seed@CTAC solution was added to solution 1 (and manually stirred for 1 second), and immediately 3.2 mL of this solution was added to solution 2 (and manually stirred for a few seconds). The AuNTs dispersion was left undisturbed at room temperature for at least 1 hour. We observed that addition of 15 µL of 0.01 M NaI to solution 1 further improved the yield in NTs obtained with the fast-addition procedure.

### 4.4.5. Purification of AuNTs

After spectroscopic characterization, the AuNTs dispersion was purified by addition of 25 wt% CTAC solution to reach a final concentration of 0.15M. Flocculation of the AuNTs was completed overnight, the supernatant was then removed and the precipitated particles were redispersed in 5 mL of 0.1 M CTAC solution. Typically the concentration in $Au^0$ of the purified sample was around 1.75 mM (estimated using the absorbance at 400nm [33,34]).

### 4.4.6. PVP coating of AuNTs

AuNTs@CTAC were centrifuged (4000 rpm, 15 min, 30 °C), and the supernatant was carefully removed. The pellet was redispersed in 50 µL of 0.1 M CTAC solution, and sonicated briefly. Subsequently, water was added to reach an $Au^0$ concentration of 0.5 mM. A 10 mg/mL PVP solution was prepared, sonicated for 10 min and finally added under vigorous stirring to the AuNTs to achieve a final

PVP concentration of 1 mg/mL. This solution was stirred overnight at room temperature.

### 4.4.7. Self-Assembly of AuNTs@PVP at water-air interface

The AuNTs@PVP were centrifuged and redispersed in ethanol:hexane at a 2:3 volume ratio. Ethanol was added first and gentle stirring for a few seconds was required for a successful dispersion. Small amounts of water might affect the stability of the dispersion, leading to phase separation. Self-assembly of the AuNTs was performed as follows: the AuNTs@PVP dispersion was gently placed on top of the pure water surface. Upon evaporation of the organic solvents, the AuNTs monolayer became gold-like. Transfer of the AuNTs monolayer onto a solid substrate was performed by gently touching it with the substrate parallel to the surface, which is known as "horizontal lifting" or "Langmuir-Schaeffer" technique. Transfer onto a TEM grid was performed to acquire TEM images. Transfer onto a glass substrate was also performed to get optical photographs, UV-vis spectra and SERS measurements. Glass slides (20×20 $mm^2$; Menzel-Gläser, Thermo Scientific, Germany) were thoroughly cleaned by ultrasonication in: water with soap, ethanol, and acetone, 15 minutes for each solvent. After this cleaning procedure, the glass slides were thoroughly rinsed with Milli-Q ultrapure water and gently blow-dried with a stream of $N_2$ gas. Substrates were stored in sealed Petri dishes.

### 4.4.8. Sample Preparation for SERS Measurements

The SERS enhancing performance of the AuNT assemblies was tested using benzenethiol (BT), 4-mercaptopyridine (4-MP), crystal violet (CV) and 2,4-dinitrotoluene (2,4-DNT) as a standard analytes in different concentrations. Consecutive Milli-Q water dilutions of a 1 mM BT, 4-MP, CV ethanol stock solutions were performed to reach final concentrations of 100, 10, 1, 0.1 μM. The BT stock solution was freshly prepared prior to each SERS measurement. For SERS measurements in solution, the AuNT colloids were stabilized in 0.1 mM CTAC to prevent the aggregation, and the nanoparticle concentration set to [$Au^0$] = 0.5 mM. 4 μL of BT and CV stock, 100, 10 and 1 μM were added to 400 μL AuNT solutions, respectively. For SERS measurements of CV on solid samples, after deposition of the AuNTs@PVP, the glass slides were treated with UV/ozone (UV/Ozone ProCleaner; Bioforce Nanoscience, Ames, IA, U.S.A.) for 30 min and 7 μL of analyte solution evenly spread over the assembled AuNTs and the SERS spectra were collected after complete drying overnight. For SERS measurements of BT on solid samples, prior to PVP coating and monolayer formation, the analyte was pre-incubated in solution overnight with the AuNTs@CTAC. All spectra were background corrected except for CV. The background spectra were recorded by measuring the SERS signal of the nanoparticle assembly without analyte, to discriminate possible contributions originating from residues of the polymer or its fragments.

### 4.4.9. Spectroscopic, SERS and Structural Characterization

Transmission electron microscopy (TEM) images were collected with a JEOL JEM-1400PLUS instrument operating at 120kV, using carbon-coated 400 square mesh copper grids; all samples were centrifuged twice before dropping it on the TEM grid. SEM images were collected with an Ultra 55 FEG SEM, Zeiss operated at 10kV. SEM samples were prepared by spin-coating the collodial solutions on silicon substrates, previously cleaned with piranha solution. Optical extinction spectra were recorded using an Agilent 8453 UV-vis diode-array spectrophotometer. SERS spectra were recorded using a Renishaw Invia Raman microscope equipped with two Peltier-cooled CCD detectors, a Leica microscope two gratings with 1200 and 1800 lines/mm and band pass filter optics. For SERS measurements, a diode laser with emission wavelength of 633 nm and 785 nm was used and focused onto the liquid sample through an objective with 15 mm focal length and onto the solid sample through a 100× or 50× objective with NA of 0.34, 0.9 or 0.5, respectively. The liquid samples were irradiated with laser powers of 5 mW (785 nm excitation) and 0.32 mW (633 nm excitation). The solid samples were irradiated with laser powers of 0.2 mW for 785 nm and 10 ⍰W for 633 nm excitation wavelength. In solution, the SERS spectra were collected with an exposition time of 1s and 500 (BT and CV) or 300 (4-MP and 2,4-DNT) scans were accumulated. For solid samples, the exposition time was set to 1s and 1 scan accumulated. The BT SERS maps were generated by plotting the fitted peak areas of the vibrational modes at 1075 and 1575 $cm^{-1}$.

## 4.5. References

[1] Rodríguez-Lorenzo, L.; Álvarez-Puebla, R. A.; Pastoriza-Santos, I.; Mazzucco, S.; Stéphan, O.; Kociak, M.; Liz-Marzán, L. M.; García de Abajo, F. J. J. Am. Chem. Soc. 131 (2009) 4616.
[2] Liu, Q.; Cui, Y.; Gardner, D.; Li, X.; He, S.; Smalyukh, I. I. Nano Lett., 10 (2010) 1347.
[3] Duncan, B.; Kim, C.; Rotello, V. M. J Control. Release 148 (2010) 122.
[4] Wilczewska, A. Z.; Niemirowicz, K.; Markiewicz, K. H.; Car, H. Pharmacol. Rep. 64 (2012) 1020.
[5] DuChene, J. S.; Niu, W.; Abendroth, J. M.; Sun, Q.; Zhao, W.; Huo, F.; Wei, W. D. Chem. Mater. 25 (2013) 1392.
[6] Millstone, J. E.; Métraux, G. S.; Mirkin, C. A. Adv. Funct. Mater., 16 (2006) 1209.
[7] Banholzer, M. J.; Harris, N.; Millstone, J. E.; Schatz, G. C.; Mirkin, C. A. J. Phys. Chem. C, 114 (2010) 7521.
[8] Jana, N. R. Chem. Commun. 15 (2003) 1950.
[9] Park, K.; Koerner, H.; Vaia, R. A. Nano Lett. 10 (2010) 1433.
[10] Jain, P. K.; Huang, W.; El-Sayed, M. A. Nano Lett. 7 (2007) 2080.
[11] Sánchez-Iglesias, A.; Grzelczak, M.; Pérez-Juste, J.; Liz-Marzán, L. M. Angew. Chem. Int. Ed. 49 (2010) 9985.
[12] Dong, A.; Chen, J.; Vora, P. M.; Kikkawa, J. M.; Murray, C. B. Nature, 466 (2010) 474.
[13] Li, Z.; Zhao, W.; Quinn, J.; Rafailovich, M. H.; Sokolov, J.; Lennox, R. B.; Eisenberg, A.; Wu, X. Z.; Kim, M. W.; Sinha, S. K.; *et al*. Langmuir, 11 (1995) 4785.
[14] Zhu, J.; Eisenberg, A.; Lennox, R. B. J. Am. Chem. Soc., 113 (1991) 5583.
[15] Mahmoud, M. A.; Tabor, C. E.; El-Sayed, M. A. J. Phys. Chem. C, 113 (2009) 5493.
[16] Lee, Y. H.; Lee, C. K.; Tan, B.; Rui Tan, J. M.; Phang, I. Y.; Ling, X. Y. Nanoscale 5 (2013) 6404.
[17] Langille, M. R.; Personick, M. L.; Zhang, J.; Mirkin, C. A. J. Am. Chem. Soc., 134 (2012) 14542.
[18] Mason, T. Phys. Rev. E, 66 (2002).
[19] A. Vrij. Physica A, 235 (1997) 120.
[20] D. Fennell Evans; Håkan Wennerström. *The Colloidal Domain: Where Physics, Chemistry, Biology, and Technology Meet*; (1999).
[21] Walker, D. A.; Browne, K. P.; Kowalczyk, B.; Grzybowski, B. A. Angew. Chem. Int. Ed., 49 (2010) 6760.
[22] Deegan, R. D.; Bakajin, O.; Dupont, T. F.; Huber, G.; Nagel, S. R.; Witten, T. A. Nature, 389 (1997) 827.
[23] Saikin, S. K.; Olivares-Amaya, R.; Rappoport, D.; Stopa, M.; Aspuru-Guzik, A. Phys. Chem. Chem. Phys. 11 (2009) 9401.
[24] Whelan, C. M.; Barnes, C. J.; Walker, C. G. H.; Brown, N. M. D. Surf. Sci., 425 (1999) 195.
[25] Carron, K. T.; Hurley, L. G. J. Phys. Chem. 95 (1991) 9979.
[26] Li, S.; Wu, D.; Xu, X.; Gu, R. J. Raman Spectrosc. 38 (2007) 1436.

[27] Sriram, S.; Bhaskaran, M.; Chen, S.; Jayawardhana, S.; Stoddart, P. R.; Liu, J. Z.; Medhekar, N. V.; Kalantar-Zadeh, K.; Mitchell, A. J. Am. Chem. Soc. 134 (2012) 4646.

[28] Song, W.; Wang, Y.; Zhao, B. J. Phys. Chem. C, 111 (2007) 12786.

[29] Won Hui Do; Jae Lee Chul; Yeub Kim Dong; Maeng Joon Jung. J. Ind. Eng. Chem. 18 (2012) 2141.

[30] Zhang, L.; Bai, Y.; Shang, Z.; Zhang, Y.; Mo, Y. J. Raman Spectrosc. 38 (2007) 1106.

[31] Sylvia, J. M.; Janni, J. A.; Klein, J. D.; Spencer, K. M. Anal. Chem., 72 (2000) 5834.

[32] Le Ru, E. C.; Blackie, E.; Meyer, M.; Etchegoin, P. G. J. Phys. Chem. C, 111 (2007) 13794.

[33] Scarabelli, L.; Grzelczak, M.; Liz-Marzán, L. M. Chem. Mater. 25 (2013) 4232.

[34] Rodríguez-Fernández, J.; Pérez-Juste, J.; Mulvaney, P.; Liz-Marzán, L. M. J. Phys. Chem. B, 109 (2005) 14257.

# 5. Surface Enhanced Raman Scattering and Gated Materials for the Ultrasensitive Detection of *Mycoplasma* and Cocaine

*ABSTRACT*

*In this chapter we present a novel combination of surface-enhanced Raman scattering (SERS) as a rapid and sensitive tool for assay readout, with gated materials for the selective detection of molecules of biomedical relevance. In particular, our systems comprise mesoporous silica nanoparticles (MSNs) loaded with crystal violet (CV), a molecule with high Raman cross section, and capped with either a suitable DNA sequence for the detection of Mycoplasma genomic DNA, or with an aptamer that can selectively coordinate cocaine. In both cases the presence of the corresponding target analyte (genomic DNA or cocaine) in solution resulted in the release of CV, which was efficiently detected by SERS upon adsorption on gold nanotriangles (AuNTs), which display efficient electromagnetic field enhancement and high colloidal stability. Using this novel procedure a limit of detection of ca. 20 copies μL*$^{-1}$ *was calculated for the detection of Mycoplasma genomic DNA, whereas cocaine was detected at concentrations as low as 10 nM.*

## 5.1. Introduction

Recent advances in nanotechnology and molecular and bio-molecular chemistry have resulted in significant advances in areas such as bio-engineering, bio-sensing and bio-nanotechnology.[1–3] In this scenario materials obtained by anchoring organic molecules to pre-designed inorganic scaffolds resulted in the design of hybrid systems with a wide variety of new functionalities.[4,5] An interesting application in this field is the development of gated nano-devices that can deliver an entrapped cargo when selected external stimuli are applied. These gated materials consist of a suitable inorganic support that acts as a nanocontainer and a switchable "gate-like" molecular construct capable of being "opened" or "closed" at will.[6,7] Mesoporous silica nanoparticles (MSNs) are suitable inorganic scaffolds for gated ensembles because they contain tailor-made homogeneous pores of *ca.* 2-10 nm, are highly inert, easy to functionalize *via* well-known chemistries, and have a remarkable load capacity dictated by large specific surface area and specific volume.[8,9] MSNs have been functionalized with a wide variety of switchable molecular, supramolecular and bio-molecular pore-capping systems to develop gated materials capable of showing "zero release". These capped materials have been used mainly in drug delivery applications.[10–12] In contrast, their use in sensing protocols is still uncommon and relatively few examples are available.[13,14] For the development of sensory nanoprobes based on MSNs, the inorganic scaffold is loaded with a suitable reporter and the capping mechanism is designed so that only the target analyte is able to induce pore opening and delivery of the reporter.[13,15–17]

On the other hand, surface enhanced Raman scattering (SERS) is a highly sensitive and selective vibrational spectroscopic technique that allows the detection of molecules at very low concentrations, additionally providing structural information.[17-19] The efficiency of SERS is highly dependent on the electromagnetic field enhancement provided by the interaction between adsorbed molecules and the surface of plasmonic nanoparticles. Gold nanoparticles (AuNPs) in particular have been extensively used because of their high chemical stability and the possibility to tailor their plasmon resonances over the visible and near infrared (NIR) wavelength ranges,[20] which are most appropriate for Raman scattering measurements.[21,22] As a consequence, AuNPs have been used for SERS detection of many different biological targets including simple biomolecules, proteins, and living cells.[23–32]

In this scenario we envisioned SERS as a complementary sensing technique, in combination with capped MSNs that could specifically respond to a certain stimulus, as a suitable approach for the design of novel advanced sensing materials. In previous reports of capped materials for sensing applications the recognition event was typically monitored by optical or spectroscopic techniques.[13,28] In contrast, the high performance of SERS offers very attractive advantages for the development of sensing platforms, definitely rivaling with fluorescence and optical measurements.[33,34] Based on these concepts, a convenient design of the SERS-based capped system can be envisioned for which MSNs are capped with a certain molecule, so that selective uncapping in the presence of the target analyte leads to release of a high-cross section SERS molecule that is readily detected using suitable dispersed plasmonic nanoparticles. When the Raman reporters are stored in the MSNs, they are too far away from the metal nanoparticle surface and the SERS effect does not occur, but when released upon analyte-triggered uncapping, SERS signals arise. We propose that this simple design could contribute to the development of highly specific and ultra-sensitive nanodevices for easy and quick identification of a wide variety of target molecules and biomolecules. To demonstrate the general application of this approach, we present here two different sensing systems. In both cases MSNs were loaded with crystal violet (CV) and capped with an oligonucleotide, either for the detection of *Mycoplasma* genomic DNA or for the detection of cocaine. In both cases the presence of the corresponding target analyte (genomic DNA or cocaine) was expected to result in CV release that should be detected by SERS in the presence of gold nanotriangles (AuNTs).

## 5.2. Results and Discussion

### 5.2.1. Design of the Sensing Material

The different material fabrication steps and the sensing mechanism are illustrated in **Scheme 5.1**. Nanoparticulated MCM-41 mesoporous solids were synthesized in alkaline media following well-known procedures that make use of the cationic surfactant *n*-cetyltrimethylammonium bromide (CTAB) as directing agent for condensation of the inorganic precursor tetraethylorthosilicate (TEOS).[35] The obtained powder was washed and the surfactant was subsequently removed by calcination. Then, the obtained MSNs were loaded with CV, followed by grafting of 3-aminopropyltriethoxysilane (APTES) on the external surface (**S1**). Aminopropyl moieties are partially charged at neutral pH and display electrostatic interactions with negatively charged oligonucleotides. Addition of the oligonucleotide **O1** (5’-GGG AGC AAA CAG GAT TAG ATA CCC T-3’), a sequence highly conserved in the *Mycoplasma* genome that corresponds to a fragment of the 16S ribosomal RNA subunit,[36,37] resulted in capping of the pores (**S1-O1**). The subsequent uncapping of the MSNs relies on the hybridization of the capping oligonucleotide with *Mycoplasma* genomic DNA. Pore opening leads to release of CV, which is then adsorbed on AuNTs, thereby facilitating detection by SERS spectroscopy.

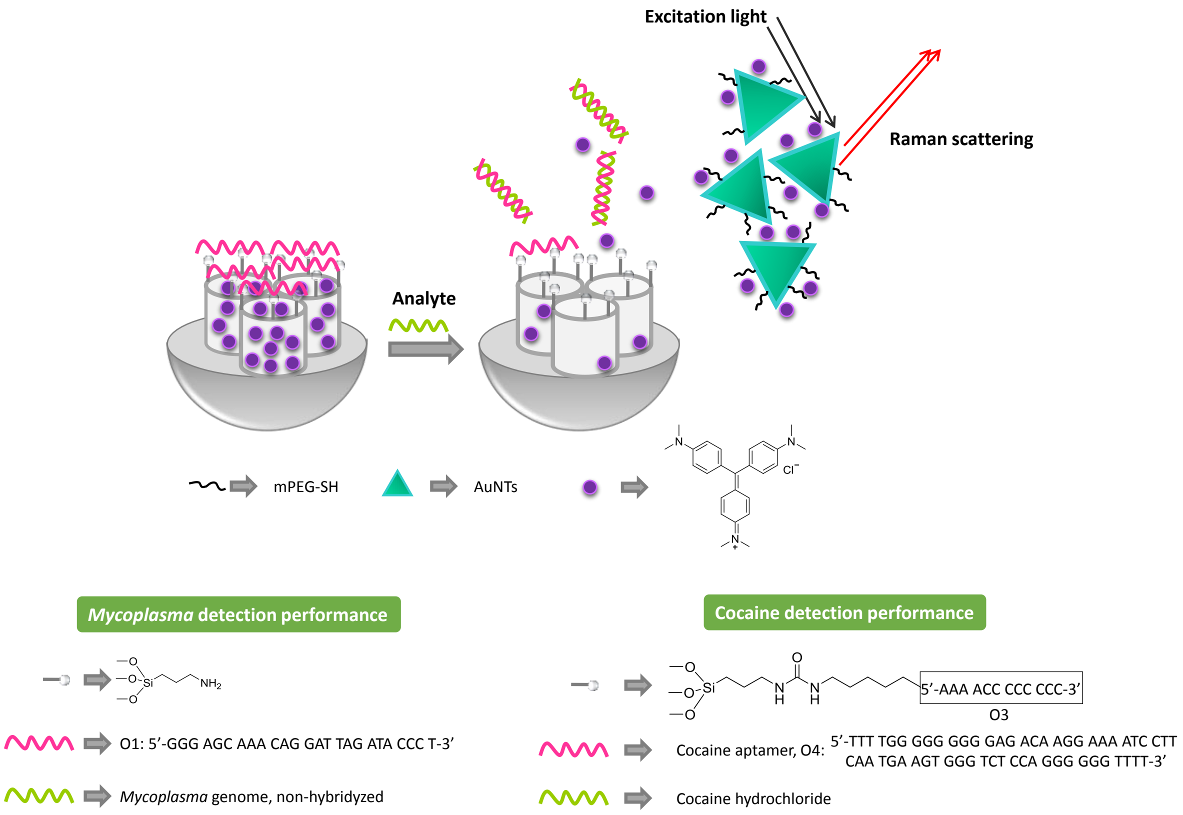

**Scheme 5.1.-** Representation of the system for *Mycoplasma* DNA and cocaine detection based on a combination of capped MSNs and SERS.

The approach followed for cocaine detection was identical, except that the CV-loaded MCM-41 support was functionalized on the external surface with (3-isocyanatopropyl) triethoxysilane (**S2**) and then, a short DNA sequence functionalized with an aminohexyl moiety at the 5'-end position, **O3** ($NH_2$-$(CH_2)_6$-5'-CCC CCC AAA AAA-3'), was covalently attached through formation of urea bonds (**S2-O3**). Finally, addition of **O4** (5'-TTT TGG GGG GGG GAG ACA AGG AAA ATC CTT CAA TGA AGT GGG TCT CCA GGG GGG TTT T-3') blocked the pore outlets by hybridization with the immobilized oligonucleotide **O3**. This resulted in the final solid **S2-O4**. The presence of cocaine in solution was expected to displace the aptamer from the solid, due to the aptamer-drug interaction, with the subsequent pore opening and dye release. Again, the signaling event is measured *via* the SERS signal of CV.

An additional task toward the design of the sensing systems was the optimization of the (size and shape of) SERS reporters. SERS efficiency is highly dependent on the morphology of the nanoparticles, as it governs the resulting surface plasmon resonance properties. Among the different available shapes, spherical gold nanoparticles are easy to prepare and to functionalize but anisotropic gold nanoparticles are expected to have higher SERS activity due to larger electromagnetic field confinement at sharp edges or corners compared to those in smooth gold spheres.[38,39] Thus, we prepared AuNTs as a potentially more efficient enhancing system (Figure 5.1). SERS efficiency of these two morphologies was compared in solutions containing different concentrations of CV (Figure 5.2), which confirmed the higher efficiency of AuNTs, so these were selected for subsequent experiments.

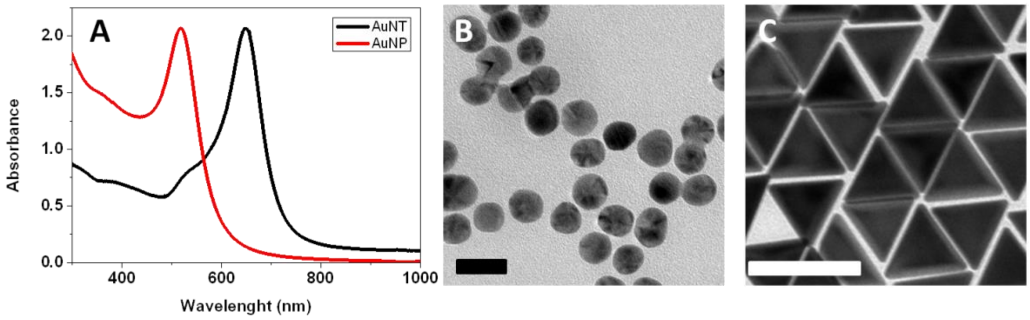

**Figure 5.1.-** Gold nanoparticles characterization. A) UV-vis-NIR spectra normalized at the LSPR maximum for hydrosols containing gold nanospheres (AuNP, black line) and gold nanotriangles (AuNT, red line). B**)** TEM images of 13 ± 1 nm AuNP. Scale bar: 20nm. C) TEM image of 66 ± 3 × 25 nm AuNT. Scale bar: 100nm.

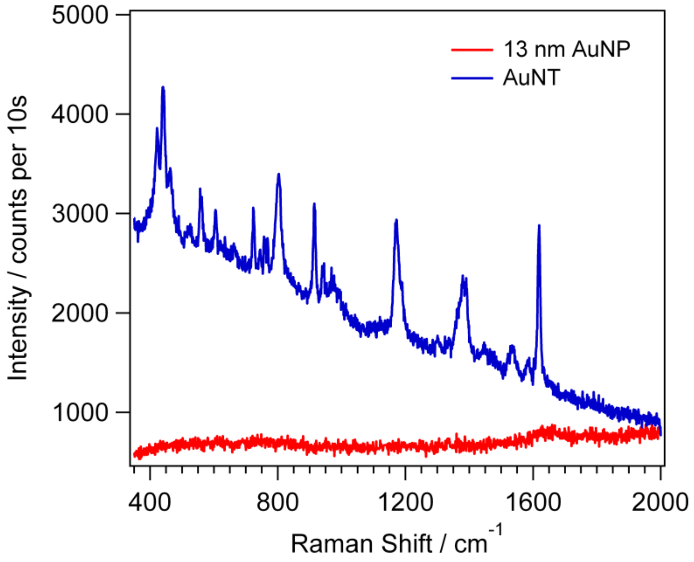

**Figure 5.2.-** SERS performance of isotropic *vs.* anisotropic gold nanoparticles. SERS signal of a 1 µM CV solution containing AuNT@mPEG-SH (blue line) and 13 nm AuNP@mPEG-SH (red line). Both spectra were not background corrected. Measurement parameters: $P_{laser}$ = 1.2 mW, $t_{int}$ = 10s.

An additional challenge however was the stabilization of (relatively large) AuNTs in a medium with high ionic strength (20 mM Tris - 37.5 mM $MgCl_2$), which was required to facilitate DNA hybridization. We therefore investigated the stabilization of nanoparticles functionalized with a thiolated polyethyleneglycol ligand (mPEG-SH). AuNTs were functionalized with *ca.* 10 mPEG-SH molecules/nanoparticle (AuNT@PEG), which was found to be enough to preserve the stability of the nanoparticles without affecting CV adsorption. As shown in Figure 5.3, quenching of CV fluorescence was observed in the presence of AuNTs indicating that the dye was indeed located in the proximity of the nanoparticles.

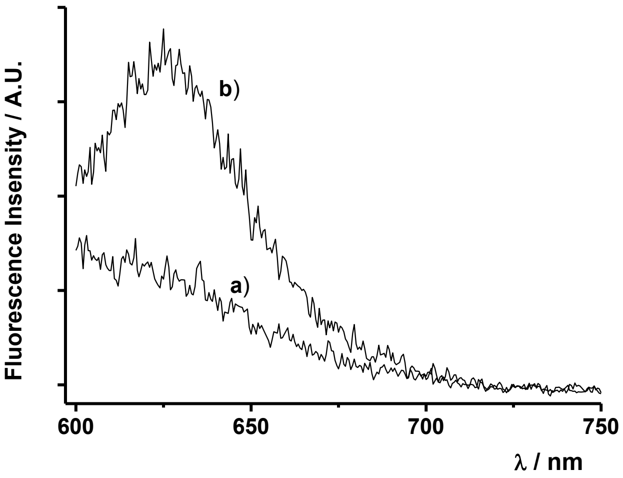

**Figure 5.3.-** CV fluorescence quenching: Fluorescence spectra ($\lambda_{exc}$ = 590 nm)of a 1 µM CV aqueous solution in the presence (a) and in the absence of AuNTs. [$Au^0$=0.5mM]

### 5.2.2. Materials Characterization

The MSN-based materials were characterized by using standard techniques. Powder X-ray diffraction of as synthesized MCM-41 (curve a in Figure 5.4) showed four low-angle reflections, typical of a hexagonal mesoporous array, which can be indexed as (100), (110), (200), and (210) Bragg peaks. Moreover the presence and high intensity values of the (100) reflections in calcined MCM-41 and in **S1** and **S2** (curves b, c, d in Figure 5.4) confirmed that the loading with CV and further functionalization of the external surface did not modify the 3D mesoporous structure. TEM analysis of all the materials confirmed the presence of the mesoporous structure and the typical channels of the MCM-41 network were visualized as alternate dark and light stripes (see Figure 5.4). TEM images also showed that MCM-41 support and solids **S1** and **S2** are spherical particles of *ca.* 100 nm diameter.

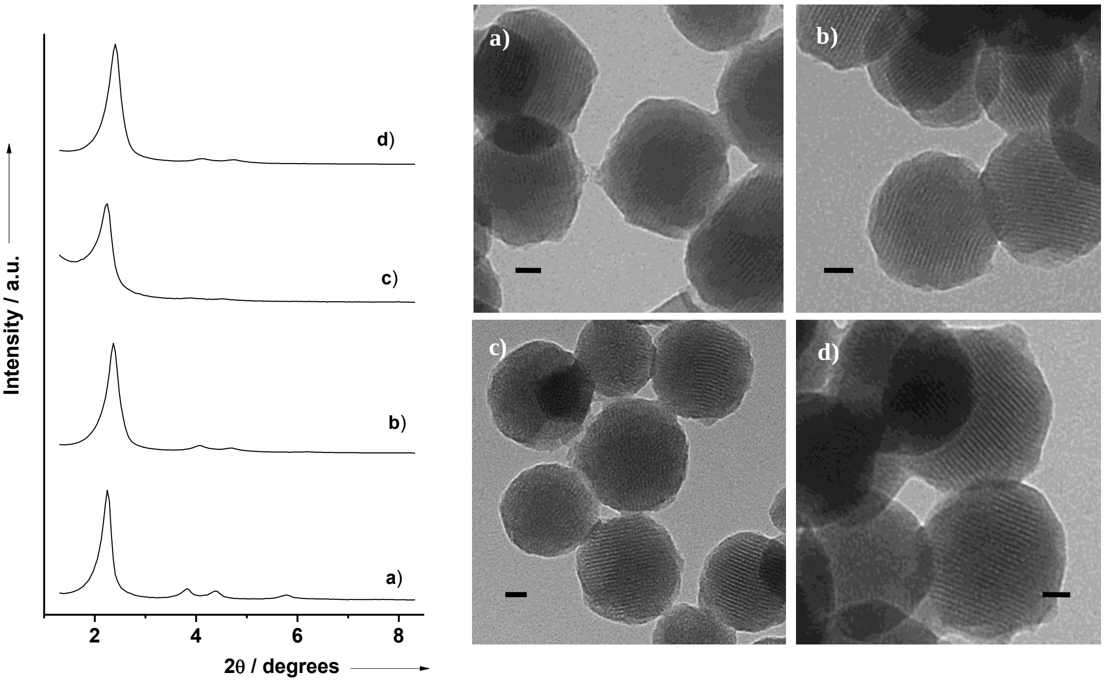

**Figure 5.4.- Left panel**: Powder X-ray diffraction patterns of the solids: (a) MCM-41 as synthesized, (b) calcined MCM-41, (c) solid **S1** containing crystal violet and functionalized with 3-aminopropyltriethoxysilane, and (d) solid **S2** containing crystal violet and functionalized with 3-(triethoxysilyl)propyl isocyanate. **Right panel**: TEM images of: (a) as prepared MCM-41, (b) calcined MCM-41, (b) solid **S1** and (c) solid **S2,** showing the typical porosity of the MCM-41 mesoporous matrix. Scale bar: 20 nm.

$N_2$ adsorption-desorption isotherms of the calcined MCM-41 material displayed a step at intermediate $P/P_0$ value (0.1-0.3) typical of this type of solids (Figure 5.5). Pore volume was calculated by applying the BJH model[40] on the adsorption branch of the isotherm and the total specific surface area was calculated by using the BET model[41] (values are listed in Table 5.1). On the other hand, the $N_2$ adsorption-desorption isotherms of **S1** and **S2** were typical of mesoporous systems with partially filled mesopores (see Figure 5.6), and a significant decrease in the adsorbed $N_2$ volume and surface area was observed (see Table 5.1).

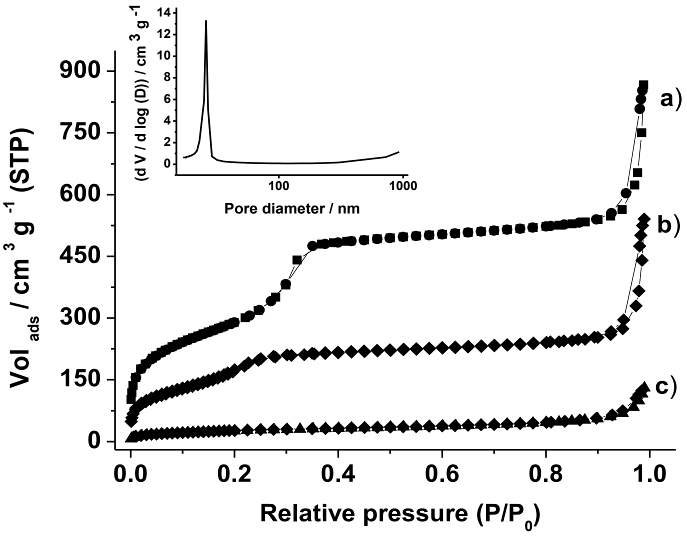

**Figure 5.5.-** Nitrogen adsorption-desorption isotherms for (a) MCM-41 mesoporous material, (b) **S2** and c) **S1** materials. Inset: Pore size distribution of MCM-41 mesoporous material.

**Table 5.1:** BET specific surface values, pore volumes and pore sizes calculated from the $N_2$ adsorption-desorption isotherms for selected materials.

| *Solid* | *$S_{BET}$ (m$^2$ g$^{-1}$)* | *Pore Volume (cm$^3$ g$^{-1}$)* | *Pore diameter (nm)* |
|---|---|---|---|
| ***MCM-41*** | 1055.5 | 0.86 | 2.62 |
| ***S1*** | 98.5 | 0.19 | - |
| ***S2*** | 637.9 | 0.42 | - |

The organic content in the functionalized nanoparticles were determined by elemental and thermogravimetric analysis (see Table 5.2). Moreover, the content of oligonucleotide in **S1-O1**, **S2-O3** and **S2-O4** was calculated by measuring the absorbance of the oligonucleotides **O1**, **O3** and **O4** at 260 nm after the capping process. Contents of 0.168, 0.017 and 0.085 mmol g$^{-1}$ of solid were determined for

**O1**, **O3** and **O4**, respectively. In addition, the corresponding hydrodynamic diameters were measured by dynamic light scattering (DLS) at room temperature (see Figures 5.6 and Table 5.3).

**Table 5.2:** Content of 3-aminopropyltriethoxysilane, 3-(triethoxysilyl)propyl isocyanate and crystal violet (in mmol $g^{-1}$ $SiO_2$) in the prepared solids **S1** and **S2**.

| **Solid** | $\alpha_{CV}$<br>**(mmol $g^{-1}$ $SiO_2$)** | $\alpha_{APTS}$<br>**(mmol $g^{-1}$ $SiO_2$)** | $\alpha_{isocyanate}$<br>**(mmol $g^{-1}$ $SiO_2$)** |
|---|---|---|---|
| **S1** | 0.57 | 2.87 | - |
| **S2** | 0.53 | - | 0.31 |

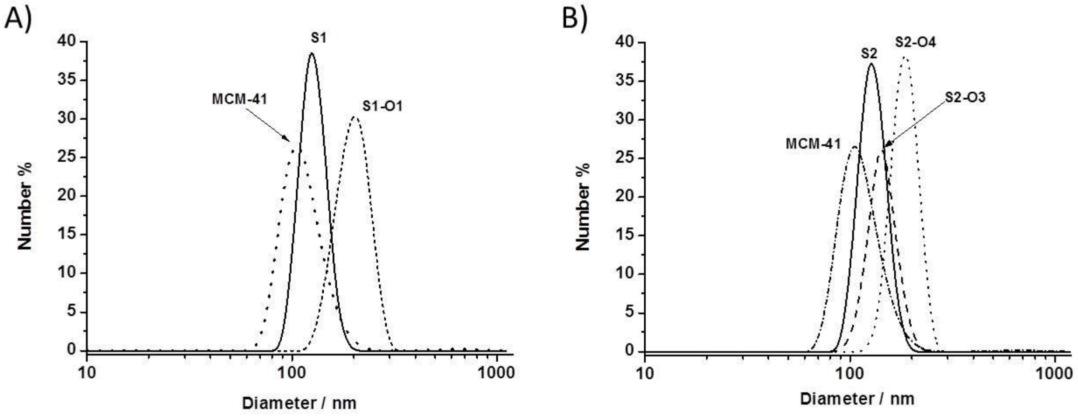

**Figure 5.6.-** A) Size distribution by number of particles obtained by DLS studies for calcined **MCM-41**, **S1** and **S1-O1**. B) Size distribution by number of particles obtained by DLS studies for calcined **MCM-41**, **S2**, **S2-O3** and **S2-O4**.

**Table 5.3:** Hydrodynamic diameter of **MCM-41**, **S1**, **S1-O1**, **S2**, **S2-O3** and **S2-O4** solids, measured by DLS.

| Solid | Particle diameter (nm) |
|---|---|
| **MCM-41** | 113.6 ± 24 |
| **S1** | 127.2 ± 15.44 |
| **S1-O1** | 177.4 ± 22.6 |
| **S2** | 129.5 ± 16.3 |
| **S2-O3** | 161.4 ± 18.7 |
| **S2-O4** | 190 ± 24 |

### 5.2.3. *Mycoplasma* Detection

*Mycoplasma* refers to a genome of prokaryotic microorganisms that have been described as parasites of various animals and plants.[42] In addition, their characteristic lack of a cell wall confers them resistance to many common antibiotics so they are often present in research laboratories as cell-culture contaminants. Hence, detection of these microorganisms is of general interest in biomedical and life sciences. For these experiments, **S1-O1** in the presence of AuNT@PEG was used. As stated above, a sequence highly conserved in the *Mycoplasma* genome that corresponds to a fragment of the 16S ribosomal RNA subunit (**O1**, 5'-GGG AGC AAA CAG GAT TAG ATA CCC T-3') was used as cap for the MSN.[16] In a first series of experiments the functionality of the system was analyzed by adding **O2** (an **O1** complementary DNA strand) to a suspension of **S1-O1**. Three non-complementary oligonucleotides (**O5**, **O6**, and **O7**) were also tested and used as specificity controls and in all cases the release of CV was monitored by both fluorescence and SERS (Figure 5.7) and the system was then optimized for SERS detection. These studies showed that the **S1-O1–**AuNTs system allowed us to selectively detect extremely low concentrations of **O2**, reaching a limit of detection as low as $10^{-9}$ M, whereas no SERS signal was obtained in the presence of the non-complementary oligonucleotides (**O5**, **O6**, **O7**).

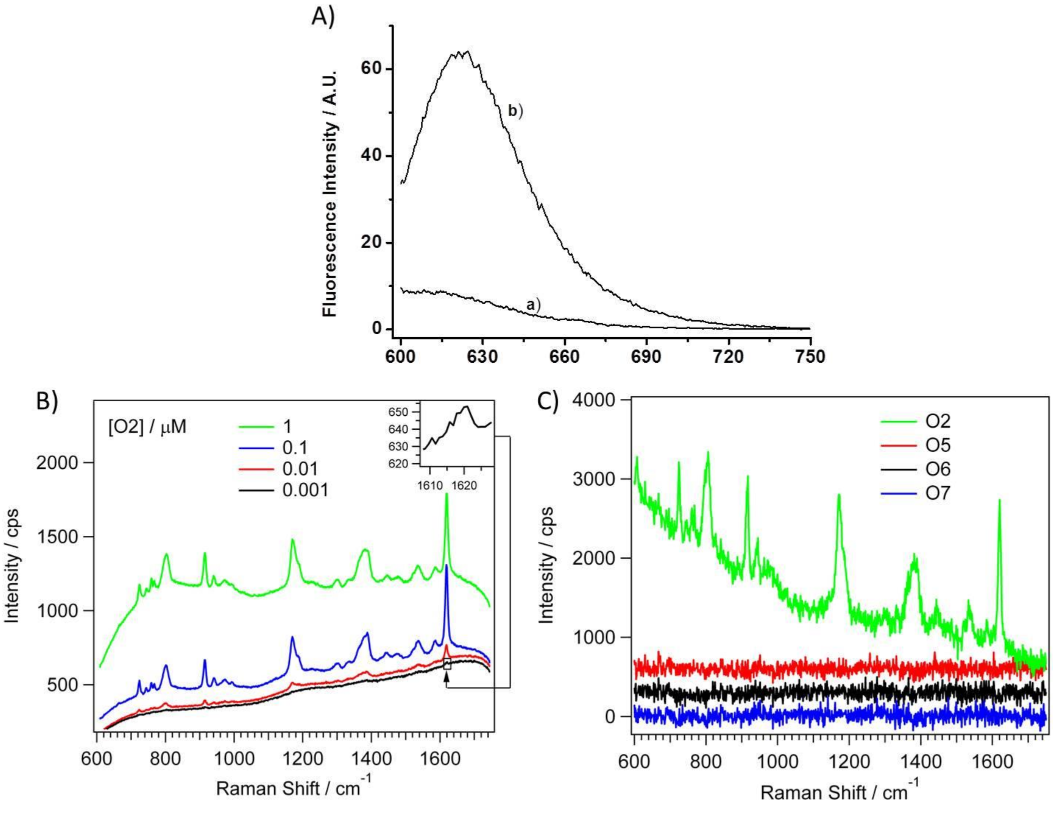

**Figure 5.7.-** A) Fluorescence spectra of crystal violet released from **S1-O1** in the absence (curve a) and in the presence (curve b) of oligonucleotide **O2**. ($\lambda_{exc}$ = 590 nm). B) Detection of CV release as a function of oligonucleotide **O2** concentration. Note that **O2** was detected at concentrations as low as 1 µM. Spectra were not background corrected. Measurement parameters: $P_{laser}$ = 6 mW, $t_{int}$ = 1s, average of 100 accumulations. C) Specifity of solid **S1-O1**. SERS detection of CV release as a function of **O2**, **O5**, **O6** and **O7**. The concentration DNA was 1 µM in all cases. Note that **O2** is complementary to **O1** while **O3**, **O4** and **O5** are non-complementary DNAs. Spectra were background corrected. Measurement parameters: $P_{laser}$ = 1.2 mW, $t_{int}$ = 10s, 1 accumulation.

After confirming the selective gate opening in the presence of complementary DNA, the response of **S1-O1** in the presence of *Mycoplasma fermentans* genomic DNA was studied. For this purpose, 1 mg of **S1-O1** was suspended in 1 mL of hybridization buffer and then two aliquots were taken from this suspension. Meanwhile, a solution containing genomic double-stranded DNA (dsDNA) of *Mycoplasma fermentans* standard ($10^3$ DNA copies $\mu L^{-1}$) was heated at 95 °C for 5 min to dehybridize dsDNA and then cooled to 50 °C. The DNA solution was added to one of the aliquots to reach a final DNA concentration of 200 copies $\mu L^{-1}$ whereas Milli-Q water (without DNA) at 50 °C was added to the second aliquot. Both suspensions were maintained at 37 °C and after 1 hour the mixtures were centrifuged to remove the solid. Subsequently, a solution containing AuNT@PEG was added to the supernatant to reach a gold concentration of 0.04 mM and SERS spectroscopy was then used to detect released CV. This procedure was then repeated for solutions containing decreasing number of *Mycoplasma fermentans* genomic DNA copies to explore the correlation between concentration of genomic DNA and amount of released CV (Figure 5.8). The recorded scattered frequencies are in good agreement ($\Delta < \pm 3$ $cm^{-1}$) with previously reported SERS spectra for CV.[43] From these studies it was observed that in the absence of the *Mycoplasma* genomic DNA solid **S1-O1** was tightly capped and showed a very low release of the dye (which we defined as background). In contrast, the presence of the target DNA induced uncapping of the pores and CV release. Regarding the sensitivity of this new approach, after subtraction of the background signal, the CV SERS signal was detectable at concentrations as low as 20 DNA copies $\mu L^{-1}$ of

*Mycoplasma fermentans*. This limit of detection represents an improvement when compared with previous works using gated materials.[44,45]

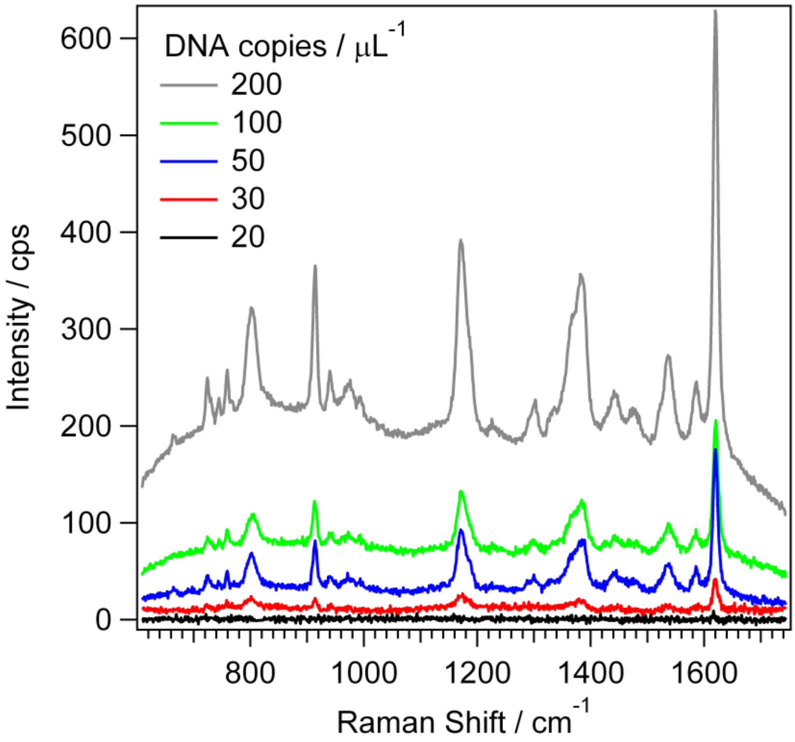

**Figure 5.8.-** Detection of CV release as a function of the number of *Mycobacterium fermentans* genomic DNA copies µL$^{-1}$. The SERS signal of CV is detectable even for concentrations as low as 20 DNA copies µL$^{-1}$. The plotted spectra represent the average of 100 individual spectra, were background corrected and an offset was applied for clearer data presentation. Measurement parameters: $P_{laser}$ = 6 mW, $t_{int}$ = 1s.

Similar experiments were carried out with solid **S1-O1** to verify the selectivity of the method, in which the genomic DNA of the pathogens *Legionella pneumophilia* and *Candida albicans* were used at a concentration of 100 copies µL$^{-1}$ (Figure 5.9). SERS analysis demonstrated that solid **S1-O1** was selective to the presence of *Mycoplasma fermentans* genomic DNA as a lower CV signal was detected in the supernatant in the presence of DNA from other pathogens.

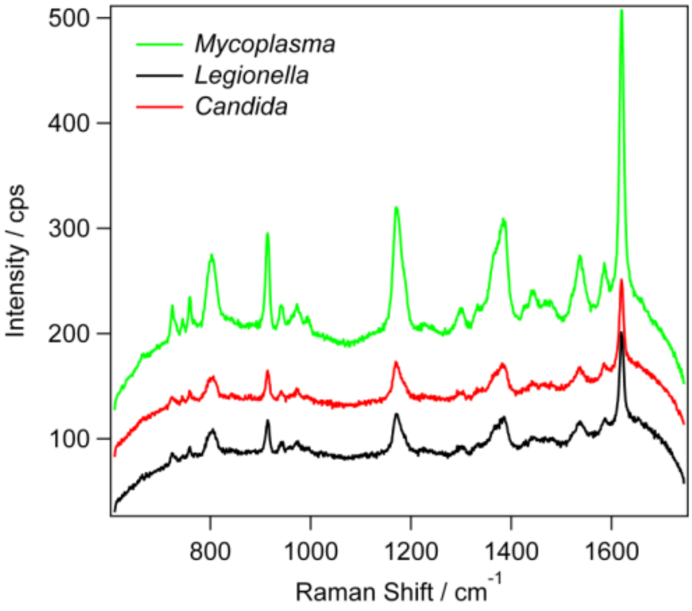

**Figure 5.9.-** SERS detection of CV release in the presence of different types of genomic DNA: *Mycoplasma fermentans* (green curve) *Legionella pneumophilia* (black curve) and *Candida albicans* (red curve). Genomic DNA concentration was set to 100 copies µL$^{-1}$. Spectra were not background corrected and an offset was applied for clearer data representation. Measurement parameters: $P_{laser}$ = 6 mW, $t_{int}$ = 1s, average of 100 accumulations.

### 5.2.4. Cocaine Detection

Encouraged by the results obtained for **S1-O1**, we devised a second biosensor, again using capped MSNs and SERS, aimed at cocaine detection. Cocaine is an alkaloid obtained from the leaves of the coca plant, which is extensively used in developed countries as an illegal recreational drug. Although cocaine production and distribution is restricted and illegal in most contexts, it is a powerful nervous system stimulant that causes strong addiction among consumers, frequently leading to serious health, social and legal problems. Therefore development of inexpensive, selective and sensitive devices for its detection is of high importance.[46–48] Our cocaine sensing system comprised MSNs loaded with CV, functionalized with the short DNA sequence **O3** and finally capped with the cocaine aptamer (**O4**), resulting in the final **S2-O4** material.

To study the response of the prepared sensory nanocarrier toward the presence of cocaine in solution, a suspension of 500 µg **S2-O4** mL$^{-1}$ in hybridization buffer (Tris-$MgCl_2$) was prepared. Then, 200 µL of this suspension was diluted with 800 µL of hybridization buffer and further separated into two aliquots. A Milli-Q water solution of cocaine (2 mM) was added to one of the aliquots to reach a final cocaine concentration of 10$^{-4}$ M whereas Milli-Q water (without cocaine) was added to the other aliquot. Both suspensions were kept under stirring at room temperature and after 1 hour the solutions were centrifuged to remove the solid content. Subsequently, a solution containing AuNT@PEG was added to the supernatant to reach a gold concentration of 0.02 mM and CV delivery was analyzed by SERS as a function of cocaine concentration (Figure 5.10). The results clearly demonstrated that the interaction of cocaine with the aptamer indeed triggers pore opening, allowing dye release and detection by SERS.

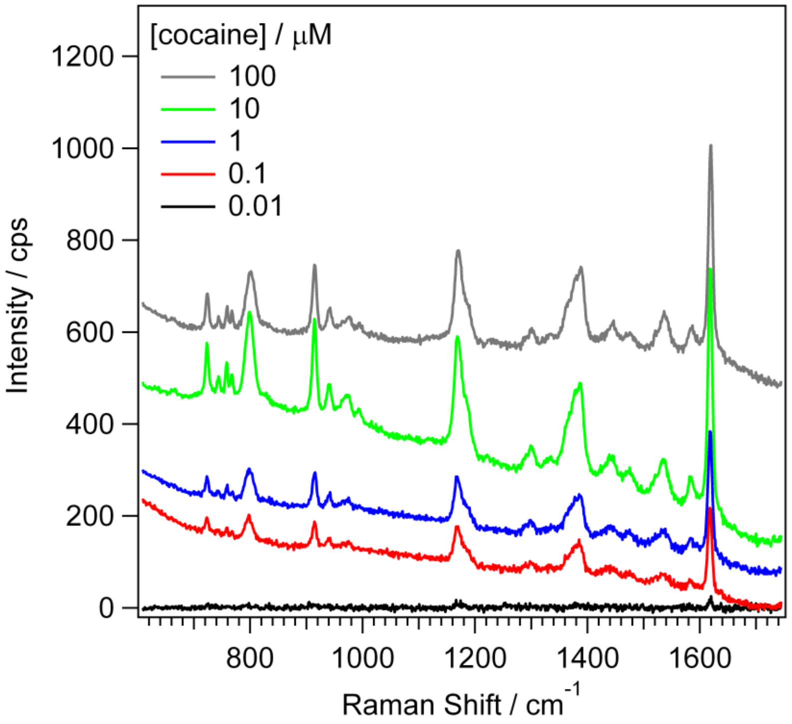

**Figure 5.10.-** Detection of CV release as a function of cocaine concentration. The characteristic SERS signal of CV was clearly detected at a concentration as low as 10 nM. The plotted spectra represent the average of 100 individual spectra, were background corrected and an offset was applied for clearer data representation. Measurement parameters: $P_{laser}$ = 6 mW, $t_{int}$ = 1s.

Upon optimization of the system, the most intense vibrations at 1617 and 1172 $cm^{-1}$ of CV were clearly detected by SERS at a cocaine concentration as low as 10 nM, indicating a high sensitivity as this result is comparable to those for other aptameric sensors based on fluorescence,[49,50] colorimetric[51,52] or electrochemical measurements.[53,54] Our results additionally provide an improvement of approximately 20-fold in the detection limit as compared to previous SERS-based aptameric cocaine sensors.[55] It is important to note that the background signal was subtracted prior to determination of the detection limit, which confirms that this method is suitable for the ultrasensitive and highly selective cocaine detection.

Control experiments were also carried out to determine the specificity of the system. Experiments in the absence of drug (background) and in the presence of other drugs such as morphine, methadone and heroine showed that **S2-O4** was highly selective to the presence of cocaine in the selected concentration range (Figure 5.11), since no cargo release was detected in the presence of other drugs.

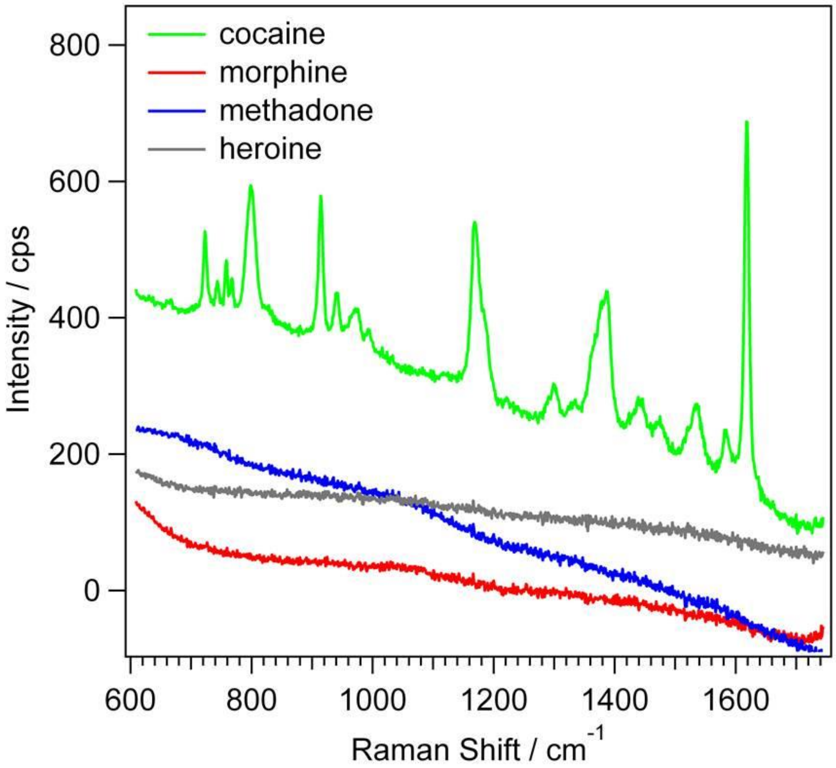

**Figure 5.11.-** Detection of CV release in the presence of different drugs. Drug concentration was 10 µM in all cases. Spectra were background corrected and an offset was applied for clearer data representation. Measurement parameters: $P_{laser}$ = 6 mW, $t_{int}$ = 1s, average of 100 accumulations.

## 5.3. Conclusions

In this chapter we have demonstrated that the combination of gated materials with SERS spectroscopy can be used for the design of highly sensitive and selective sensing systems. CV-loaded MSNs were used in combination with suitable caps and AuNT@PEG for the detection of *Mycoplasma* genomic DNA and cocaine, with limits of detection as low as 20 copies $\mu L^{-1}$ and 10 nM, respectively. In both cases a highly selective response was found. We also propose that a wide variety of SERS-active molecules can be used as cargo in different capped systems, which can be selectively opened in the presence of target analytes and combined with diverse SERS efficient plasmonic nanoparticles, rendering this approach appealing and full of potential for the design of new plasmonic biosensors.

## 5.4. Experimental Section

### 5.4.1. Materials

Hexadecyltrimethylammonium chloride (CTAC, 25 wt% in water), hydrogen tetrachloroaurate trihydrate ($HAuCl_4 \cdot H_2O$, ≥99.9%), L-ascorbic acid (AA, ≥99%), O-[2-(3-Mercaptopropionylamino)ethyl]-O′-methylpolyethylene glycol (mPEG-SH, average molecular weight: 5,000), sodium borohydride ($NaBH_4$, 99%), crystal violet (CV, ≥90%), tetraethylorthosilicate (TEOS), *n*-cetyltrimethylammonium bromide (CTAB, ≥99% ), sodium hydroxide (NaOH), tris(hydroxymethyl)aminomethane (Tris), 3-aminopropyltriethoxysilane (APTES) and 3-(triethoxysilyl)propyl isocyanatem and hydrochloric acid were purchased from Aldrich. Milli-Q water (resistivity 18.2 MΩ·cm at 25 °C) was used in all experiments. The oligonucleotides and aptamers listed in Table 5.4 were provided by Isogen Life Science. Analytical-grade solvents were from Scharlab (Barcelona, Spain). Cocaine hydrochloride, morphine, methadone and heroin hydrochloride were provided by the Agencia Española de Medicamentos y Productos Sanitarios (AEMPS). All chemicals were used as received.

**Table 5.4:** Oligonucleotides and aptamers used in this work.

| Name | Sequence |
|---|---|
| **O1** | 5’-GGGAGCAAACAGGATTAGATACCCT-3’ |
| **O2** | 5’-AGGGTATCTAATCCTGTTTGCTCCC-3’ |
| **O3** | $NH_2$-$(CH_2)_6$-5’-AAAACCCCCCCC-3’ |
| **O4** | 5’-TTTTGGGGGGGGGAGACAAGGAAAATCCTTCAATGAAGTGGGTCTCCAGGGGGGTTTT-3’ |
| **O5** | 5’-GAGGTTAACAGAGTGACAGATGGTGCA-3’ |
| **O6** | 5’-AGGGTATCTAATTGCCTGTTGCTCCC-3’ |
| **O7** | 5’-AGGGTATCTAATGGACCTGTTTGCTCCC-3’ |

### 5.4.2. General Techniques

XRD, TGA, elemental analysis, TEM microscopy, $N_2$ adsorption-desorption and UV-visible spectroscopy techniques were used to characterize the prepared materials. X-ray measurements were performed on a Brücher AXS D8 Advance diffractometer using Cu-Kα radiation. TEM images of MSNs were taken with a JEOL TEM-1010 Electron microscope working at 100 kV. TEM images of AuNPs were collected with a JEOL JEM-1400PLUS instrument operating at 120 kV, using carbon-coated 400 square mesh copper grids. $N_2$ adsorption-desorption isotherms were recorded on a Micromeritics ASAP2010 automated sorption analyzer. The samples were degassed at 120 °C in vacuum overnight. The specific surfaces areas were calculated from the adsorption data in the low pressures range using the BET model. Pore size was determined following the BJH method. Fluorescence spectroscopy was carried out on a Jasco FP-8300 Spectrometer. Optical extinction spectra were recorded using an Agilent 8453 UV-vis diode-array spectrophotometer. SERS measurements were performed by means of Renishaw inVia system consisting of a confocal Leica microscope equipped with high-resolution diffraction grating (1800 gr/mm), band pass filter optics and a Peltier-cooled CCD detector using a HeNe laser ($\lambda$=633 nm, maximal output 12.5 mW) as excitation source. The scattered frequencies (integration time, $t_{int}$) were collected for 1 and 10 s at irradiation powers ($P_{laser}$) of 6 and 1.2 mW, respectively. For the short-time data acquisitions 100 spectra were accumulated and averaged. All spectra were collected with a long-working distance 50x objective having a numerical aperture of 0.45 from the sample solution within a 1 mL glass vial (Thermo Scientific).

### 5.4.3. Buffer Solutions

Hybridization buffer consisting in 20 mM Tris-HCl, 37.5 mM $MgCl_2$ (pH 7.5) in Milli-Q water, was used for controlled release experiments.

## 5.4.4. Synthesis of MCM-41 Mesoporous Nanoparticles

An aqueous solution of NaOH (2 M, 3.5 mL) was added to a solution of *n*-cetyltrimethylammoniumbromide (CTABr, 1.00 g, 2.74 mmol) in deionized $H_2O$ (480 mL). The solution temperature was adjusted to 80 °C. TEOS (5 mL, $2.57*10^{-2}$ mol) was subsequently added dropwise to the surfactant solution. The mixture was stirred for 2 h to yield a white precipitate. The final solid was centrifuged, washed with deionized water and dried at 70°C for 18 h (MCM-41 as-synthesized). To obtain the final porous material (MCM-41), the as-synthesized solid was calcined at 550 °C under oxidizing atmosphere for 5 h to remove the template.

## 5.4.5. Synthesis of S1

The amino functionalized solid **S1** was prepared as follows: calcined MCM-41 (500 mg) and crystal violet (161 mg, 0.4 mmol) were suspended in Milli-Q water (20 mL). The suspension was stirred at room temperature for 24 h to load the MCM-41 pores. Afterward an excess of APTES (0.65 mL, 2.77 mmol) was added, and the suspension was stirred at room temperature for 5.5 h. Finally, the resulting solid was isolated by filtration, washed with Milli-Q (3 mL) water and dried at 36 °C for 18 h.

## 5.4.6. Synthesis of S1-O1

For the preparation of **S1-O1,** 450 μg of **S1** was suspended in 450 μL of a solution containing the oligonucleotide **O1 (**5’-GGGAGCAAACAGGATTAGATACCCT-3’) in a concentration of 40 μM in hybridization buffer, and the suspension was stirred at 37°C for 30 min. The final **S1-O1** solid, was isolated by centrifugation and washed with 3x1 mL of hybridization buffer in order to remove the residual dye and the free oligonucleotide **O1.**

### 5.4.7.Synthesis of S2

In a typical synthesis, calcined MCM-41 (300 mg) and crystal violet (98 mg, 0.24 mmol) were suspended in $CH_3CN$ (10 mL). The suspension was stirred at room temperature for 24 h to load the pores. Then, an excess of 3-(triethoxysilyl)propyl isocyanate (0.37 mL, 1.5 mmol) was added, and the suspension was stirred at room temperature for 5.5 h. Finally, the resulting solid was isolated by filtration, washed with 3 mL of $CH_3CN$ and dried at 36 °C for 18 h.

### 5.4.8. Synthesis of S2-O3

100 µL of oligonucleotide **O3** was added to a suspension containing 1 mg of **S2**, 2 µL of triethylamine and 700 µL of crystal violet in $CH_3CN$ (1 mM). The mixture was stirred at room temperature for 3 h. The final solid **S2-O3** was isolated by centrifugation and washed with Milli-Q water (2x700 µL) to eliminate the unbounded oligonucleotide and the dye.

### 5.4.9. Synthesis of S2-O4

In order to cap the pores of solid **S2-O3,** a portion of 200 µg of **S2-O3** was suspended in a 400 µL of a solution containing the cocaine aptamer in a concentration of 5 µM in hybridization buffer. The suspension was stirred at room temperature for 2 h, and the final solid **S2-O4** was centrifuged and washed with hybridization buffer to remove the free cocaine aptamer and the residual dye.

### 5.4.10. Gold Nanoparticles Synthesis

**Citrate-stabilized Au NPs** (13nm) were prepared by the Turkevich method.[56] Briefly, Au NPs were prepared by injecting sodium citrate (25 mL, 1.7 mM) to the boiling solution of $HAuCl_4$ (500 mL, 0.5 mM). The color of the solution changes from colorless to dark red after 10 min of reaction.

**AuNT@mPEG-SH** were synthesized by a recently reported seeded growth method.[57] In a typical experiment two growth solutions are prepared: 1) 1.6 mL of 0.1M CTAC solution was added to 8 mL of Milli-Q water, followed by 40 µL of 0.05 M $HAuCl_4$ and by 15 µL of 0.01 M NaI solutions; 2) 500 µL of 0.05 M $HAuCl_4$ solution was added to 40 mL of 0.05 M CTAC, followed by 300 µL of 0.01 M NaI solution. The first solution was used to grow the CTAC capped seed into larger nanoparticles, while the second solution was used as the NTs growth batch. Before proceeding, the initial seed@CTAC solution was diluted 10× in a 0.1 M CTAC solution. Subsequently, 40 µL and 400 µL of 0.1M AA solution were added to solutions 1 and 2, respectively, and both solutions were manually stirred until the complete transparency of the solutions was achieved. Finally, 100 µL of diluted seed@CTAC solution was added to solution 1 (and manually stirred for 1 second), and immediately 3.2 mL of this solution was added to solution 2 (and manually stirred for a few seconds). The AuNTs dispersion was left undisturbed at room temperature for at least 1 hour. Then, the AuNTs dispersion was purified by addition of 6.65 mL of 25 wt% CTAC solution to reach a final CTAC concentration of 0.15 M. Flocculation of the AuNTs was completed overnight, the supernatant was then removed and the precipitated particles were redispersed in 5 mL of 0.1 M CTAC solution. After TEM characterization the AuNTs were centrifuged (4000 rpm, 15min, 30°C) and stabilized with a suitable amount of mPEG-SH, calculated to add 10 thiols/NP. The solution was left stirring overnight for proper functionalization. Then, it was centrifuged (4000 rpm, 15 min, 30°C), and the supernatant was carefully removed. The pellet was finally redispersed in Milli-Q water.

### 5.4.11. Release Experiments

*Release experiments of S1-O1*.

To investigate the gating properties of S1-O1, 450 µg of this solid was suspended in 1.7 mL of hybridization buffer and separated in two aliquots of 850 µL each. The first fraction was diluted with 150 µL of Milli-Q water, whereas the second one was treated with 150 µL of an aqueous solution containing 8.9 µM of oligonucleotide O2. In both cases, the suspensions were stirred for 60 min at 37 °C. In order to remove the solid, both fractions were centrifuged. Dye delivery at 60 min was then measured by the fluorescence emission of crystal violet in the solution at 620 nm ($\lambda_{exc}$ 590 nm).

*Release experiments of S2-O4*.

200 µL of S2-O4 solution (500 µg/mL) was suspended in 800 µL of a buffer solution. Then, this solution was divided in two aliquots and a proper amount of an aqueous cocaine stock solution (2 mM) was added to one of the aliquots to reach a final cocaine concentration of $10^{-4}$ M. At the same time, an equal amount of Milli-Q water (without cocaine) was added to the other aliquot. The suspension was kept at room temperature and after 1 hour it was centrifuged to remove the solid. This procedure was repeated for different cocaine concentrations. Serial dilutions of the cocaine-buffer stock solution were performed for lower cocaine concentration detection.

## 5.5. References

[1] R. P. Goodman, I. a T. Schaap, C. F. Tardin, C. M. Erben, R. M. Berry, C. F. Schmidt, a J. Turberfield, Science 310 (2005) 1661.

[2] M. Nishikawa, S. Rattanakiat, Y. Takakura, Adv. Drug Deliv. Rev. 62 (2010) 626.

[3] A. Mahapatro, Mater. Sci. Eng. C 55 (2015) 227.

[4] A. B. Descalzo, R. Martínez-Máñez, F. Sancenón, K. Hoffmann, K. Rurack, Angew. Chemie - Int. Ed. 45 (2006) 5924.

[5] K. Ariga, Y. Yamauchi, Q. Ji, Y. Yonamine, J. P. Hill, APL Mater. 2 (2014) 030701.

[6] C. Coll, A. Bernardos, R. Martínez-Máñez, F. Sancenón, Acc. Chem. Res., 46 (2013) 339.

[7] Y. Klichko, N. M. Khashab, Y.-W. Yang, S. Angelos, J. F. Stoddart, J. I. Zink, Microporous Mesoporous Mater. 132 (2010) 435.

[8] A. Baeza, M. Colilla, M. Vallet-Regi, Expert Opin. Drug Deliv. 12 (2015) 319.

[9] C. Argyo, V. Weiss, C. Bräuchle, T. Bein, Chem. Mater. 26 (2014) 435.

[10] A. Agostini, L. Mondragón, A. Bernardos, R. Martínez-Máñez, M. D. Marcos, F. Sancenón, J. Soto, A. Costero, C. Manguan-García, R. Perona, et al., Angew. Chem. Int. Ed. Engl. 51 (2012) 10556.

[11] R. Qian, L. Ding, H. Ju, J. Am. Chem. Soc. 135 (2013) 13282.

[12] É. Pérez-Esteve, A. Fuentes, C. Coll, C. Acosta, A. Bernardos, P. Amorós, M. D. Marcos, F. Sancenón, R. Martínez-Máñez, J. M. Barat, Microporous Mesoporous Mater. 202 (2015) 124.

[13] F. Sancenón, L. Pascual, M. Oroval, E. Aznar, R. Martínez-Máñez, ChemistryOpen 2015, n/a–n/a.

[14] K. Ren, J. Wu, Y. Zhang, F. Yan, H. Ju, Anal. Chem. 86 (2014) 7494.

[15] E. Climent, D. Gröninger, M. Hecht, M. A. Walter, R. Martínez-Máñez, M. G. Weller, F. Sancenón, P. Amorós, K. Rurack, Chemistry, 19 (2013) 4117.

[16] S. Wu, X. Huang, X. Du, Angew. Chem. Int. Ed. Engl. 52 (2013) 5580.

[17] S. Sarkar, S. Dutta, T. Pal, J. Phys. Chem. C 118 (2014) 28152.

[18] K. Kneipp, Y. Wang, H. Kneipp, L. T. Perelman, I. Itzkan, R. R. Dasari, M. S. Feld, 78 (1997) 1667.

[19] W. Ma, H. Yin, L. Xu, X. Wu, H. Kuang, L. Wang, C. Xu, Chem. Commun., 50 (2014) 9737.

[20] H. U. I. Wang, D. W. Brandl, Acc. Chem. Res. 40 (2007) 53.

[21] B. Sharma, R. R. Frontiera, A.-I. Henry, E. Ringe, R. P. Van Duyne, Mater. Today 15 (2012) 16.

[22] T. Kang, S. M. Yoo, I. Yoon, S. Y. Lee, B. Kim, Nano Lett. 10 (2010) 1189.

[23] L. Polavarapu, A. La Porta, S. M. Novikov, M. Coronado-Puchau, L. M. Liz-Marzán, Small 10 (2014) 3065.

[24] D. Cialla, S. Pollok, C. Steinbrücker, K. Weber, J. Popp, Nanophotonics, (2014) 383.

[25] X. X. Han, Y. Ozaki, B. Zhao, TrAC Trends Anal. Chem. 38 (2012) 67

[26] S. Siddhanta, C. Naray, Nanomater. Nanotechnol. 2 (2012) 1.

[27] A. F. Palonpon, J. Ando, H. Yamakoshi, K. Dodo, M. Sodeoka, S. Kawata, K. Fujita, Nat. Protoc. 8 (2013) 677.
[28] J. Langer, S. Novikov, L.M. Liz-Marzán, Nanotechnol. (2015) in press
[29] J.J. Giner-Casares, M. Henriksen-Lacey, M. Coronado-Puchau, L.M. Liz-Marzán, Mater. Today.10.1016/j.mattod.2015.07.004.
[30] G. Lu, H. De Keersmaecker, L. Su, B. Kenens, S. Rocha, E. Fron, C. Chen, P. Van Dorpe, H. Mizuno, J. Hofkens, et al., Adv. Mater. 26 (2014) 5124.
[31] S. Zong, Z. Wang, H. Chen, J. Yang, Y. Cui, Anal. Chem. 85 (2013) 2223.
[32] M. Hecht, E. Climent, M. Biyikal, F. Sancenón, R. Martínez-Máñez, K. Rurack, Coord. Chem. Rev. 257 (2013) 2589.
[33] J.-M. Li, W.-F. Ma, C. Wei, L.-J. You, J. Guo, J. Hu, C.-C. Wang, Langmuir, 27 (2011) 14539.
[34] D.-K. Lim, K.-S. Jeon, H. M. Kim, J.-M. Nam, Y. D. Suh, Nat. Mater. 9 (2010) 60.
[35] M. Comes, G. Rodríguez-López, M. D. Marcos, R. Martínez-Máñez, F. Sancenón, J. Soto, L. A. Villaescusa, P. Amorós, D. Beltrán, Angew. Chem. Int. Ed. Engl. 44 (2005) 2918.
[36] P. C. Choppa, A. Vojdani, C. Tagle, R. Andrin, L. Magtoto, Mol. Cell. Probes 12 (1998) 301.
[37] F. J. van Kuppeveld, J. T. van der Logt, A. F. Angulo, M. J. van Zoest, W. G. Quint, H. G. Niesters, J. M. Galama, W. J. Melchers, Appl. Environ. Microbiol. 58 (1992) 2606.
[38] P. F. Liao, J. Chem. Phys. 76 (1982) 751.
[39] J. Gersten, A. Nitzan, J. Chem. Phys. 73 (1980) 3023.
[40] E. P. Barrett, L. G. Joyner, P. P. Halenda, J. Am. Chem. Soc. 73 (1951) 373.
[41] S. Brunauer, P. H. Emmett, E. Teller, J. Am. Chem. Soc., 60 (1938) 309.
[42] S. Razin, D. Yogev, Y. Naot, Microbiol. Mol. Biol. Rev. 62 (1998) 1094.
[43] M. V. Cañamares, C. Chenal, R. L. Birke, J. R. Lombardi, J. Phys. Chem. C 112 (2008) 20295.
[44] E. Climent, L. Mondragón, R. Martínez-Máñez, F. Sancenón, M. D. Marcos, J. R. Murguía, P. Amorós, K. Rurack, E. Pérez-Payá, Angew. Chem. Int. Ed. Engl. 52 (2013) 8938.
[45] L. Pascual, I. Baroja, E. Aznar, F. Sancenón, M. D. Marcos, J. R. Murguía, P. Amorós, K. Rurack, R. Martínez-Máñez, Chem. Commun. 51 (2015) 1414.
[46] M. N. Stojanovic, D. W. Landry, J. Am. Chem. Soc. 124 (2002) 9678.
[47] C.-Y. Zhang, L. W. Johnson, Anal. Chem. 81 (2009) 3051.
[48] J. Chen, J. Jiang, X. Gao, G. Liu, G. Shen, R. Yu, Chem. - A Eur. J. 14 (2008) 8374.
[49] M. N. Stojanovic, P. de Prada, D. W. Landry, J. Am. Chem. Soc. 123, (2001) 4928.
[50] J. Liu, J. H. Lee, Y. Lu, Anal. Chem. 79 (2007) 4120.
[51] F. Xia, X. Zuo, R. Yang, Y. Xiao, D. Kang, A. Vallée-Bélisle, X. Gong, J. D. Yuen, B. B. Y. Hsu, A. J. Heeger, et al., Proc. Natl. Acad. Sci. U. S. A. 107 (2010) 10837.
[52] J. Liu, Y. Lu, Angew. Chemie 118 (2006) 96.

[53] B. R. Baker, R. Y. Lai, M. S. Wood, E. H. Doctor, A. J. Heeger, K. W. Plaxco, J. Am. Chem. Soc. 128 (2006) 3138.
[54] J. Das, K. B. Cederquist, A. A. Zaragoza, P. E. Lee, E. H. Sargent, S. O. Kelley, Nat. Chem. 4 (2012) 642.
[55] J. Chen, J. Jiang, X. Gao, G. Liu, G. Shen, R. Yu, Chemistry, 14 (2008) 8374.
[56] J. Kimling, M. Maier, B. Okenve, V. Kotaidis, H. Ballot, A. Plech, J. Phys. Chem. B 110 (2006) 15700.
[57] L. Scarabelli, M. Coronado-puchau, J. J. Giner-casares, J. Langer, L. M. Liz-marzan, ACS Nano 8 (2014) 5833.

# 6. General Conclusions

Altogether this thesis represents a significant advancement in the development of novel plasmonic biosensors. Gold nanoparticles with improved plasmonic properties were successfully obtained and implemented for the biodetection of relevant molecules for biology and human health.

Although specific conclusions have been included at the end of each chapter, the most relevant overall conclusions can be divided attending to the gold nanoparticle shape used for the development of the sensors:

1) Plasmonic biosensors using AuNRs:

  a) the enzymatic activity of acetylcholinesterase (AChE) can modulate the growth of AuNRs.

  b) subnanomolar concentrations of paraoxon, a typical nerve gas analog, can be colorimetrically detected by modulating the growth of AuNRs

  c) the enzyme Horse Radish Peroxidase can gradually oxidize AuNRs in the presence of $H_2O_2$.

  d) a simple human blood glucose colorimetric assay in physiological conditions has been developed by combining AuNRs, HRP and a second enzyme, Glucose Oxidase.

2) Plasmonic biosensors using AuNTs:

a) monodisperse solutions of stable AuNTs can be self-assembled at the air-liquid interface for the preparation of plasmonic SERS substrates.

b) Benzenethiol SERS detection can be significantly improved by using AuNTs as enhancing substrates.

c) The combination of AuNTs and mesoporous silica nanoparticles loaded with Crystal Violet can be used for ultrasensitive detection of biorelevant analytes, which has been demonstrated with *Mycoplasma* spp. and cocaine. Limits of detection as low as 20 copies $\mu L^{-1}$ and 10 nM can be achieved for *Mycoplasma* genomic DNA and cocaine, respectively.

# 7. Resumen

En esta tesis se pretende desarrollar nuevos biosensores mediante el uso de nanopartículas metálicas, principalmente de oro y de plata. El trabajo que aquí se presenta se centra en la síntesis de esas nanopartículas, la funcionalización de su superficie y su posterior aplicación en la detección de biomoléculas relevantes para la salud humana. El desarrollo de nuevas y mejores nanopartículas metálicas (NPs) junto con el control de la química de su superficie es indispensable para este propósito. En este sentido, la síntesis y funcionalización se llevó a cabo siguiendo los protocolos existentes y mejorando otros. Todas las NPs se estudiaron mediante técnicas espectroscópicas y microscopía electrónica de transmisión, y se utilizaron para la detección de muy bajas concentraciones de gases nerviosos, glucosa, ADN bacteriano o cocaína, entre otros. El objetivo principal de esta tesis es, pues, la preparación de nanoestructuras adecuadas para la detección selectiva y a bajo costo de analitos biológicos.

Tras introducir el estado del arte en el capítulo 1, en los capítulos 2 y 3 se desarrollaron biosensores colorimétricos para la detección de glucosa y gases nerviosos mediante la combinación de nanorods de oro y enzimas. En una primera serie de experimentos se investigó el efecto de una molécula obtenida enzimáticamente en el proceso de síntesis de los AuNRs (Capítulo 2). La enzima acetilcolinesterasa fue seleccionada para producir tiocolina, molécula tiolada capaz de adsorberse a la superficie de semillas de oro y modular así la síntesis de AuNRs. La posterior inhibición de la actividad de la acetilcolinesterasa con análogos de gases nerviosos ha permitido la detección colorimétrica de los mismos de forma selectiva y ultrasensible.

En un segundo grupo de experimentos se oxidaron AuNRs con la ayuda de radicales hidroxilo producidos enzimáticamente (capítulo 3). La enzima peroxidasa del rábano (en inglés Horse Radish Peroxidase, HRP) en presencia de $H_2O_2$ se utilizó para la oxidación controlada de los AuNRs. El acoplamiento enzimático entre la glucosa oxidasa y HRP dio lugar al desarrollo de un nuevo ensayo colorimétrico fácil de implementar para la detección de glucosa.

En ambos casos, el uso de AuNRs y la introducción de especies biocatalíticas mejoró significativamente la eficacia y la biocompatibilidad del sistema, abriendo así nuevas posibilidades en el diseño de biosensores.

En el capítulo 4 se sintetizaron nanotriángulos de oro (AuNTs) homogéneos y monodispersos de diferentes tamaños que presentan características plasmónicas muy interesantes con un gran potencial para el diseño de biosensores. La combinación de AuNTs y nanopartículas de sílice mesoporosa cargadas con colorantes nos permitió diseñar un ensayo novedoso para la detección de ADN de *Mycobacterium sp*. y cocaína por medio de espectroscopía de dispersión Raman amplificada en superficie (SERS) (Capítulo 5).

En conjunto, se espera que esta tesis represente un avance significativo en el uso de nanopartículas metálicas para el diseño de nuevos biosensores. Las nanoestructuras diseñadas en esta tesis, junto con el uso de catalizadores biológicos facilitan la detección de diferentes biomoléculas sin el uso de complicados y costosos instrumentos.

## 7.1. Introducción

En las últimas décadas, las nanopartículas metálicas se han convertido en un elemento indispensable para el desarrollo de nuevos sensores capaces de detectar moléculas y biomoléculas de manera rápida, sensible y a bajo coste. Las extraordinarias propiedades ópticas de las nanopartículas y la química de su superficie han dado lugar a la aparición de nuevos ensayos *in vitro* e *in vivo* para la detección de biomoléculas, células e incluso tejidos afectados por una patología.

Una de las estructuras más importantes para el desarrollo de estos sistemas han sido las nanovarillas de or (Au nanorods o AuNRs). De entre las distintas estrategias posibles para sintetizar esta nanoestructura, el crecimiento a partir de semillas propuesto por Murphy *et al.* se ha convertido en el protocolo más eficiente para su síntesis en términos de control de tamaño, forma y monodispersidad. Los nanorods de oro se sintetizan en un medio que contiene principalmente CTAB y una sal de oro, así como una pequeña cantidad de iones plata que juegan un papel importante en la ruptura de la simetría de la semilla y posterior formación de las nanopartículas. Las propiedades ópticas de estas nanopartículas se relacionan con su resonancia plasmónica superficial (dos bandas plasmónicas en el Vis/NIR), cuya frecuencia es extremadamente sensible a pequeños cambios en el tamaño y forma del nanorod, conviertiéndolos en candidatos ideales para el desarrollo de biosensores. Además, la intensidad del campo eléctrico en las distintas zonas de estas y otras nanopartículas anisotrópicas como los nanotriángulos de oro, ha aumentado en los últimos años el interés por estas nanopartículas, que pueden actuar de sustratos para la espectroscopía por dispersión Raman aumentada por superficie (SERS), técnica utilizada para la ultradetección de moléculas.

Otras nanopartículas que en la actualidad también presentan una gran relevancia en el diseño de biosensores son las partículas mesoporosas de sílice. Estas NPs presentan poros que pueden ser cargados con distintas biomoléculas que permanecen en su interior por medio de ciertas moléculas que actúan de “puerta” y que se pueden abrir en presencia de un estímulo externo (cambio en el pH, temperatura, presencia de moléculas complementarias…), permitiendo así la liberación del contenido de los poros.

El desarrollo de nuevos biosensores requiere, por tanto, nuevos protocolos para la síntesis de nanopartículas más homogéneas que permitan alcanzar límites de detección hasta ahora no logrados con las distintas técnicas existentes.

## 7.2. Modulación Enzimática del Crecimiento de Nanorods de Oro y su Aplicación para la Detección de Gases Nerviosos.

El proceso de crecimiento de nanocristales metálicos a partir de semillas puede verse afectado por una gran variedad de moléculas capaces de adherirse a la superficie de las semillas. En este trabajo se moduló el crecimiento de los nanorods mediante la adición de una molécula tiolada producida por la enzima acetilcolina esterasa (AChE). Esta enzima es capaz de hidrolizar la acetiltiocolina (ATCh) para producir tiocolina (TCh) e iones acetato de forma controlada. La adición de tiocolina durante el proceso de formación de los nanorods de oro nos permitió modular la síntesis de nanorods, dando lugar a la formación de otras geometrías como cubos y esferas. Como se observa en la Figura 6.1B cuando las concentraciones de tiocolina son bajas, el número de nanorods disminuye y el de cubos aumenta. Sin embargo, a medida que aumenta esta concentración tanto los cubos como los nanorods desaparecen y los cristales crecen dando lugar a esferas.

Estos resultados se han obtenido tanto por medios espectroscópicos y por microscopía electrónica de transmisión (Figure 6.1).

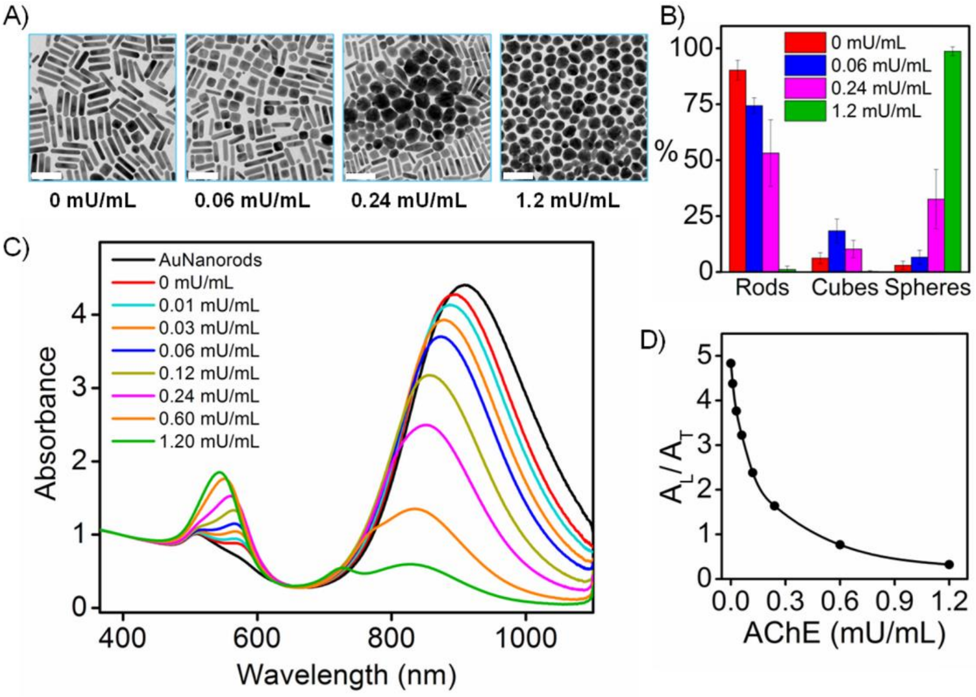

**Figura 6.1.-** Efecto de la tiocolina sobre el crecimiento de AuNRs. A) Imágenes de TEM de los productos obtenidos tras la adición de 0.05 mM ATCh y varias concentraciones de AChE. B) Porcentaje de las diferentes geometrías obtenidas para cada concentración de AChE. C) Espectros de absorbancia de los productos formados en presencia de 0.05 mM ATCh y varias concentraciones de AChE. D) Variación de la relación obtenida entre el máximo de la banda de resonancia longitudinal y el máximo de la banda transversal. Escala: 100 nm.

La AChE es un enzima fundamental en las sinapsis colinérgicas, ampliamente distribuidas por el sistema nervioso central y el periférico, de manera que cualquier inhibidor de la enzima se considera muy tóxico y/o mortal para el ser humano. Estos inhibidores se han usado como armas químicas ya que son relativamente baratos y altamente letales. Por ello, el uso de la AChE no sólo permitió el ajuste fino de las concentraciones de tiocolina durante el crecimiento de los nanorods, sino que además nos sirvió para el desarrollo de un sensor colorimétrico para gases nerviosos. Como ejemplo de ellos utilizamos el paraoxon, un organofosfato, análogo de los gases nerviosos, capaz de inhibir la enzima AChE.

El sistema resultó tan eficiente que pudieron detectarse cantidades extremadamente pequeñas de paraoxon (límite de detección de 280pM) lo que representó una gran avance en el desarrollo de biosensores plasmónicos (Figura 6.2).

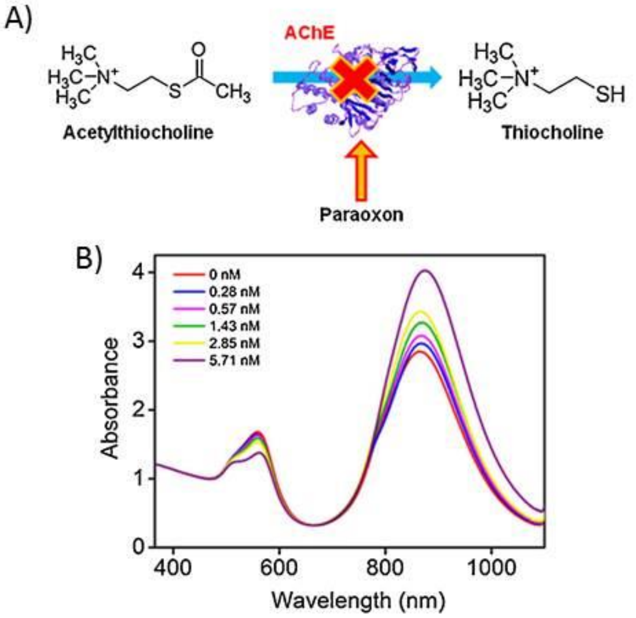

**Figura 6.2.-** A) Esquema en el que se muestra la inhibición de la actividad de la enzima AChE por efecto del paraoxon. B) Espectros de absorción de los productos formados en presencia 0.025 mM ATCh, 0.185 mU/mL AChE y diferentes concentraciones de paraoxon.

## 7.3. Oxidación Enzimática de Nanorods de Oro por Peroxidasa del Rábano y su Aplicación en la Detección de Glucosa en Sangre

Como ya se especificó en un apartado anterior, los nanorods de oro (AuNRs) presentan propiedades ópticas excepcionales debido a la elevada sensibilidad de su resonancia plasmónica superficial a pequeños cambios en el tamaño y la forma de los nanorods. En este contexto, el uso de $H_2O_2$ permite la oxidación selectiva de los nanorods disminuyendo, por tanto, su relación de aspecto. Sin embargo, esta oxidación requiere del uso de altas cantidades de $H_2O_2$ en condiciones especiales de temperaturas y pH, impidiendo su uso como biosensores. Para superar esta limitación, en este trabajo hemos introducido la enzima HRP que permite la oxidación gradual de los nanorods a muy bajas concentraciones de $H_2O_2$ en condiciones fisiológicas.

Cómo se observa en la Figura 6.3A-C, la actividad enzimática de HRP en presencia de $H_2O_2$ acorta selectivamente la longitud de los AuNRs, lo que se traduce en una respuesta óptica (Figura 6.3DyE) que puede, incluso, percibirse a simple vista.

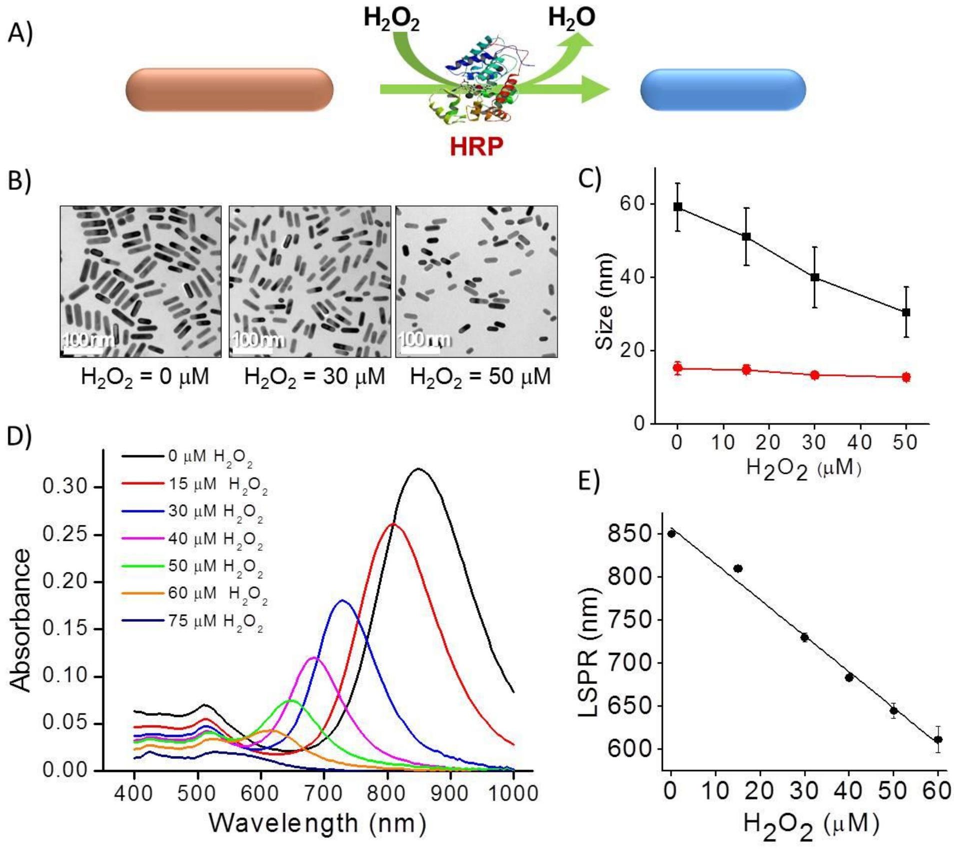

**Figura 6.3.-** A) esquema representando la oxidación enzimática de los AuNRs por acción de la actividad enzimática de HRP. B) imágenes de TEM de los AuNRs tras la adición de diferentes concentraciones de $H_2O_2$ en presencia de HRP (1.5 mM). C) Tamaño de los AuNRs en función de la concentración de $H_2O_2$. C) Longitud (cuadrados negros) y anchura (círculos rojos) de los AuNRs en función de la concentración de $H_2O_2$. D) Espetros de absorbancia de los AuNRs tras la incubación en presencia de HRP (1.5 mM) y diferentes concentraciones de $H_2O_2$. E) Variación del máximo de la banda de resonancia longitudinal en función de la concentración de $H_2O_2$.

En este trabajo, además, se ha estudiado el efecto de distintos haluros ($Cl^-$, $Br^-$, $I^-$) en la oxidación de los nanorods. Se descubrió que la presencia de haluros facilitaba la oxidación de los NRs por HRP, permitiendo así ajustar los parámetros de la reacción y aplicar el sistema para la biodetección de glucosa en sangre. Para el desarrollo de un sensor de glucosa, la actividad de HRP se acopló a la actividad de una segunda enzima, la glucosa oxidasa (Figura 6.4A). La actividad enzimática de la GOx cataliza la oxidación de la glucosa de una muestra biológica, por ejemplo plasma, y genera $H_2O_2$ como producto. Este $H_2O_2$ será utilizado por la HRP para la oxidación de los nanorods. La aplicación práctica de este sistema requeriría que personal sin preparación especial pudiese usarlo como sensor de glucosa. Con este objetivo, se diseñó un gel de sílice en el que se encontraban embebidos todos los componentes necesarios para la reacción (nanorods+haluros+enzimas). De este modo, tal como se puede observar en la Figura 6.4B, al añadir una muestra biológica sobre la superficie del gel, se produce un cambio de color en el mismo que es directamente proporcional a la cantidad de glucosa contenida en la muestra.

**Figura 6.4.-** A) Representación esquematica de la oxidación de AuNRs tras el acoplamiento de la actividad enzimática de GOx y HRP. B) Detección colorimétrica de glucosa en sustratos de gel de sílice sobre pocillos de una placa.

## 7.4. Síntesis de Nanotriángulos de Oro y su Uso en Espectroscopía de Dispersión Raman Amplificada en Superficie (SERS).

En este capítulo se describe con detalle el proceso de síntesis y purificación de nanotriángulos de oro (AuNT). Inicialmente, se diseñó un protocolo que nos permitió sintetizar AuNTs homogéneos y monodipersos (desviación estándar del 3%) de 50 a 150 nm de lado. Estas nanopartículas fueron utilizadas para la detección de distintos analitos por SERS. Los nanotriángulos se sintetizaron mediante el crecimiento sobre semillas en un medio con iones de plata y yoduro, los cuales juegan un papel importante en la ruptura de la simetría de la semilla y la generación de partículas anisotrópicas. Tras la síntesis se desarrolló un método de purificación rápido que nos permitió obtener disoluciones puras de nanotriángulos de tamaño altamente uniforme (Figure 6.5).

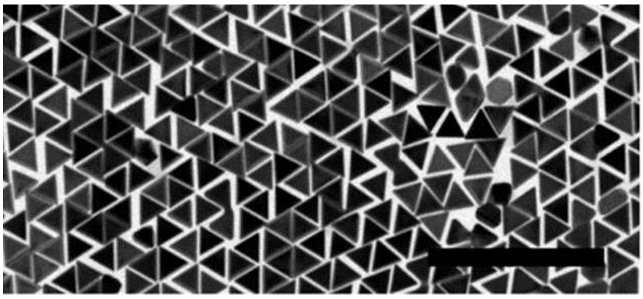

**Figura 6.5.-** Imagen de TEM de una disolución de nanotriángulos homogéneos. Escala 500nm.

Estas disoluciones fueron posteriormente ensambladas en la interfase aire/líquido donde formaron una monocapa, visible a simple vista, que podía ser transferida fácilmente sobre un sustrato. Finalmente, tanto los sustratos como las disoluciones de AuNTs fueron utilizados para medir por SERS diversos analitos: cristal violeta, tiofenol, 2,4 dinitrotolueno y 4-mercaptopiridina, con resultados muy prometedores ya que algunas de estas moléculas fueron detectadas a muy bajas concentraciones, como por ejemplo el tiofenol con un factor de mejora de $1{,}2*10^5$ con respecto a la intensidad de Raman.

## 7.5. Materiales Mesoporosos y Espectroscopía de Dispersión Raman Amplificada en Superficie (SERS) para la Detección de *Mycoplasma* sp. y Cocaína.

En este estudio se combinaron las virtudes de SERS, técnica espectroscópica rápida y sensible, con la biocompatibilidad y especificad de los materiales mesoporosos. Se sintetizaron partículas de sílice mesoporosa cargadas con el colorante violeta cristal (CV) y posteriormente se funcionalizaron con ADN de una especie de *Mycoplasma* (genero bacteriano de gran importancia médica y agrícola) y un aptámero para cocaína, respectivamente. En estos sistemas, los poros de las partículas mesoporosas quedan cerrados por interacciones electrostáticas y, por tanto, el CV queda en el interior de los mismos. La adición de un ADN complementario o de cocaína provoca la apertura y ulterior salida de CV de los poros (ver Figura 6.6).

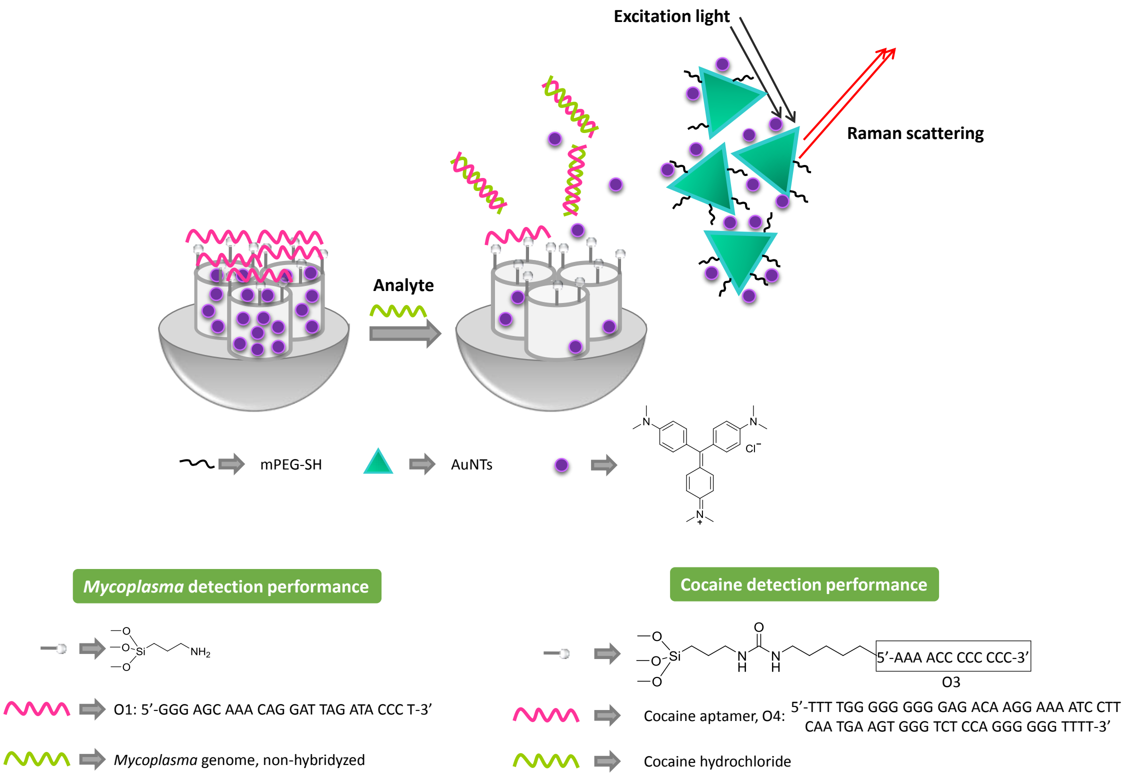

**Figura 6.6.-** Representación de una nanopartícula mesoporosa cargada con CV para la detección de ADN de *Mycoplasma* y cocaína.

A continuación, el CV liberado se adhirió a la superficie de los nanotriángulos de oro y la señal del CV se midió por medio de SERS. Este sistema resultó altamente eficaz para la detección de estas dos biomoléculas ya que llegaron a detectarse 20 copias μL$^{-1}$ de ADN genómico de *Mycoplasma fermentans* y concentraciones de cocaína del orden de 10μM.

## 7.6. Conclusiones Generales

En su conjunto esta tesis representa un avance significativo en el desarrollo de nuevos biosensores plasmónicos utilizando nanopartículas metálicas. Atendiendo a la morfología de las nanopartículas empleadas, las principales conclusiones del trabajo realizado se pueden resumir como sigue:

1) Biosensores plasmónicos en los que se emplearon AuNRs:

  a) la actividad de la enzima acetilcolinesterasa (AChE) puede modular el crecimiento de AuNRs.

  b) la modulación del crecimiento de AuNRs puede utilizarse para la detección colorimétrica de concentraciones subnanomolares de paraoxon, un análogo de gas nervioso.

  c) la enzima Peroxidasa del Rábano puede oxidar gradualmente AuNRs en presencia de $H_2O_2$, dando lugar a variaciones de color detectables por espectrometría o a simple vista.

  d) la combinación de AuNRs, HRP y una segunda enzima, glucosa oxidasa, puede utilizarse para el desarrollo de dispositivos capaces de detectar glucosa en sangre con gran precisión.

2) Biosensores plasmónicos en los que se emplearon AuNTs:

  a) Es posible inducir el autoensamblaje de AuNTs en una interfase aire-líquido, formando así sustratos plasmónicos muy eficientes.

  b) el uso de AuNTs mejora significativamente la detección por SERS de tiofenol y otras moléculas, en comparación con nanopartículas con otras morfologías.

c) la combinación de AuNTs y nanopartículas mesoporosas de sílice cargadas con Violeta Cristal puede utilizarse para detección ultrasensible de analitos biorelevantes, como *Mycoplasma* y cocaína, con límites de detección de 20 copies $\mu L^{-1}$ y 10 nM respectivamente.

# Agradecimientos

Quisiera agradecer esta tesis:

### *A mis directores*

Luis y Jorge. A Luis, por darme la oportunidad de cambiar de campo y aceptarme en su recién estrenado grupo. Desde que te conocí en Madrid en el año 2012 me animaste para que empezara esta aventura y me apoyaste en todos los aspectos para que esta tesis haya sido posible. Además de tu rapidez a la hora de contestar, corregir y gestionar en general cualquier aspecto relativo a la investigación, tengo que agradecerte toda la confianza y libertad con la que me has dejado trabajar durante este tiempo. Te agradezco el haber compartido conmigo toda tu experiencia y el haber estado ahí en todos los momento (buenos y malos) y espero poder seguir contando con tu amistad en el futuro. A Jorge, porque a pesar de estar separados por cientos de kilómetros siempre estuviste disponible para hablar sobre cualquier resultado y para ayudarme con la burocracia de la universidad que, como es bien sabido por todos, no es poca.

### *A mis colaboradores*

En primer lugar tengo que agradecer la ayuda recibida por toda la gente del grupo de Valery Pavlov, a los que están y a los que se fueron, y en especial a Laura Saa. Laura, tú sabes que sin tu determinante contribución y tu infinita paciencia este trabajo no habría sido posible. También tengo que agradecer a Mar Oroval del grupo de Ramón Martínez Mañez por su contribución en la síntesis de nanopartículas de sílice y su empeño en que las cosas funcionasen. A Uday y Rafal

Klajn por darme la oportunidad de visitar unos de los mejores centros de investigación a nivel internacional, the Weizmann Instute of Science, y por todo el trabajo realizado en el ensamblaje de nanopartículas.

### *A la gente de CICbiomaGUNE*

En primer lugar quiero agradecer la ayuda recibida de todos los compañeros que han pasado por el grupo y que he tenido el placer de conocer, son tantos que prefiero no nombrarlos por si olvido de alguno. Gracias a todos, me habéis enseñado y ayudado mucho. En especial quiero agradecer a mis compañeros de doctorado Ana, Andrea, Guillermo, María y Leonardo toda la ayuda y los buenos momentos que hemos pasado. También a Judith por las largas discusiones que parecían interminables e inútiles pero que acabaron dando sus frutos. Mención especial a Juanjo- muchas gracias por todas las cosas que me has enseñado y por soportarme cada día. Por último, también agradecer a los demás miembros de CICbiomaGUNE, con los que a diario me he cruzado, pues de algún modo también forman parte de esta tesis.

### *A mis amigos*

Estaré siempre agradecido a Yan Duan y Samuel Mañas por su amistad, por estar siempre ahí a pesar de todos mis defectos y por tantas y tantas cosas que hemos vivido. Ahh y por hacer posible que la empresa de los aguacates sea una realidad. Estoy convencido de que a pesar de las dificultades nuestra amistad no va acabar aquí y seguiremos compartiendo buenos momentos en el futuro.

### *A la financiación*

Esta tesis ha sido posible gracias al Ministerio de Educación, Cultura y Deporte por concederme la beca predoctoral FPU y también a los proyectos ERC Advanced Grant 267867 Plamaquo, BIO2011-26365, MAT2012-384229-C04-01, PROMETEOII/2014/047 y ISIC-Nano que financiaron esta investigación.

### *A mi familia*

Mis padres y mi hermana. Por todo el apoyo, comprensión, cariño y una lista interminable de cosas que me han dado durante este tiempo. Sin vosotros nunca hubiera llegado hasta aquí.